Image Segmentation Methods for Sea Ice Analysis

by

Giulio Passerotti

ORCID: 0009-0000-1090-1951

A thesis submitted in total fulfillment for the degree of Doctor of Philosophy

in the
Department of Infrastructure Engineering
Faculty of Engineering and Information Technology
THE UNIVERSITY OF MELBOURNE

October 2024

THE UNIVERSITY OF MELBOURNE

Abstract

Department of Infrastructure Engineering
Faculty of Engineering and Information Technology

Doctor of Philosophy

by Giulio Passerotti
ORCID: 0009-0000-1090-1951

The size and shape of ice pieces floating in the sea, known as floes, play a critical role in understanding the dynamics of ice-covered oceans. These characteristics significantly affect albedo, sea ice concentrations, energy exchanges between the ocean and the atmosphere, and the spreading of waves through ice-infested waters. Despite the availability of diverse image recognition techniques suitable for analyzing ice-covered water imagery, accurately detecting and measuring floes presents a considerable challenge.

This study explores floe size estimation by tackling the difficulties of detection using conventional image processing methods in a controlled laboratory setting. This preliminary step lays the groundwork for further field observations, where a precise methodology for image acquisition is established, including camera calibration to correct perspective distortion. Image segmentation techniques are then applied to in-situ sea ice imagery, comparing traditional methods with modern ones: a snake-based algorithm and the Segment Anything Model (SAM), an advanced deep learning model from Meta. To overcome the limitations of each approach, a combined technique leveraging the advantages of both is proposed. The efficacy of this integrated method is validated through an in-depth analysis of floe size statistics, highlighting significant differences in outcomes across the methods. Finally, this hybrid methodology is applied to an extensive dataset of images from multiple Antarctic winter expeditions, providing a practical framework for the analysis of sea ice properties.

Declaration of Authorship

I, Giulio Passerotti, declare that this thesis titled, 'Image Segmentation Methods for Sea Ice Analysis' and the work presented in it are my own. I confirm that:

- The thesis comprises only my original work except where indicated in the preface;
- due acknowledgement has been made in the text to all other material used; and
- the thesis is fewer than the maximum word limit in length, exclusive of tables, maps, bibliographies and appendices as approved by the Research Higher Degrees Committee.

Signed: Giulio Passerotti

Date: 9 October 2024

Preface

This thesis presents the research carried out during my Ph.D. candidature at The University of Melbourne. It comprises 8 main chapters. The first chapter provides an introduction to the thesis as a whole. Chapter 2 offers a theoretical background, while Chapter 4 discusses field image acquisition. The final chapter presents the conclusions of the work.

- Chapter 3 presents the paper:

  Giulio Passerotti, Luke G. Bennetts, Franz von Bock und Polach, Alberto Alberello, Otto Puolakka, Azam Dolatshah, Jaak Monbaliu, and Alessandro Toffoli. Interactions between irregular wave fields and sea ice: A physical model for wave attenuation and ice breakup in an ice tank. *Journal of Physical Oceanography*, 52 (7):1431–1446, July 2022. ISSN 1520-0485. doi: 10.1175/jpo-d-21-0238.1

- Chapters 5-7 present the development of an image segmentation method based on the acquisition of winter Antarctic expeditions in 2017, 2019, and 2022. It is noteworthy that the content within these chapters constitutes unpublished material and has not been submitted for publication at this juncture.

Acknowledgements

Field campaigns were funded by the South African National Antarctic Program through the National Research Foundation. This work has also received funding from the ACE Foundation, Ferring Pharmaceuticals, the Australian Antarctic Science Program (project 4434), and the Australian Research Council (DP200102828). The project was made possible thanks to collaboration with the international Southern Ocean Seasonal Experiment (SCALE) and the University of Cape Town.

I wish to express my thanks to the Faculty of Engineering and Information Technology (FEIT) for awarding me the Ph.D. scholarship that provided me with the immense opportunity to embark on a rewarding research career.

I sincerely extend my deepest gratitude to my dedicated supervisor, Prof. Alessandro Toffoli, for all his invaluable advice, patience, and unwavering encouragement throughout my Ph.D. journey. His immense knowledge and experience have served as sources of inspiration and motivation, setting an example for me to aspire to.

I also wish to express my sincerest thanks to my co-supervisors, Prof. Ian Yang and Prof. James Bailey, and committee chair A/Prof. Xuemei Liu, for all the stimulating discussions, comments, and suggestions that have improved the quality of this research.

Many thanks to my colleagues and friends, Dr. Alberto Alberello and Ippolita Tersigni, with whom I had the privilege of participating in the expedition campaigns over the Antarctic sea ice. Together, we shared some of the most formative and enriching on-field experiences of my entire Ph.D. journey.

Finally, I wish to express my gratitude to my family and my partner, Alessia Miccinesi, for their unwavering support, understanding, and assistance throughout this challenging academic endeavour. Their love and encouragement have provided me with the emotional strength and stability needed to pursue this Ph.D. project with dedication and perseverance.

I lovingly dedicate this work to Priscilla, whose presence and inspiration have been a guiding light in my journey.

Contents

List of Figures

List of Tables

Chapter 1

Introduction

1.1 Image Processing for Antarctic Science

Sea ice is a vital component of Earth's cryosphere, which encompasses all of its frozen water, and plays a critical role in regulating the global climate system. Understanding the dynamics of sea ice is crucial for predicting and comprehending Earth's responses to climate change and its broader climatic impacts. The Southern Ocean is particularly pivotal for Earth's climate. Across its vast expanses of uninterrupted water, interactions between strong winds, large waves, intense currents, and the seasonal sea ice cycle fuel the exchange of heat and gas between the air and sea. This confers on the Southern Ocean the capacity to store more energy than any other latitude band on the planet and absorb notable masses of the extra heat and carbon dioxide from human activities.

Air-sea interaction processes in the sea ice region of the Southern Ocean [3, 4], and in particular in the marginal ice zone – the band of movable sea ice cover between the open ocean and more compact sea ice conditions – are still elusive but essential for refining retrieval algorithms for satellite remote sensing, enhancing climate models, and improving predictions [5]. The remoteness and extreme weather conditions of the region complicate in-situ observational efforts, contributing to a significant knowledge and technological gap. By closely observing changes over time in the sea ice region, scientists can gain insights into the processes that regulate sea ice formation and melting, as well as the overall stability of the ice cover [6, 7].

Collecting sea ice data is challenging due to the limitations of existing observational methods and the inhospitable, remote nature of polar regions. The harsh conditions of Antarctica, along with logistical challenges and high costs associated with extensive field campaigns, have historically restricted the quantity and quality of observational data available. Additionally, the inherently dynamic nature of sea ice, which continuously responds to atmospheric and oceanic conditions, complicates efforts to achieve consistent and continuous measurements [8].

Most of the data available in the sea ice region, especially in Antarctica, rely on visual observations acquired through the ASPeCT protocol during voyages to high latitudes [9, 10]. However accurate, visual observations are subject to human errors and interpretation, which introduce inconsistent sets of uncertainties into a general database. For example, if the same portion of sea ice is assessed by three observers, it is likely they would return three different observations. I personally encountered this challenge while contributing to sea ice visual observations aboard the S.A. Agulhas II in 2022, particularly when attempting to assess the size and concentration of ice floes from a distance without any available reference points.

Advancements in image processing techniques have begun to address these data gaps in a more objective manner. Cameras and sensors enable continuous monitoring of large sea ice areas with high precision, providing spatially and temporally continuous data. This technology delivers detailed insights into ice concentration, floe size distribution, and other critical parameters.

This automated approach significantly reduces the uncertainties and errors associated with manual methods and provides more reliable and comprehensive data for researchers and operations in polar regions. It is worth noting, however, that uncertainties cannot be entirely eliminated; a digitized observation protocol based on computer vision would standardize observation errors. Compared to traditional methods, such as manual counting from ships – a labor-intensive process that offers limited spatial and temporal resolution – image processing techniques provide a more thorough and continuous dataset. This is crucial for evaluating and enhancing the accuracy of sea ice models, especially in terms of floe size distribution. Such methods not only broaden the scope of geographical and temporal observations but also improve the precision with which changes in the Antarctic sea ice landscape are assessed.

1.2 Research objectives

This research aims to address the data scarcity in polar regions by leveraging images from Antarctic expeditions to develop an algorithm capable of effectively identifying ice floes under the challenging conditions typical of Antarctica. The identification of ice floes in digital images facilitates the estimation of key parameters, such as floe size distribution and sea ice concentration, which are essential for understanding the high spatial and temporal variability of oceanic, atmospheric, and ecological conditions in the marginal ice zone.

The thesis employs high-resolution, close-range digital images and advanced image processing techniques to achieve the following objectives:

- Evaluate ice identification challenges, including the detection of floe edges and the estimation of floe shapes, in a controlled laboratory setting where an ice sheet is fragmented by artificially generated waves.
- Develop a robust image acquisition technique to operate aboard an icebreaker vessel that mitigates wave-induced perspective distortions and incorporates a method for converting image data into metric measurements.
- Generalize and automate the application of object segmentation to images with varying levels of clarity and assess both traditional segmentation techniques and modern methods that use artificial intelligence.
- Develop a hybrid algorithm that combines the strengths of traditional and AI-based approaches.
- Conduct a statistical comparison to determine the most effective segmentation method for accuracy and efficiency in identifying ice floes and estimating floe size and ice concentration.

1.3 Thesis structure

The structure of the thesis follows a logical progression, starting with an analysis of sea ice images in a laboratory setting to understand the challenges of image segmentation. This initial work helped identify key obstacles and refine the methodology, which was then extended to real-world scenarios. The research progressed through evaluating segmentation methods for detecting sea ice from in-situ imagery. Chapter 3 of the thesis includes a manuscript that has been published in the Journal of Physical Oceanography (JPO), and the format of the publication has been maintained.

Chapter 2 provides a brief review of computer vision methods to measure sea ice. The chapter starts with a brief overview of sea ice in the marginal ice zone. It then reviews methods for detecting sea ice characteristics from images acquired from ships, aerial vehicles, and satellites. These methods range from classical edge detection filtering to advanced artificial intelligence systems. Additionally, methods for extracting ice properties from images taken in a laboratory are analyzed. These experiments serve to recreate the dynamic processes occurring in the marginal ice zone in a controlled scale and setting. They are used for both advancing knowledge of complex coupled processes in the sea ice regions and acquiring images for training AI-based algorithms for sea ice data retrieval.

Chapter 3 details an experiment that investigates the challenges of image segmentation in detecting sea ice floes within a controlled laboratory setting, where conditions can be precisely managed, unlike in natural environments. The study focuses on how different steepness levels of incident wave fields influence the breakup and transition of sea ice from a continuous to a fragmented state. This physical modeling approach aids in understanding the dynamics of sea ice in response to wave energy, and the mechanisms underlying ice breakup. It also discusses analogies between wave and sea ice floe statistics.

Chapter 4 outlines the process of capturing sea ice images during three winter expeditions in the Antarctic Marginal Ice Zone (MIZ). It establishes a precise methodology for image acquisition, including the correction of geometric distortions in images based on the camera's internal parameters. This technique, known as objective orthorectification, converts pixels to meters without relying on known reference objects within the camera's field of view. The chapter also examines how the ship motion due to wave action affects this orthorectification process. A set of images representing a broad spectrum of field conditions encountered in the Southern Ocean is selected and manually segmented to create a high-quality reference for evaluating subsequent image segmentation methods.

Chapter 5 introduces the adaptation of an active contours model, specifically the Gradient Vector Flow (GVF) snake algorithm, for detecting sea ice floes in digital images. This algorithm segments floes that appear connected, using a dynamic curve that adjusts to fit the precise boundaries of the floes. An automated initial contour generator, designed to adapt to various ice floe shapes, is proposed. The chapter also discusses pre-processing techniques that enhance image sharpness and smoothness to address challenges with uneven grayscale distribution, which can affect segmentation accuracy. The results from this snake-based method are compared with those from manual segmentation.

Chapter 6 explores new techniques in image segmentation derived from deep learning models, particularly assessing the suitability of vision foundation models for ice analysis. These models, which do not require training, are ideal for polar regions where fresh, relevant training data is scarce. The Segment Anything Model (SAM), a type of foundation model adept at segmenting every object within an image, is applied to the same subset of benchmark images. Adjustments are made to enable this model to process images acquired under conditions that reflect the complexity of the Antarctic environment. The results are visually compared with those obtained through manual segmentation.

Chapter 7 proposed a new segmentation algorithm that combines the GVF algorithm and SAM. This hybrid approach utilizes the strengths of both segmentation methods and is applied to the same subset of images used by other techniques for direct comparison with the manual benchmark. A more robust subset of images is then used to estimate floe size statistics across the various segmentation methods proposed in this dissertation. Variations in floe size statistics arising from the GVF, SAM, and combined SAM-GVF methods are discussed. The best-performing method is applied to the entire database from winter expeditions to the Antarctic MIZ in 2017, 2019, and 2022, with parameters such as floe area, diameter, and ice concentration determined for each image and their statistical properties discussed.

Chapter 8 presents the overall conclusions of the thesis.

Chapter 2

Computer Vision for Sea Ice Measurements

2.1 Introduction

Sea ice imagery is essential for observing and analyzing sea ice for scientific purposes as well as key to underpinning navigation at high latitudes. Various remote sensing technologies and digital imaging techniques are used to monitor fundamental aspects of sea ice, such as concentration, floe size distribution, thickness, and types. The dynamic nature of sea ice means that its size, shape, and distribution can vary significantly (e.g. [11]), influenced by environmental factors such as wind, temperature, and water currents [12]. Ice floes may also be densely packed or overlapping (see Figure 2.1), complicating the task of distinguishing their boundaries in images, especially from a distance or when they are partially covered by snow. This complexity is exacerbated by the harsh and variable lighting conditions typical of polar regions, including low light levels, sun glare, and reflections off the ice surface that can obscure visibility [13].

Computer vision is employed to address these challenges by automating the detection and measurement processes, which are typically labour-intensive and subjective when performed manually [14–16]. Through advanced image processing techniques and machine learning algorithms, computer vision systems can consistently analyze visual data from cameras and sensors, even in difficult conditions. These systems are designed to adapt to the various appearances and formations of ice [17], providing accurate, repeatable, and scalable measurements. They significantly enhance the capability to monitor sea ice by processing large volumes of data quickly, reducing human error, and enabling real-time measurements [18, 19].

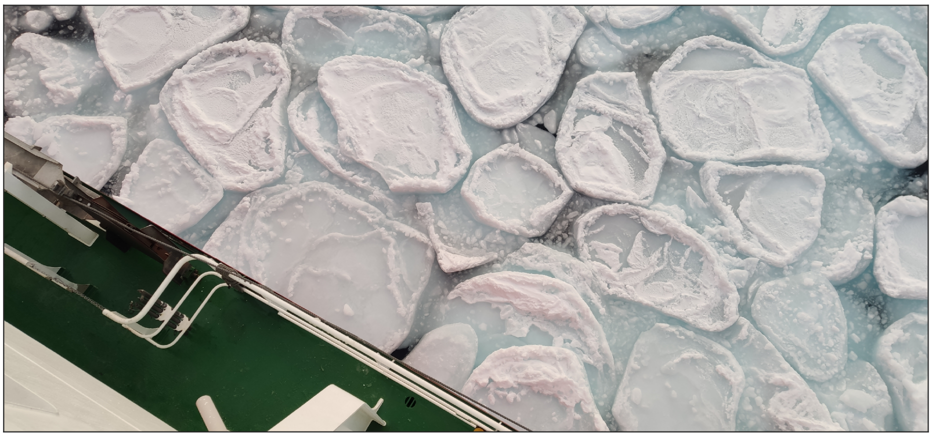

FIGURE 2.1: Image captured aboard a ship showing densely packed and overlapping ice floes.

In this chapter, a description of the marginal ice zone – the area between the continuous ice cover and the ocean where ice is formed and transformed, and the focus of this dissertation – is first presented. Methods to extract properties of ice floes in this zone are discussed. Images from satellites, shipborne cameras, and aerial vehicles are utilized to develop an automatic recognition system for sea ice. These images are often combined to create a more comprehensive detection algorithm using deep learning models. Additionally, experiments and images taken in laboratory settings are used to study the behavior of ice under external forces in a controlled environment. These images contribute to understanding the challenges of detecting sea ice and serve as a basis for building more generalized models.

2.2 The marginal ice zone

Sea ice plays a crucial role in Earth's climate system, performing multiple crucial functions that influence both global and regional climates. It reflects sunlight back into space, significantly increasing the planet's albedo, which is vital for regulating global temperatures [20]. Sea ice insulates the warmer ocean waters from the colder atmospheric temperatures, moderating oceanic heat exchange with the atmosphere and influencing atmospheric circulation patterns. When sea ice forms it releases salt, increasing water density and driving ocean currents, which, in turn, are essential for global heat distribution. The growth and melt of sea ice impact the Earth's carbon cycle by influencing biological productivity in polar regions [21]. Furthermore, sea ice provides essential habitats and hunting grounds for a variety of marine species, from microorganisms to large mammals, supporting diverse ecosystems. The presence, distribution, and changes in sea ice cover are critical indicators of climate change and are vital for climate modeling and environmental forecasting.

The Marginal Ice Zone (MIZ) is a critical and dynamic area within the sea ice environment where sea ice and open water interact, comprised of ice floes ranging from centimeters to tens of kilometers in size. Ice floes are floating pieces of sea ice that vary from small fragments (a few meters) to vast sheets (a few hundred meters) [22]. This zone is particularly sensitive to climate and ocean conditions as it sets the edge between the continuous ice cover and the ocean. Characterized by sea ice concentrations between 15% and 80%, the MIZ's semi-enclosed nature creates a dynamic environment where ice floes of various sizes and shapes are continuously formed and altered [23]. It is more susceptible to wave action and temperature fluctuations than the stable consolidated ice (see e.g. [11, 24]). The processes occurring in the MIZ, including the breakup of ice due to wave interactions and the melting patterns influenced by oceanic heat, are vital for understanding how changes in sea ice cover may impact global climate patterns.

The size distribution of ice floes is crucial in understanding sea ice dynamics inside the MIZ. Their distribution affects the melting processes around the edges of the ice floes, which is where most melting occurs due to the direct contact with warmer ocean waters [25]. Secondly, the size and shape of these floes influence the ocean surface energy budget [26, 27] by modifying the albedo effect – the reflection of solar energy back into space. Larger floes have a different albedo and heat absorption capacity compared to smaller ones. Moreover, the distribution impacts sea ice rheology [28] – the deformation and movement of sea ice under external forces – which in turn affects the overall ice dynamics, including the formation of ice ridges and leads (openings in sea ice).

The MIZ's dynamic environment is further complicated by its exposure to oceanic waves and swells, which can break up ice floes, creating smaller fragments [29]. This fragmentation process is influenced by the floe size, which dictates how waves transmit energy through the ice (cf. [30]). Smaller floes might lead to increased wave energy dissipation, while larger floes could scatter wave energy [31, 32]. Therefore, understanding how different sizes of floes distribute in the MIZ is crucial for predicting changes in sea ice dynamics and their broader climatic impacts.

Traditional sea ice models have struggled with adequately incorporating processes related to the floe size distribution due to limited observational data, which is necessary for validating these models [33]. Observations of sea ice have traditionally been sparse, especially high-resolution data that can accurately capture the details of floe size and shape across different resolutions and under various conditions.

2.3 In-situ sea ice imagery

Camera systems have become widely employed due to their affordability, reliability, and the ability to offer temporally and spatially continuous field observations of sea ice conditions (e.g. [34, 35]). Numerous studies [14, 16, 34, 36–41] have been undertaken to detect ice floes from digital images obtained aboard ships or from aerial perspectives. Unlike aerial cameras, ship-mounted cameras provide continuous recording, enabling a more comprehensive and dynamic understanding of sea ice behavior.

The principal challenge in processing sea ice images resides in associating each individual pixel with its corresponding floe. A classical approach focuses on the threshold segmentation algorithm. Sea ice images are transformed into 2D grayscale images and the histogram of the pixel intensities is calculated. A threshold value is then selected based on this histogram to separate the intensity range of the ice floes from the background water. However, this threshold is normally a subjective user-dependent value [34, 42, 43]. Efforts to automate the process of ice identification have resulted in the development of more sophisticated techniques, such as the k-means algorithm [37, 39], gradient vector flow (GVF) snake algorithm [16] and watershed segmentation [36, 44]. Nevertheless, none of these studies execute a proper calibration of the camera [45] to obtain a top-view projection of the images and, consequently, an accurate pixel-to-meter conversion. As a result, no size-related statistics of the floes can be extracted. Furthermore, these methods often require user intervention to extract the boundaries of the floes.

To the best of the authors' knowledge, the sole complete and automated method proposed for detecting ice floes from close-range optical images is by Sandru et al. [14]. After perspective correction, this method employs a revised version of the k-means algorithm to categorize pixel intensities into four groups: two for different types of ice, one for open water, and the last for everything else. The k-means algorithm partitions a set of data into k distinct groups so that the data in each group are as similar to each other as possible [46]. The principal problem with this technique when applied to sea ice is that the number of clusters must be formulated in advance and cannot be changed. Therefore, this method is only effective if the selected ice groups are all present in the image. In reality, close-range ice imagery is irregular, as the illumination within them is neither homogeneous nor constant among images taken at different times of the day, due to weather conditions (see Figure 2.2) and other external factors. If the grayscale values of pixels within a single floe vary considerably, these could be associated with two distinct clusters. Consequently, forcing the detection of four groups in any case [14] could lead to misleading results.

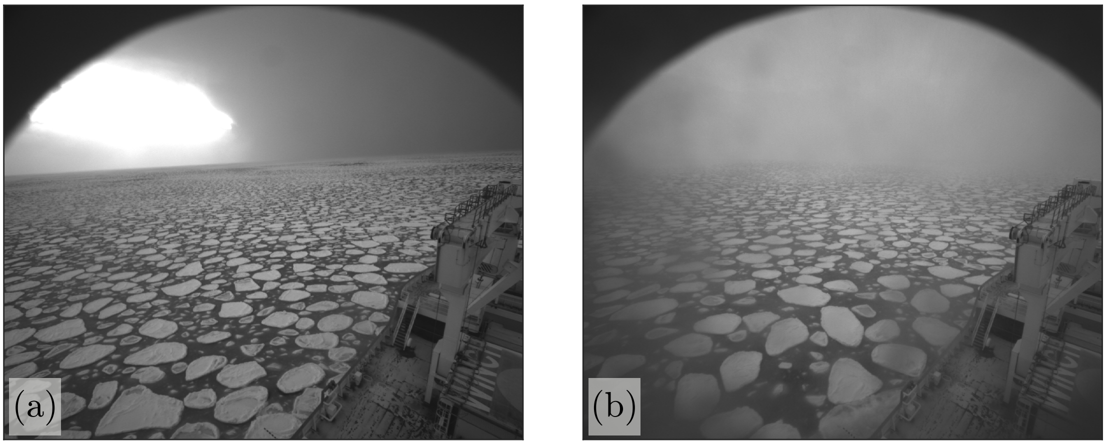

Figure 2.2: Sample images captured under varying weather conditions: (a) partially sunny skies and (b) low visibility due to snowfall.

In recent years, deep learning (DL) has significantly transformed image processing by achieving unprecedented levels of accuracy and performance in object detection, image classification, and semantic image segmentation. Convolutional neural networks (CNN) can automatically learn features from images and extract high-level semantic information. By learning from a vast array of training data, CNNs can identify and categorize pixels in new images based on the patterns they have learned.

In the context of sea ice recognition, CNNs have been applied in several studies [40, 41, 47] to analyze digital images acquired from sensors installed on ships to differentiate between various elements surrounding the vessel such as ice, water, and sky. These models demonstrate strong generalization abilities across various unseen datasets, making them robust for real-time application in different ice conditions. These studies perform semantic segmentation which involves classifying each pixel in an image into predefined categories, effectively partitioning the image into segments that share semantic properties. Thus, they do not differentiate between individual ice entities. Additionally, in most studies, the semantic segmentation does not address perspective distortion or perform camera calibration, which is necessary for accurately measuring the dimensions of identified ice features [40]. This omission limits the practical application of these models in tasks that require precise size estimations of ice formations [15].

Deep learning models demand significant computational resources for building the training dataset. This burden can restrict their implementation on systems with limited processing power, making them less suitable for potential real-time applications. Moreover, the effectiveness of these models is greatly influenced by the quality and diversity of the training data they are exposed to. Insufficient representation of diverse ice conditions can limit its effectiveness. Without this diversity in training data, the model's practical utility and accuracy in real-world scenarios may be severely compromised (this is a common problem in other research fields that rely on computer vision; see e.g. [48]).

2.4 Satellite

Remote sensing techniques, especially satellite sensors, have become increasingly popular for studying sea ice [49]. Satellite images provide a reliable and extensive source of data, particularly in remote polar regions where conducting direct observations is challenging. One of the primary benefits of using satellite imagery for monitoring sea ice is their ability to consistently and regularly cover vast areas that are otherwise hardly accessible. Although satellite images may have a limited temporal resolution, they provide continuous observation all-the-year-round. This is in contrast to images taken from ships and aircraft, which, while high in resolution, are only available during the short duration of polar expeditions. It should be noted that satellite imagery is constrained by clouds, which is a critical problem, especially in the Southern Ocean [50]. However, the technical advancements in Synthetic Aperture Radar (SAR) have significantly enhanced the quality and reliability of sea ice detection. SAR is particularly valuable due to its ability to penetrate through clouds and operate independently of daylight, delivering data with a resolution ranging from meters to tens of meters across large areas [51]. This capability makes satellite images suitable for studying medium-sized floes (10-100 m) [15, 29]. However, they are less effective for examining pancake ice floes, which typically measure between 4 and 6 m and constitute a critical sea ice form in the marginal ice zone during winter. [34].

Despite these limitations, the ease of accessing satellite data has led the scientific community to develop new techniques for identifying ice and other glaciological features from these images. These methods range from manual interpretations by experts to more sophisticated automated systems that utilize deep learning and advanced algorithms [52]. One of the key techniques for identifying ice floes and their boundaries is dynamic thresholding [53, 54]. This method adapts to the specific characteristics of the image to differentiate between ice and open water. It adjusts the threshold values according to the local statistics of the image, which allows for more accurate differentiation. The detailed surface characteristics of ice are also crucial for distinguishing between different types of ice and segmenting the ice floes. Texture features, extracted from SAR images, play a significant role in this process, offering a statistical representation that reflects the distribution of pixel values and their spatial relationships within the image. By capturing the spatial variation of pixel intensities, these texture features significantly enhance the accuracy of ice classification [55].

Segmentation techniques, which are essential for analyzing close-range images captured in situ, can also be adapted for use with satellite imagery. This adaptability demonstrates that segmentation algorithms are largely independent of image resolution, making them versatile across different imaging contexts. Common techniques such as k-means clustering [29] and watershed algorithms [56] provide examples of how these methods can be adjusted to work effectively with the distinct characteristics of satellite images.

The development of deep learning models has further reduced the gap between the segmentation techniques used for satellite imagery and those used for in situ images. This advancement has been particularly influential in enabling the use of close-range images to train neural networks that are then applied to more broadly captured satellite images. For instance, Zhang and Hughes [15] has utilized a dataset of images captured from aircraft to train a CNN. To overcome the challenge of costly and time-consuming data annotation required for training these models, Zhang and Hughes [15] implemented a GVF snake algorithm to automatically label ice floes in the local-scale marginal ice zone images. The trained CNN is subsequently applied to segment larger-scale satellite images, which are typically more numerous and available. This approach allows the trained neural networks to apply the knowledge and patterns learned from in situ images to effectively segment and analyze satellite imagery, despite the inherent differences in detail and resolution.

Deep learning models, however, require substantial amounts of labeled data to learn from. Specifically, these models need extensive datasets with each floe distinctly labeled to accurately identify and segment individual ice floes. Obtaining detailed images of sea ice, particularly from remote polar regions, is inherently difficult. Moreover, the process of accurately labeling these images is not only crucial for the success of the models but also highly labor-intensive. This substantial requirement for detailed, labeled data creates a major barrier to entry, which could restrict the broader adoption of advanced artificial intelligence (AI) techniques in remote sensing applications.

To ease the requirements of data annotation and model training, vision foundation models have been developed [57]. These are large, pre-trained deep learning models that have been initially trained on vast, diverse datasets. Essentially, foundation models transfer the knowledge they have acquired from their comprehensive initial training to new and less familiar tasks. This adaptability reduces the necessity for creating and labeling extensive new datasets for each specific application. Consequently, researchers can use these models for tasks like segmenting sea ice in satellite imagery with considerably less initial data.

An example of this is the first vision foundation model, known as the Segment Anything Model (SAM), which was studied by Shankar et al. [58] for its ability to perform semantic segmentation of large icebergs in satellite images. Remarkably, without any additional training data, SAM achieved accuracy levels comparable to those of highly specialized CNNs. This development significantly reduces the need to build deep learning models from scratch, thereby making it more practical to apply sophisticated AI techniques in the challenging conditions of polar ice research.

2.5 Experiments

Laboratory experiments in ice facilities are crucial for studying complex environmental interactions because they allow for precise control over conditions that are difficult to manage in natural settings. In the context of ice research, conducting experiments in a lab setting enables scientists to manipulate and standardize variables like environment illumination, ice texture, gradient, and shape (see details in Chapter 3). This controlled environment results in digital images of consistently high clarity.

Typically, these images are captured using a camera positioned to look directly downward at the ice. This setup ensures a clear, unobstructed view of the ice surface below without perspective distortion. Additionally, the size of the ice tank – where the (model) ice is contained and examined – provides a scale reference that is crucial for geometric adjustments in the imaging process. These adjustments are necessary to ensure that the digital images accurately represent the true sizes of the ice floes. By enabling such precise control and measurement, laboratory experiments facilitate detailed and accurate studies of ice behaviors and properties under various simulated environmental conditions.

Several experiments have been conducted in controlled settings to explore parameters that are difficult to isolate in natural environments due to the unpredictable and extreme conditions of polar regions. For instance, Herman et al. [59] focused on the behavior of sea ice under wave-induced stress. This experiment involved artificially generating wave patterns to break a continuous, uniform sheet of ice and then analyzing the sizes of the ice floes produced. Other studies, such as those by Zhang et al. [60] and Byun and Nam [61], involved cutting level ice into square pieces and distributing them within the ice tank. These experiments aimed to assess how ice impacts the integrity and operational capabilities of structures in cold regions, thereby aiding the planning and safety of marine operations.

In laboratory settings, where variables can be meticulously controlled, traditional image processing techniques such as image binarization and morphological operations prove particularly effective for detecting sea ice [60, 61]. The process of binarization converts the original image into a binary image, often referred to as a mask. In this binary image, pixels representing ice are assigned a value of one, while those representing the background water are assigned a value of zero. This straightforward approach generally allows for the clear separation of individual ice floes within the camera's field of view. However, in crowded scenes where floes are densely packed, these basic techniques might not suffice to accurately delineate the boundaries of each floe without manual adjustments. To address this issue, more advanced image processing methods have been developed and applied, as noted in Zhang et al. [60]. These advanced techniques enhance the precision of the segmentation process, reducing the need for manual corrections.

Images captured in laboratory settings are not only instrumental in examining how ice responds to external forces but also serve as valuable resources for building high-quality datasets of segmented ice floes. These datasets can be exploited to train deep learning models intended for field use. Although these images represent a more idealized version of ice conditions, as opposed to the broad diversity found in natural environments, they help mitigate the common issue of data scarcity in polar regions by providing a rich source of consistent and controlled data.

For example, Zhou et al. [62] discussed the development and application of a neural network designed to identify sea ice floes and calculate their concentration from images captured by ship-based cameras. The model was trained on laboratory images showcasing various floe shapes and sizes, under a range of lighting conditions and viewing angles. The controlled and consistently replicated laboratory conditions were essential for developing a robust deep learning model. This setting enabled the algorithm to learn from clear, well-documented examples, reducing the inconsistencies often found in segmented field data. This example highlights the applicability of well-segmented laboratory images in developing and refining AI models for practical use in the demanding conditions of polar regions.

2.6 Conclusions

The size and distribution of ice floes within the MIZ crucially impact the melting processes and the ocean surface energy budget, influencing sea ice dynamics and broader climatic impacts. Understanding these dynamics is vital for climate modeling and forecasting, emphasizing the need for high-resolution observations to improve sea ice models.

A variety of image processing techniques have been utilized to detect sea ice and measure floe properties using data from satellites, shipborne cameras, and aerial vehicles. These approaches range from traditional image processing methods to advanced deep learning techniques. Deep learning models, in particular, have proven to be highly effective, providing quick and accurate classifications of ice in images. However, most of these techniques focus on semantic segmentation, which classifies different areas of images but is not able to identify individual instances of ice floes. Distinguishing between overlapping floes in crowded scenes remains a significant challenge, requiring training datasets that capture the inherent variability and dynamic nature of sea ice within the MIZ.

The need for techniques capable of processing images under less than ideal conditions – such as unclear boundaries between floes and inconsistent lighting and weather – is recognized as fundamental for accurately handling field ice imagery. In subsequent chapters, it will be explored how image processing techniques can be applied in a controlled laboratory environment to study the characteristics of ice floes. This exploration is essential for the development of generalized segmentation algorithms capable of detecting individual ice floes amidst the constantly changing conditions of the MIZ.

Furthermore, the process of correcting perspective distortions and establishing an objective conversion between pixels and meters for accurately measuring floe sizes will be discussed. This issue, often overlooked in the literature, is critical for accurately studying parameters like floe size distribution. By addressing these challenges, an enhancement in our understanding and modeling of sea ice dynamics can be achieved, contributing significantly to our knowledge of climate systems.

Chapter 3

Interactions between Irregular Wave Fields and Sea Ice: A Physical Model for Wave Attenuation and Ice Breakup in an Ice Tank[1]

Abstract

Irregular, unidirectional surface water waves incident on model ice in an ice tank are used as a physical model of ocean surface wave interactions with sea ice. Results are given for an experiment consisting of three tests, starting with a continuous ice cover and in which the incident wave steepness increases between tests. The incident waves range from causing no breakup of the ice cover to breakup of the full length of ice cover. Temporal evolution of the ice edge, breaking front and mean floe sizes are reported. Floe size distributions in the different tests are analysed. The evolution of the wave spectrum with distance into the ice-covered water is analysed in terms of changes of energy content, mean wave period and spectral bandwidth relative to their incident counterparts, and pronounced differences are found between the tests. Further, an empirical attenuation coefficient is derived from the measurements and shown to have

[1]This chapter has been published as: Giulio Passerotti, Luke G. Bennetts, Franz von Bock und Polach, Alberto Alberello, Otto Puolakka, Azam Dolatshah, Jaak Monbaliu, and Alessandro Toffoli. Interactions between irregular wave fields and sea ice: A physical model for wave attenuation and ice breakup in an ice tank. *Journal of Physical Oceanography*, 52(7):1431–1446, July 2022. ISSN 1520-0485. doi: 10.1175/jpo-d-21-0238.1

a power-law dependence on frequency comparable to that found in field measurements. Links between wave properties and ice breakup are discussed.

3.1 Introduction

Over the past decade, interactions between surface gravity waves and sea ice have become more broadly recognised as important for wave and sea ice processes [63–65]. Major international research programs have focused on wave–ice interactions and the marginal ice zone where wave–ice interactions occur [66–69]. A central theme of the research advances is integration of wave–ice interactions into numerical wave models [70–73] and sea ice models [74–77] used for operational forecasts, climate studies and other scientific investigations. Following the framework set by [78] and Williams et al. [79, 80], wave–ice interaction models tend to couple the two key processes of (i) wave attenuation over distance travelled due to ice cover, and (ii) wave-induced breakup of continuous ice covers (very large ice floes) into collections of smaller floes, notwithstanding other potentially important wave–ice interaction processes, such as wave-induced ice drift [81, 82], wave-driven floe–floe collisions [83, 84] and wave overwash of floes [85, 86]. Rapid progress has been made in understanding and modelling wave–ice interactions, but conspicuous knowledge gaps still exist, particularly for wave-induced ice breakup.

Wave attenuation in the ice-covered ocean is measured using wave-buoy arrays [67, 87], synthetic aperture radar [88, 89] and stereo-imaging techniques [24, 90]. Analysis of the data collected suggests each frequency component of the wave spectrum attenuates exponentially with distance travelled, and that the rate of attenuation increases with increasing frequency, so that the spectrum skews towards low frequencies [87, 91]. The observations of frequency-dependent exponential wave attenuation are consistent with prevailing theories, which are broadly divided into two categories: (a) scattering theory, in which attenuation results from an accumulation of partial wave reflections by each individual floe; and (b) viscous theories, in which the ice cover is typically treated as a continuum and wave energy is dissipated by some (often unspecified) mechanism in the ice or underlying water. Scattering theory is applicable when wavelengths are comparable to floe sizes, and predictions show pleasing agreement with historical data from the Arctic basin where the scattering regime is generally valid [92–94]. Viscous continuum models are applicable when wavelengths are much greater than floe sizes, which is the relevant regime for most recent observations, and the viscous parameters are typically chosen to give agreement with the observations [95, 96]. Wave measurements are usually not accompanied by detailed measurements of the ice conditions, and the relationship between wave attenuation rates and ice conditions is largely unknown. However, there are consistent reports of wave blocking by continuous ice cover transitioning to relatively weak attenuation following ice breakup [97, 98].

Reports of wave-induced ice breakup exist in the literature, based on visual observations from ships [97, 99–101] or inferred from satellite imagery [29, 98]. Local measurements of wave and ice properties during breakup events are rare, which makes it challenging to assess the relative wave and ice conditions that lead to breakup, the resulting floe size distribution and breakup effects on waves [2]. Additional complications are presented by unknowns associated to wave attenuation [102]. Wave-induced ice breakup theories are typically based on stresses and/or strains imposed by a passing wave exceeding some critical value(s) [92, 103, 104], with variants that include ice fatigue [105], probabilistic treatment of wave amplitudes [79], irregular wave spectra [78, 106], three-dimensional effects [107], breakup memory [77] and viscoelastic ice [108].

Laboratory-scale physical modelling is generating understanding of wave–ice interactions to complement field observations and theory. Wave basin experiments are used to investigate wave attenuation (and related wave transmission/reflection) due to plastic or wooden floes [109–112], freshwater ice and model ice (saline or doped), with most up to 2020 listed by Parra et al. [113] and others since then [35, 114]. Few wave-basin experiments investigate wave-induced breakup. Herman et al. [59] study the floe size distribution resulting from wave-induced breakup of continuous model ice, but do not include measurements of waves in the ice-covered water. Therefore, they do not relate the extent of breakup to wave attenuation, and, moreover, they report breakup unexpectedly starting halfway along the length of the ice cover due to spurious waves reflected by the beach. Dolatshah et al. [30] conduct the only study [to our knowledge; noting it is overlooked by 113], in which both attenuation and breakup are measured simultaneously, although using freshwater ice (much stiffer than model ice) and in an essentially one-dimensional setting in a narrow wave basin. They report a transition from wave blocking by continuous ice to relatively weak attenuation by broken ice, similar to field observations [97, 98]. Cheng et al. [115] report breakup in their attenuation experiments using model ice, but exclude the corresponding wave measurements from their analysis. To date, almost all physical models of wave–ice interactions use regular incident waves, thus obscuring nonlinear processes for irregular sea-states, such as ice breakup, floe–floe collisions and overwash. The only exception is Klein et al. [114], who use transient wave packets, in part to avoid ice breakup.

In this article, we report a laboratory experiment in which (unidirectional) irregular wave fields are incident on model (doped) ice in a large ice tank (Aalto University, Finland). We study the transition from a continuous ice cover to a broken ice cover using a series of tests with increasingly energetic (steep) incident wave fields, which range from causing no breakup to breaking up the entire ice-cover length. A camera mounted above the basin monitors the ice cover during the tests, and image analysis is applied to extract the ice edge, breaking front and individual floe properties. Wave motion in the ice-covered water is inferred from an array of bottom-mounted pressure sensors and we analyse the evolution of the wave spectrum and attenuation of the spectral frequency. Correlations between wave properties and ice breakup, during its transition from compact to broken, are discussed.

3.2 Experimental model

3.2.1 Facility and model ice

The Aalto ice tank is 40 m long, 40 m wide and was filled with 0.3%-ethanol doped water up to 2.8 m depth (Figure 3.1a). It is bounded at one end by a computer-controlled wave-maker with 16 triangular plungers (2.5 m wide) and by a linear beach at the opposite end to absorb incoming wave energy (95% energy-effective for incident waves tested). The tank is equipped with a cooling system to control the ambient temperature.

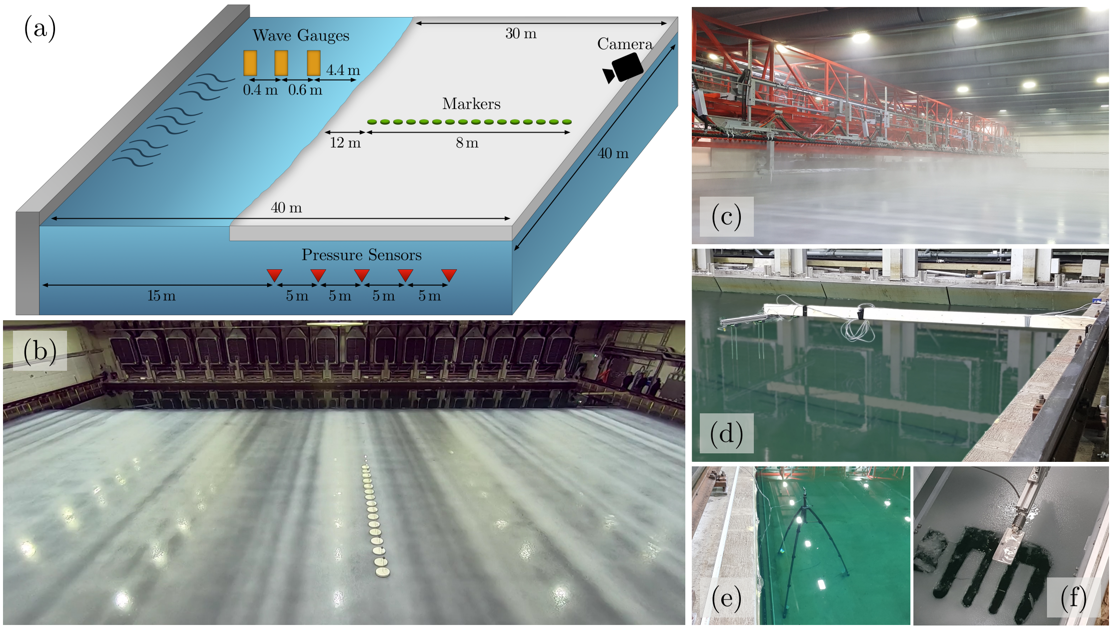

Figure 3.1: The physical model conducted at the Aalto ice tank: (a) schematic of the experimental setup (not to scale) indicating the wave maker (left-hand end), adjacent open water region of length 10 m, followed by region covered by model ice of length 30 m (initially continuous), and instrumentation (three wave gauges in open water, five pressure sensors below ice cover, sixteen markers on the ice surface, and a video camera); (b) image from video camera showing its field of view and the initial ice cover; (c) photo taken from tank side during spray of ice crystal; (d) photo taken from behind the wave maker showing wire wave gauges in open water; (e) photo showing a pressure sensor before creation of model ice cover; and (f) photo showing cantilever beam test.

Table 3.1: Pierson–Moskowitz incident wave spectra for three tests (Equation 3.1), plus initial and final ice conditions.

$H_{S,0}$ [m]	$T_{P,0}$ [s]	ε	$L_{P,0}$ [m]	Initial ice condition	Final ice condition
0.03	1.6	0.02	4	unbroken	unbroken
0.06	1.6	0.04	4	unbroken	partially broken
0.08	1.6	0.06	4	partially broken	fully broken

A model ice sheet with near uniform properties, and realistic thickness and flexural strength for a target scaling factor of ≈ 30, is produced over the entire water surface by first lowering the air temperature below freezing until a thin film of ice forms on the water surface. After this, layers of sub-cooled water are sprayed, forming ice crystals with diameter 1 mm (Figure 3.1c). The ambient temperature is then lowered to $-15°$C, which initiates crystal bonding and consolidation into an ice sheet of fine-grained structure [116, 117], until the desired strength is achieved. The ambient temperature is then increased slightly above freezing to adjust the flexural strength to its final value [e.g. 118]. The flexural strength can be tuned to a target value, but achieving a target stiffness is challenging [e.g 118–120]. The mechanical properties of the ice are measured with destructive cantilever beam tests in the ice sheet (Figure 3.1f) in accordance with the International Towing Tank Conference (ITTC) guidelines. The mechanical properties are preserved during the test by keeping the temperature close to the freezing point. The cantilever tests are carried out on a 10 m strip next to the beach, and the strip is removed upon completion. The remaining 30 m length of ice cover is cut free from the side walls, and carefully (to avoid cracking and modifications in the ice sheet) pushed towards the beach to form an initial region of open water for waves to be generated without ice interference (Figure 3.1b).

The freezing–warming cycle achieves the flexural strength $\sigma = 20.1$ kPa, which corresponds to the realistic field-scale flexural strength 550 kPa at scaling factor 27.3. The model ice thickness is $h = 30$ mm, which corresponds to a realistic field-scale thickness of 0.82 m. The Young's modulus of the model ice is $E = 5$ MPa, which corresponds to 0.14 GPa at field scale, i.e. one to two orders of magnitudes smaller than that of natural sea ice [cf. 121]. Model ice is typically too compliant [119], as it behaves nonlinearly in downward bending, exhibiting a significant plastic regime [118, 120]. Therefore, the model ice is expected to show weak elastic restoring forces when deflected by waves.

3.2.2 Initial conditions and instrumentation

Starting from the continuous ice cover, the experiment consists of monitoring the propagation of unidirectional, irregular incident waves through the ice cover and ice breakup and drift in response to wave forcing. Three incident wave conditions are tested, with the test for each condition lasting 20 minutes, which is the maximum time possible before reflection contaminates measurements in the middle of the tank in ice free conditions, and, therefore, considered conservative for the tests with ice. The input spectra are defined by the Pierson–Moskowitz fully developed sea state [122]

$$S_0(f) = \frac{\alpha_J g^2}{f^5} \exp\left[-\frac{5}{4}\left(\frac{f}{f_{P,0}}\right)^{-4}\right], \tag{3.1}$$

where $g \approx 9.81\,\mathrm{m\,s^{-2}}$ is the constant of gravitational acceleration, f the wave frequency, $f_{P,0}$ the frequency at the spectral peak and α_J is Phillip's constant. The peak frequency is $f_{P,0} = 0.625\,\mathrm{Hz}$ in all three tests, which corresponds to a peak period $T_{P,0} = 1.6\,\mathrm{s}$ and dominant wavelength $L_{P,0} = 4\,\mathrm{m}$ [based on the open water linear dispersion relation, 123]. Therefore, the field-scale wavelength is approximately 110 m. The Phillip's constant α_J was chosen to define different values of significant wave height ($H_{S,0} = 4\sqrt{m_{0,0}}$, where $m_{0,0}$ is the zeroth-order moment of the spectral density function), thereby defining different levels of wave steepness ($\varepsilon = k_{P,0}H_{S,0}/2$, where $k_{P,0} = 2\pi/L_{P,0}$ is the wavenumber at the spectral peak). The latter is a measure of the degree of nonlinearity of the wave field [e.g. 124, 125] and an indicator of the strength of wave–ice interactions [e.g. 109, 111]. The three tests use the steepness values $\varepsilon = 0.02$, 0.04 and 0.06 in order of increasing magnitude, so that the broken ice cover increases in length over the duration of the experiment (Table 3.1). Motion at the wave maker is determined by imposing complex Fourier amplitudes with moduli randomly chosen from a Rayleigh distribution around the target wave spectrum, and with phases randomly chosen from a uniform distribution over $[0, 2\pi)$ [this is a standard practice to produce random waves in the laboratory, see e.g. 124, 126]. Benchmark tests without the ice sheet are conducted to verify the incident wave field.

The water surface elevation along the tank is monitored with a combination of resistive wire wave gauges and pressure sensors, deployed 2.5 m from the side wall (Figure 3.1a), recording at a sampling rate of 300 Hz. Three wire gauges (Figure 3.1d) are installed in the open water at distances of 4.6 m, 5.0 m and 5.6 m from the wave maker (5.4 m, 5.0 m and 4.4 m from the ice edge) to monitor the incident wave field. The array configuration facilitates detection and removal of waves reflected by the ice cover [see method in 127]. Five pressure sensors (Figure 3.1e) were mounted on tripods 0.2 m below the water surface at 5 m intervals, with the first probe 15 m from the wave maker (5 m from the ice edge). A video camera is installed on the gantry above the beach, 5 m from the ice surface and inclined of 45° to monitor ice conditions (Figure 3.1a). The field of view (Figure 3.1b) captures the ice cover up to 22 m from the ice edge. Videos are recorded at a rate of 30 frames per second and at a resolution of 1920 × 1440 pixels. Sixteen markers are positioned on the ice cover every 0.54 m with the first one 12 m from the ice edge (Figure 3.1b), in order to provide reference distances and allow reconstruction of dimensions during image analysis.

3.3 Ice breakup

3.3.1 Image processing

During the tests, the continuous ice breaks up into floes and the ice edge (the boundary separating open and ice-covered water) moves. For one video frame per second, an algorithm is applied to extract the individual ice floe geometries, the ice breaking front (the farthest line of breakup) and the ice edge. Image processing begins with the raw image (Figure 3.2a), which is orthorectified to impose a constant scale, where features are represented in their true positions (Figure 3.2b). The physical dimensions of the individual picture elements (pixels) are extrapolated from known distances between markers and a Gaussian filter is used to reduce white noise and improve image clarity. A Sobel operator is used to capture high spatial gradients of image colour [128] and identify transverse edges, which correspond to ice breakup lines parallel to the wave front and ice edge. Distances from the wave maker to the edges are calculated based on the number of pixels. An average distance is computed for each breakup line to smooth irregularities. The upper edge separating the dark water surface from the brighter ice is associated to the ice edge (top red line in Figure 3.2b) and the bottom edge dividing the area of broken ice from the compact sheet is identified as the breaking front (bottom red line).

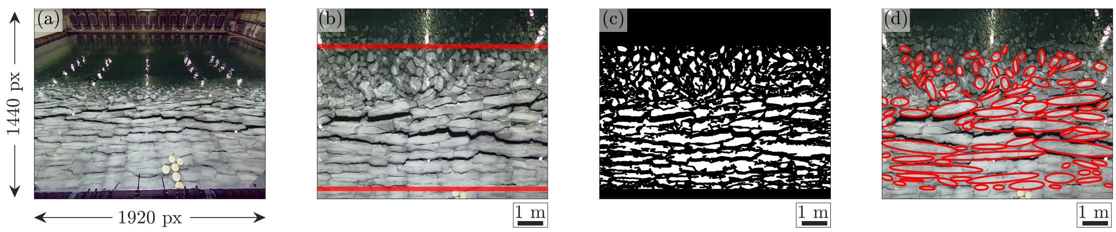

FIGURE 3.2: Stages of image processing for $\varepsilon = 0.06$ at $t \approx 300$ s: (a) raw frame; (b) orthorectified frame with ice edge (upper red line) and breaking front (bottom red line) indicated; (c) binary frame separating ice (white) from water (black); and (d) elliptical approximations for identified floes (excluding floes smaller than image resolution and large aggregate floes; red lines) superimposed on orthorectified frame.

To capture individual floe geometries, the images are converted into their binary counterparts (Figure 3.2c), thus separating the ice from water more sharply than using the Sobel operator. Transverse and longitudinal edges are identified using the Canny edge detector [128]. Motivated by the elongated forms of the floes (Figure 3.2c), floe shapes are approximate by ellipses (Figure 3.2d) with the same second moment of the covariance matrix [129]. Away from the ice edge, the ellipses are oriented so that the minor axes are roughly aligned with the incident wave direction and the major axes with the wave-front direction.

The properties of floes with areas smaller than $\approx 0.03\,\mathrm{m}^2$ (equivalent to a circle of diameter 0.2 m) are uncertain due to the resolution of the images. Therefore, these small floes are excluded from further analysis. Further, visual assessments of processed images against their raw counterparts reveals that floes with area greater than $\approx 20\,\mathrm{m}^2$ (equivalent to a circle of diameter 5 m) are aggregates of smaller floes, and, hence, are not analysed. Overall, $\approx 85\%$ of the floes within the field of view are captured and correctly identified (e.g. Figure 3.2d).

3.3.2 Ice edge and breaking front

Figure 3.3 shows the temporal evolution of the ice edge and breaking front over the three tests, denoted $i_w(t)$ and $i_b(t)$, respectively. The small steepness incident wave field in the first test ($\varepsilon = 0.02$; Figure 3.3a) is a lower bound for expected sea states in the Arctic Ocean [130] and rarely experienced in the Southern Ocean [3]. It propagates through the continuous ice cover without generating any visible fractures. The waves force overwash at the ice edge [131], which reaches up to 1.5 m onto the ice cover, and appears to accelerate ice edge melt and crumbling (although thermal properties were not measured), likely contributing to small variations in the location of the ice edge and breaking front (Figure 3.3a; also videos 1 and 2 in the supplementary material). This generates the initial difference between ice edge and breaking front in the subsequent test ($\varepsilon = 0.04$; Figure 3.3b).

The intermediate steepness incident field ($\varepsilon = 0.04$) is common in the Arctic Ocean [130] and a lower bound in the Southern Ocean [3]. The ice edge breaks up as soon as the incident field reaches it, with breakup both longitudinal (parallel to the wave crests) and transverse (along the direction of wave propagation). The breaking front advances ≈ 8 m (two wavelengths) deep into the ice cover for $t < 360$ s. The average speed of the breaking front is $\approx 0.02\,\mathrm{m\,s^{-1}}$, which is two orders of magnitude smaller than the incident group velocity ($C_{P,0} = 1.25\,\mathrm{m\,s^{-1}}$, i.e. the velocity of the incident wave front, calculated as $0.5L_{P,0}/T_{P,0}$ under the assumption of deep water). More generally,

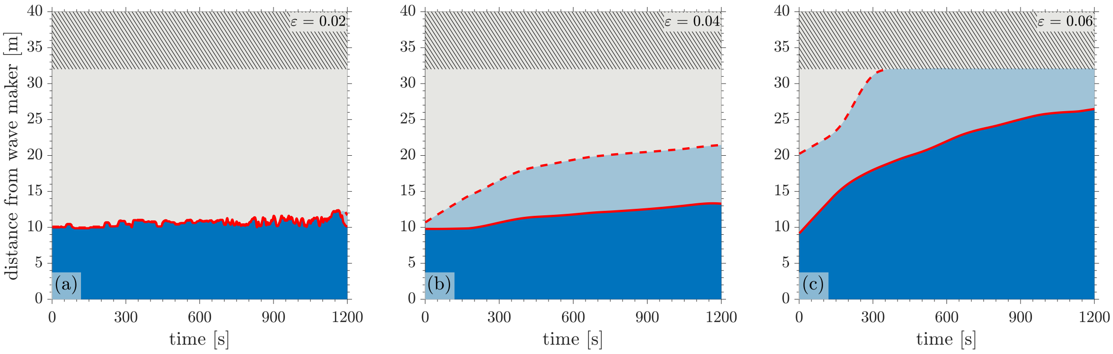

FIGURE 3.3: Spatio-temporal evolution of the ice cover during (a) $\varepsilon = 0.02$, (b) $\varepsilon = 0.04$ and (c) $\varepsilon = 0.06$ tests, indicating unbroken ice cover (white), open water (dark blue) and broken ice cover (light blue), which is bounded by the ice edge (i_w, solid red line) and the breaking front (i_b, dashed red line). The portion of the ice cover outside the camera field of view (last ≈ 8 m of the tank) is hatched.

it means that about 62 incident wave crests penetrate into the ice in order to break one linear metre of the ice cover. For $t > 360$ s, the breaking front slows down by an order of magnitude, advancing at a speed of only $\approx 0.003\,\mathrm{m\,s^{-1}}$.

During the second phase ($t > 360$ s), the ice edge retreats away from the wave maker due to gradual drift of the floes and ice-edge crumbling (see videos 3 and 4 in the supplementary material), and at approximately the same speed as the breaking front advances, so that the broken floe field length is almost constant, $i_b - i_w \approx 8$ m. Once the wave maker stops at the end of the test, the broken floes spread back upstream, slightly beyond the location of the initial ice edge, as indicated by $i_w \approx 9$ m at $t = 0$ for the final test ($\varepsilon = 0.06$; Figure 3.3c).

The steepest incident field ($\varepsilon = 0.06$) is an upper bound for the Arctic Ocean [130] and an average condition in the Southern Ocean [3]. Starting from a partially broken ice cover, the steep incident field breaks up the remaining continuous ice cover. Figure 3.3c only shows breakup to 32 m from the wave maker, but visual observations confirm full breakup, such that the breaking front reaches the beach, ≈ 20 m from its position at the beginning of this test, at $t \approx 600$ s. The average speed of the breaking front is $\approx 0.03\,\mathrm{m\,s^{-1}}$, which is a factor 1.5 greater than the speed of the breaking front in the intermediate steepness test for $t < 360$ s (considering that the incident group velocity is unchanged, the increase of breaking front velocity means that about 40 incident wave crests are sufficient to break a metre of ice cover). The steep incident field also causes strong drift of the broken floes, with the ice edge moving > 15 m downstream over the test (videos 5 and 6 in supplementary material). The rate of drift slows as the test progresses and floes accumulate towards the beach.

3.3.3 Floe size and size distribution

Figure 3.4 shows evolution of the average minor axis (D_1) and major axis (D_2) of the broken floes, normalised by the dominant incident wavelength ($L_{P,0} = 4\,\mathrm{m}$), for the intermediate steepness ($\varepsilon = 0.04$; Figure 3.4a) and large steepness ($\varepsilon = 0.06$; Figure 3.4b) tests. Averages are computed using floes in the strip of the tank between 15 and 30 m from the wave maker, thereby eliminating the ice cover beyond the field of view towards the beach and the small floes with uncertain properties close to the ice edge, for 30 s time windows with 25% overlaps to smooth trends. For the intermediate steepness, well defined floes are evident in the strip for $t > 400\,\mathrm{s}$ only (videos 3 and 4 in supplementary material), and floe sizes are calculated from this point till the end of the test. The minor and major axes are almost constant from $t = 400\,\mathrm{s}$ until the end of the test, with the minor axis $\approx$ 9% of the incident wavelength ($D_1 \approx 0.36\,\mathrm{m}$) and the major axis 35% ($D_2 \approx 1.4\,\mathrm{m}$). The large steepness incident field breaks up all of the ice in the strip, including breaking up already broken floes, causing the average minor and major axes to steadily decrease. At the end of the test, the minor axis is reduced to around 7% of the incident wavelength ($D_1 \approx 0.28\,\mathrm{m}$) and the major axis 15% ($D_2 \approx 0.6\,\mathrm{m}$).

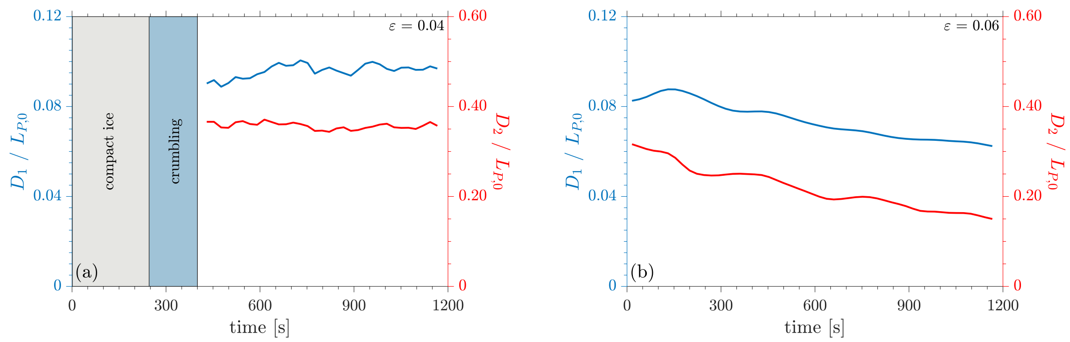

FIGURE 3.4: Temporal evolution of average minor axis (D_1; blue lines; left-hand axes) and major axis (D_2; red lines; right-hand axes) of ice floes 15–30 m from the wave maker, and normalised with respect to the incident wavelength, $L_{P,0} = 4\,\mathrm{m}$: (a) $\varepsilon = 0.04$, (b) $\varepsilon = 0.06$ tests. Note the different ordinate axis limits used for the minor and major axes.

Figure 3.5 shows the floe size distributions for the intermediate (top) and large steepness (bottom), as major vs. minor axis scatter diagrams (left panels) and probability density functions (right). The data include all floes detected from the image processing over the full 1200 s of the tests, i.e. all floes detected (within the quality filter) from every image taken. For both the intermediate and large steepness, the linear fits on the scatter diagrams reveal the aspect ratio is approximately $D_1{:}D_2 = 1{:}3$ (eccentricity $e = 2c/D_2 \approx 0.5$, where $c = \sqrt{(D_2/2)^2 - (D_1/2)^2}$), confirming the elongated floe shapes. The minor axes have narrow, bell-shaped probability density functions, with a mode of 6%, and 50% of the floes in the 5–11% range. In contrast, the probability density

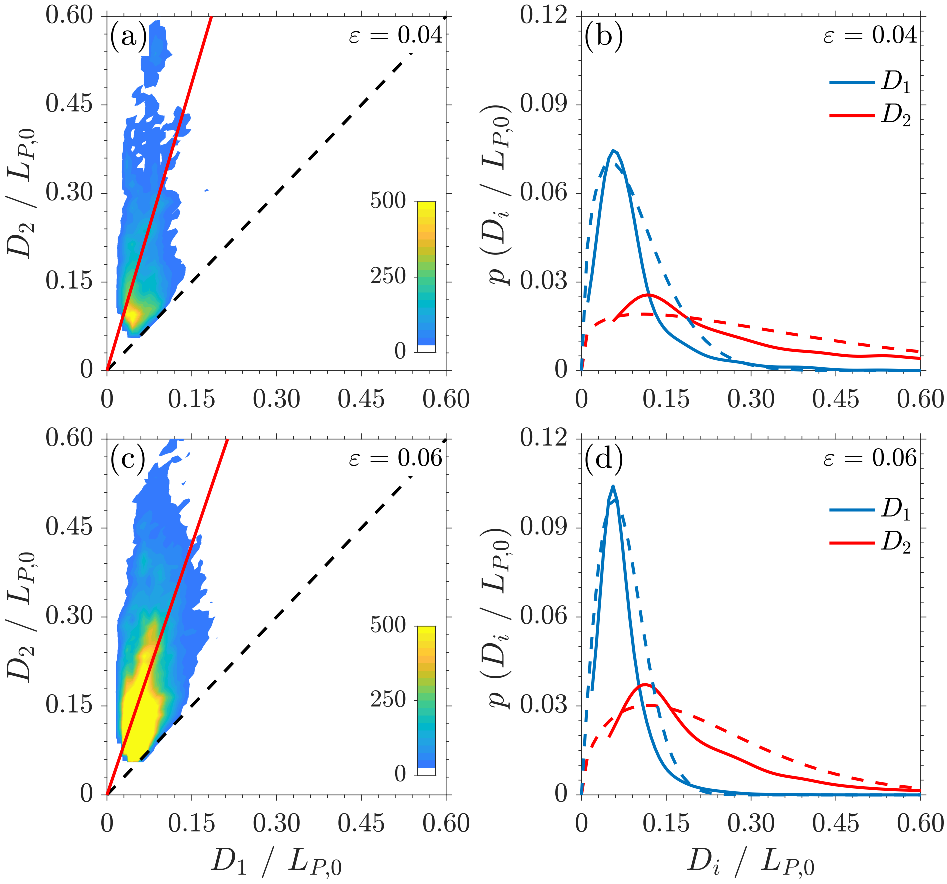

FIGURE 3.5: (a,c) Scatter diagrams of normalised major (D_2) versus minor (D_1) axes, with linear fits (solid red lines) and 1:1 correlations (dashed black lines), for (a) $\varepsilon = 0.04$ and (c) $\varepsilon = 0.06$. (b,d) Floe size distributions expressed as probability density functions of D_1 (solid blue lines) and D_2 (solid red lines), with corresponding fitted two-parameter Weibull distributions (dashed lines), for (b) $\varepsilon = 0.04$ and (d) $\varepsilon = 0.06$.

functions for the major axes are broad,with 50% of floes in the range 14–47% of the incident wavelength for $\varepsilon = 0.04$ and 11–27% for $\varepsilon = 0.06$, and with a mode $\approx$ 12% of $L_{P,0}$.

The empirical probability density functions of floe sizes are linked with wave statistics via the Weibull distribution

$$f(D_j) = \frac{\beta}{D_j}\left(\frac{D_j}{\gamma}\right)^{\beta} \mathrm{e}^{-\left(\frac{D_j}{\gamma}\right)^{\beta}}, \quad j = 1, 2, \tag{3.2}$$

where γ is the scale and β is the shape parameter. The Weibull distribution degenerates to a Rayleigh distribution for $\beta = 2$ [132], which is the statistical distribution of the incident wave amplitudes (applied at the wave maker) and, to some extent, the incident wavelengths [see discussion on distribution of wave periods and wavelengths in e.g. 133]. The Weibull function is fitted to the empirical distributions using values of β and γ derived from the maximum likelihood method [e.g. 134]. For the minor axes, $\beta = 1.6$

for $\varepsilon = 0.04$ and $\beta = 1.9$ for $\varepsilon = 0.06$, indicating the floe size in the wave direction tends to the same statistical distribution as the incident wave field as the steepness increases. Fitting of β-values is used instead of a standard goodness-of-fit test to the Rayleigh distribution, which would only confirm fitting or rejecting of the null hypothesis. For the major axes, $\beta = 1.3$ for $\varepsilon = 0.04$ and $\beta = 1.5$ for $\varepsilon = 0.06$, making the link between the floe size in the transverse direction and the wave statistics inconclusive.

3.4 Wave evolution

3.4.1 Waves-in-ice measurements

The evolution of the wave field through model ice is measured indirectly by tracking the variation of pressure below the water surface at different distances from the wave maker. In open water, pressure variations are typically converted into water surface elevations by assuming a constant (atmospheric) pressure above the water and the linear (open water) dispersion relation [e.g. 123]. The presence of ice at the water surface introduces uncertainties on both surface pressure and wave dispersion, which compromises reconstruction of the wave amplitude. To bypass the issue, the recorded pressure time series are normalised with the pressure standard deviation as recorded in open water, rather than attempting to convert them into surface elevations. The approach provides time series that measure changes of the wave field in the ice-covered water relative to the incident field. Links between wave properties and ice breakup based on using the open water dispersion relation to convert the pressure measurements into surface elevations are discussed in Section 3.5.

Figure 3.6 shows examples of normalised pressure time series at the five different pressure sensor measurement locations and for each of the three tests conducted. The evolution of the series with distance into the ice-covered water are characterised by mean amplitudes decreasing, which implies reduced energy content, mean wave periods increasing, which indicates longer wavelengths, and groupiness increasing, which implies spectral narrowing [e.g. 123]. Moreover, differences are evident in the evolution of the three incident fields. The evolution of the different incident fields are quantified and compared in Section 3.4.2 and Section 3.4.3.

The probability density functions of the crest-to-trough amplitude (A) of individual oscillations of the pressure signal (normalised by the concurrent standard deviation) are presented in Figure 3.7 as a function of the distance from the wave-maker, with the Rayleigh distribution included as benchmark. The bottom panels in the figures report the statistics of the incident wave field. The amplitude distribution in open water agrees

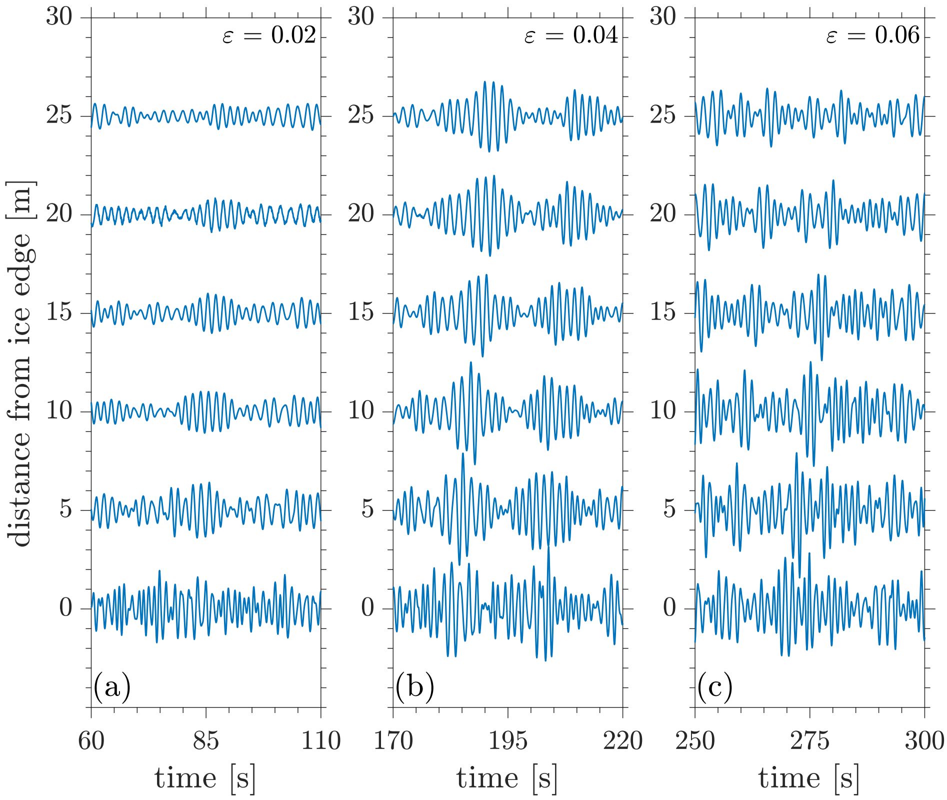

FIGURE 3.6: Time series of normalised water pressure oscillations at progressive distances from the ice edge, for (a) $\varepsilon = 0.02$, (b) $\varepsilon = 0.04$ and (c) $\varepsilon = 0.06$.

with the Rayleigh distribution, confirming it satisfies the statistics imposed at the wave maker. Statistics remain consistent with the Rayleigh probability density function as waves propagate into the ice cover, denoting the absence of any significant nonlinear wave dynamics developing within the tank [cf. 124, 126] and hence confirming linear wave physics as the relevant driver for wave evolution in the tests.

3.4.2 Wave spectrum evolution

Figure 3.8 shows the wave spectrum, $S(f)$, at each of the measurement locations and for each test, as a function of normalised frequency, $f/f_{P,0}$. The incident spectra, $S_0(f)$, from the benchmark tests (without ice), are shown for reference. The spectra are calculated as ensemble averages of the Fourier transform of 13.7 s intervals (4096 data points) of the normalised pressure time series with 50% overlap. Therefore, the spectrum at a specific location represents the change of pressure energy relative to the incident counterpart [noting that the relative pressure energy is proportional to the relative wave energy, see 123]. Evolution of the spectra over distance into the ice-covered water is quantified in terms of their spectral variance (m_0, i.e. spectra integrated with respect to frequency or zeroth-order moment; due to the normalisation of the pressure time series,

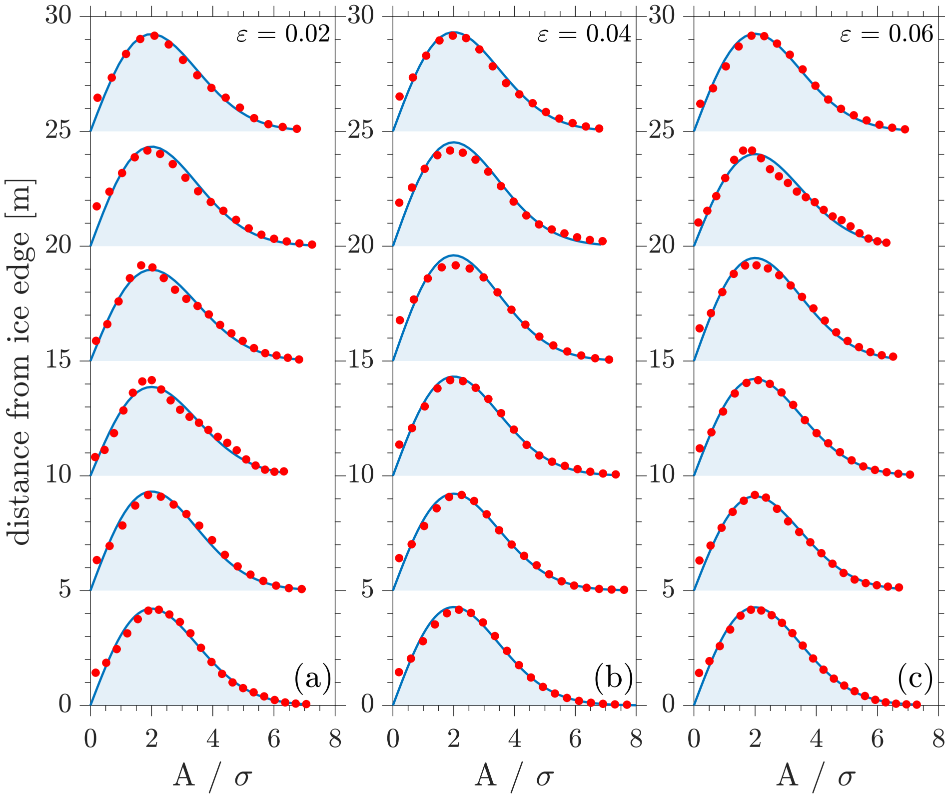

FIGURE 3.7: Empirical probability density function of the crest-to-trough amplitude (A) of individual oscillations of the pressure signal at different measurement locations normalised by the concurrent standard deviation σ (full circles), and the Rayleigh distribution (blue solid line). The distributions in the bottom row are for the incident wave field in open water.

m_0 is relative to the incident counterpart and thus takes unit value in open water), the mean wave period ($T_{01} = m_0/m_1$, where m_1 is the first order moment of the spectrum), and the frequency bandwidth (B_W, corresponding to the spectral width at one-tenth of energy content) in Figure 3.9, where each quantity is normalised by its incident wave field counterpart.

The continuous ice cover has a major effect on the energy evolution of the mild incident spectrum ($\varepsilon = 0.02$), as indicated by the corresponding time series (Figure 3.6a). The unbroken ice edge partially blocks the incident wave field, such that only ≈50% of the incident energy remains at the first measurement location (5 m from the ice edge; Figure 3.8a and Figure 3.9a) and energy then reduces at a steady rate, with only ≈20% of the incident energy remaining at the farthest measurement location (25 m from the ice edge). The sharp drop in energy at the first measurement location is attributed to reflection by the ice edge, with the reflected energy found to be ≈33% of the incident energy, i.e. accounting for two-thirds of the energy removed by the first measurement location, and energy loss due to overwash at the ice edge [see 131, 135]. A relatively sharp energy drop at the first measurement location is also visible for the intermediate

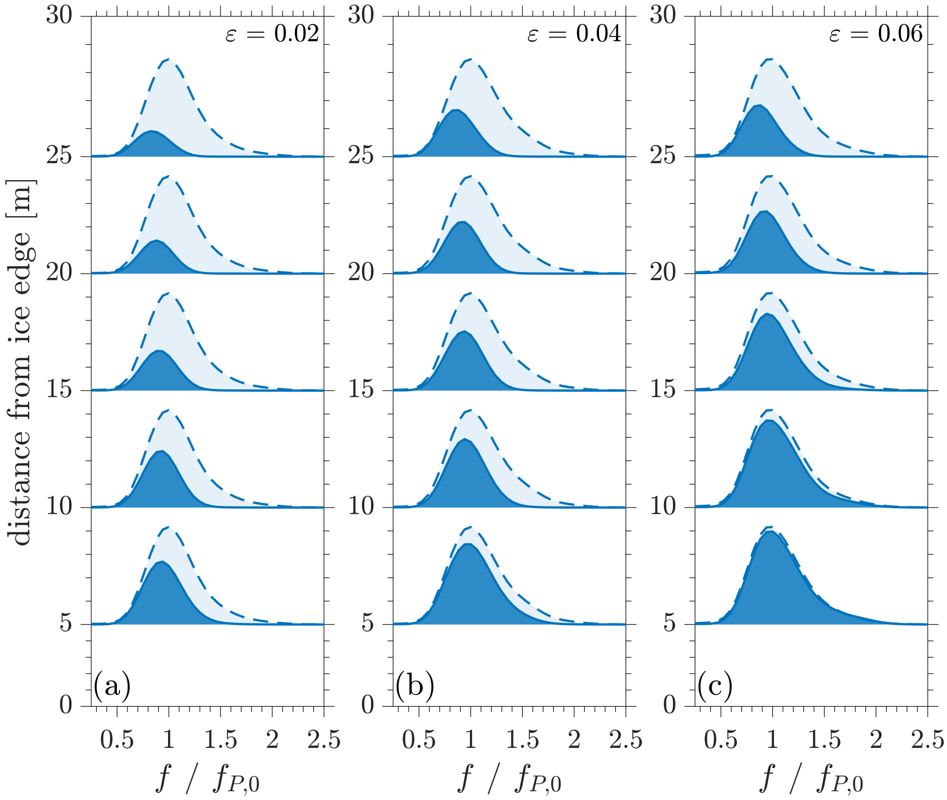

FIGURE 3.8: Wave spectra of normalised water pressure at progressive distances from the ice edge (S; dark blue shade) and corresponding incident spectra (S_0; from open water benchmark tests; light blue shaded), versus normalised frequency, for (a) $\varepsilon = 0.02$, (b) $\varepsilon = 0.04$ and (c) $\varepsilon = 0.06$.

steepness ($\varepsilon = 0.04$; Figure 3.8b and Figure 3.9b), although the drop is weaker and ≈70% of the incident energy remains. The smaller drop compared to the mild incident steepness is primarily attributed to weaker ice-edge reflection by broken ice cover (≈20% of the incident wave). The energy drops to ≈50% at the second measurement location (10 m from the initial ice edge), which is likely due to a combination of reflection by the edge of the continuous ice cover (on the wave maker side of the sensor for > 50% of the test), and wave energy dissipation during ice breakup between the first and second measurement locations. The third to fifth sensors are below continuous ice cover for the entire intermediate steepness test and the rate of energy reduction from the second to the fifth sensor is relative small, with ≈45% of the incident energy remaining at the last sensor. In contrast, for the large steepness ($\varepsilon = 0.06$; Figure 3.8c and Figure 3.9c), almost all of the incident energy is detected at the first sensor, which is unsurprising as the ice edge retreats beyond the sensor after only ≈ 300 s (the first quarter) of the test. Similarly, over 85% of the incident energy is recorded at the second sensor where the ice edge crosses around half way through the test. Wave energy drops steadily and with relatively large gradient between the second and fifth measurement locations, where the waves are propagating through broken ice for the majority of the test, with ≈35% of the

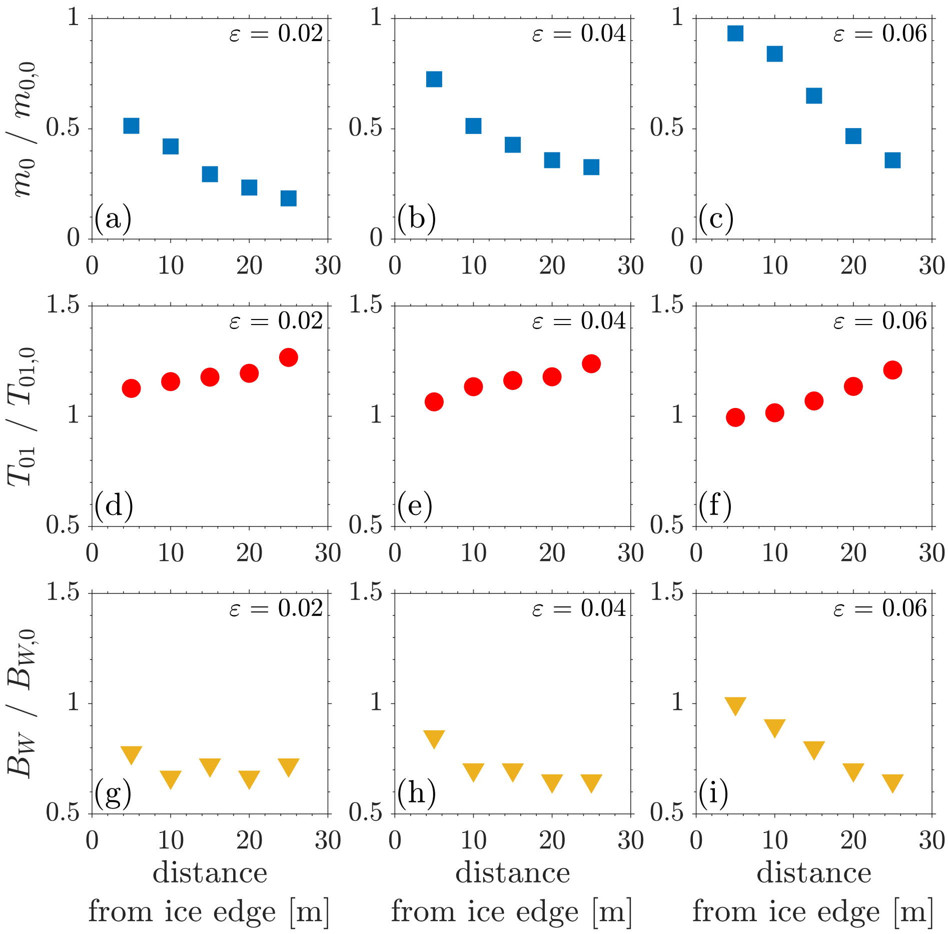

FIGURE 3.9: Wave spectrum (a–c; blue squares) zeroth-order moments, (d–f; red bullets) mean wave periods, and (h–i; yellow triangles) frequency bandwidths, versus distance from ice edge, normalised by corresponding incident wave field values, for (a,d,g) $\varepsilon = 0.02$, (b,e,h) $\varepsilon = 0.04$ and (c,f,i) $\varepsilon = 0.06$.

incident energy remaining at the farthest location.

The skewing of the spectra towards lower frequencies over distance (Figure 3.8) is attributed to ice edge reflection [136], energy loss due to overwash [135] and attenuation through continuous [137] and broken [138] ice covers being stronger for higher frequency components of the spectrum. It follows that the mean period increases with distance into the ice-covered water (Figure 3.9d–f) and the spectral width decreases (Figure 3.9g–i). Similar to the wave energy (zeroth-order moment), there are large differences between the mean period and spectral bandwidth at the first measurement location and their open water counterparts for $\varepsilon = 0.02$, and to a lesser extent for $\varepsilon = 0.04$. The mean periods then steadily increase with distance. The spectral bandwidths decrease from the first to the second measurement location, and then show only a modest decrease. For $\varepsilon = 0.06$, the mean period and spectral bandwidth are indistinguishable from their open water counterparts at the first measurement location, and then increase (mean period) and decrease (spectral bandwidth) with larger gradients than in the smaller steepness tests. For all three tests, at the farthest measurement location, the mean periods are $T_{01} = (125\% \pm 3\%)\, T_{01,0}$ and spectral bandwidths $B_W = (67\% \pm 4\%)\, B_{W,0}$.

3.4.3 Attenuation rate

Assuming each frequency component of the wave spectrum attenuates exponentially [91] in continuous and broken ice, the attenuation coefficient (exponential attenuation rate) is

$$\alpha(f; d) = -\frac{\log[S(f)/S_0(f)]}{d}, \tag{3.3}$$

where d is the distance from the initial location of the ice edge (i.e. 10 m from the wave maker). For each test, a single value of α per frequency is estimated using least squares regression [e.g. 134] on data from all probes. Figure 3.10 shows α versus normalised frequency over an interval covering the most energetic part of the spectrum ($0.5 \leq f/f_{P,0} \leq 1.8$). The 95% confidence intervals indicate the attenuation coefficient values are, in general, robust for approximately $0.8 \leq f/f_{P,0} \leq 1.4$, over which the attenuation coefficients increase monotonically with frequency, and become uncertain towards the spectral tails, where the mean values of the attenuation coefficient are relatively insensitive to frequency.

Field measurements (assumed to be mainly in broken on unconsolidated ice conditions) suggest a power-law dependence of the form [137]

$$\alpha(f) \propto f^n, \quad \text{where} \quad 1.9 \leq n \leq 3.6, \tag{3.4}$$

although theoretical scattering models suggest larger exponents [$n \geq 8$; 32]. Based on (Equation 3.4), reference slopes $\alpha(f) \propto f^2$ (yellow dashed lines), $\alpha(f) \propto f^3$ (red) and $\alpha(f) \propto f^4$ (green) are included in Figure 3.10, and set to coincide with the empirical attenuation coefficients at the spectral peaks ($f/f_{P,0} = 1$). Over the interval in which the empirical measurements are robust ($0.8 \leq f/f_{P,0} \leq 1.4$), they are, in general, bounded by the reference slopes, indicating consistency between the attenuation rate in the physical model and in field measurements. For each incident steepness, the empirical attenuation is visibly closer to references slope $\alpha(f) \propto f^3$ and f^4 than f^2. Based on the root mean square error over $0.8 \leq f/f_{P,0} \leq 1.4$, the empirical attenuation is marginally closer to $\alpha(f) \propto f^4$ than f^3 for the mild and large incident steepness tests (0.0117 vs. 0.0162 for $\varepsilon = 0.02$ and 0.0046 vs. 0.0066 for $\varepsilon = 0.06$), and significantly closer to $\alpha(f) \propto f^4$ for the intermediate incident steepness test (0.0040 vs. 0.0185 for $\varepsilon = 0.04$). Therefore, the power-law dependencies of the empirical attenuation coefficients on frequency are at the top end or just above the range derived from field measurements, which is attributed to the influence of breakup in the tests (to the best of our knowledge breakup did not occur during the field measurements) or, possibly, due to the scaling of the model ice (more compliant than natural sea ice at field scale).

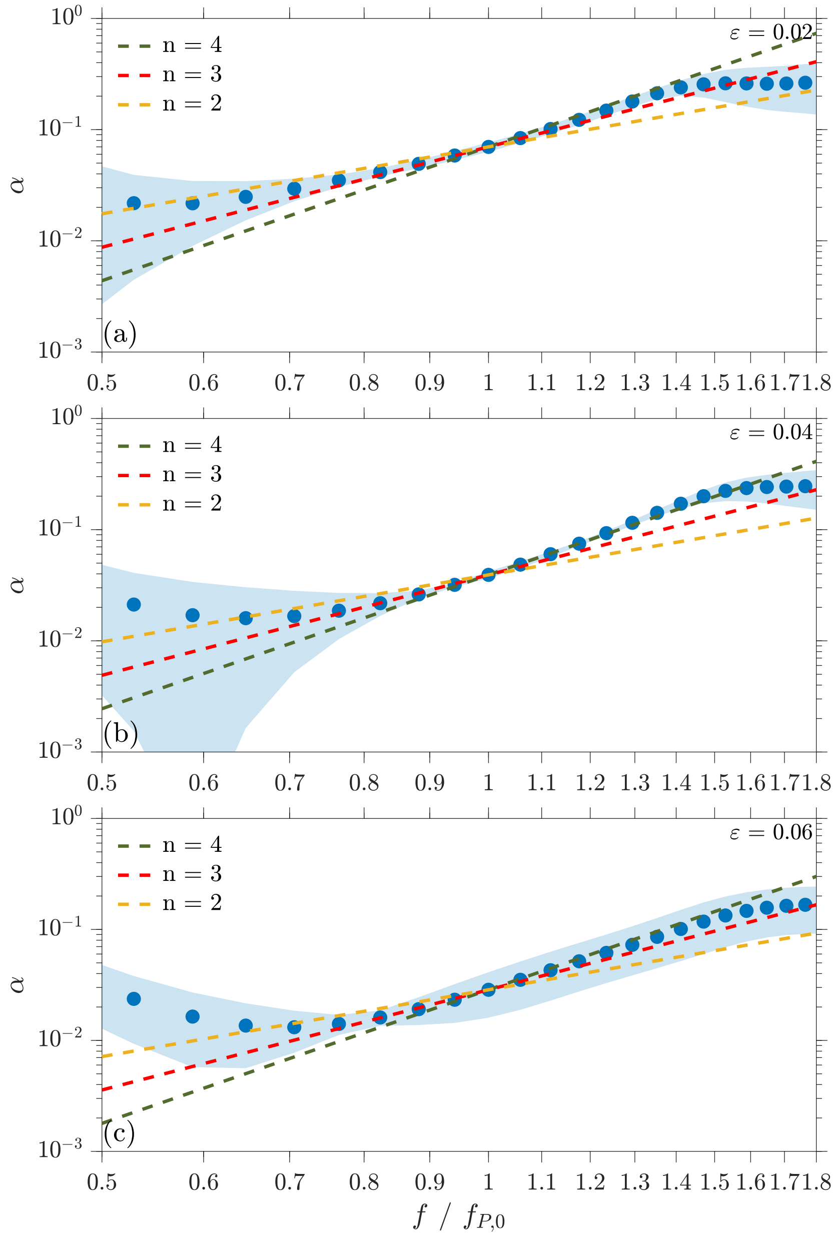

FIGURE 3.10: Empirical wave energy attenuation coefficients (α) as functions of normalised frequency (blue circles), with 95% confidence intervals (shaded area) and reference slopes $\alpha \propto f^n$ (dashed lines) that intersect the empirical data at $f/f_{P,0} = 1$, for (a) $\varepsilon = 0.02$, (b) $\varepsilon = 0.04$ and (c) $\varepsilon = 0.06$.

3.5 Discussion and conclusions

A physical model of interactions between irregular ocean waves and sea ice conducted in an ice tank using a Pierson–Moskowitz incident spectrum and doped model ice has been reported. Three tests were conducted, starting with a continuous ice cover, and with the wave incident steepness (ε) increased between tests. The impact of the incident waves on the ice cover ranged from causing no breakup for the mildest incident field to breakup of the entire length of the ice cover and retreat of the ice edge for the largest steepness. Breakup occurred both in the longitudinal (wave propagation) and transverse directions, and the resulting floes were shown to be well approximated by ellipses of aspect ratio 1:3. Evidence was found of the floe size distribution in the wave propagation direction tending towards the Rayleigh distribution, similar to the distribution of incident wave amplitudes. In contrast, the floe size distribution in the transverse direction was found to be widely spread.

Wave evolution in the ice-covered water was monitored by tracking the transformation of the subsurface pressure field with an array of bottom mounted pressure sensors. The spatial wave evolution varied considerably between tests as inferred by wave-induced pressure attenuation, mean period increase of pressure oscillations and narrowing of the spectral bandwidth. However, statistical properties of the wave field did not change appreciably over distance into the ice-covered water, fitting a Rayleigh distribution throughout the tank, and indicating that nonlinear wave dynamics did not develop during the tests. The edge of the continuous ice cover was found to have a major impact on the properties of the wave-induced pressure field (amplitude, mean period and spectral bandwidth), with differences relative to the incident condition being reduced (or removed) when the ice at the edge was broken, likely due to weaker reflection of the incident wave field. The (exponential) energy attenuation rate in the ice-covered water showed a power-law dependence on frequency, similar to that found from field measurements and with a comparable exponent.

Models for wave-induced ice breakup depend on the relationship between the wave height and period [or wavelength; e.g. 71, 78–80], with breakup more likely for larger wave heights and shorter periods, i.e. larger steepness values. Correlations between ice breakup and wave heights and periods in the tests are investigated by assuming the open water linear dispersion relation can be used to convert pressure into the surface elevation in the presence of ice cover [see, e.g., 134, for details of the conversion]. A zero-crossing analysis is applied to the time series of the surface elevation to extract individual wave heights (H) and periods (T) and hence steepness, which is calculated as $kH/2$, where k is the wavenumber associated to the water period (T). Both down- and up-crossing conditions are considered to extract a sufficiently large population [see e.g. 134]. Figure 3.11 shows the joint distribution of individual wave heights and related periods recorded at (a) locations where the ice remained unbroken throughout a test, which includes data from the $\varepsilon = 0.02$ and 0.04 tests, and (b) locations where ice transitioned from unbroken to broken in a test, which includes data from the $\varepsilon = 0.04$ and 0.06 tests. Lines of constant steepness, representing the average and maximum steepness for each dataset

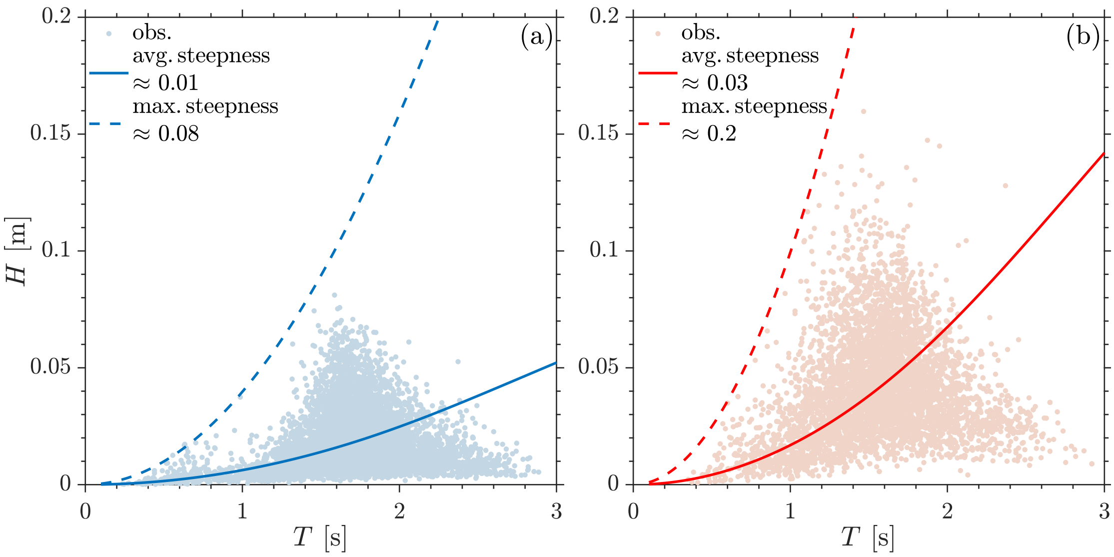

FIGURE 3.11: Empirical joint distribution of individual crest-to-trough wave heights and periods as a function of the ice configuration: (a) observations recorded in unbroken ice during the entire experimental tests (merges data obtained with incident wave fields with small and intermediate steepness, $\varepsilon = 0.02$ and 0.04, respectively); (b) observations obtained during the transition from unbroken to broken ice (merges data obtained with incident wave fields with intermediate and high steepness, $\varepsilon = 0.04$ and 0.06, respectively). Lines of constant steepness (average and maximum for each distribution) are reported as benchmarks.

(hence an indication of the strength of the the wave field), are included as benchmarks. For unbroken ice, wave heights do not exceed ≈ 0.07 m, which is about 1.5 times the significant wave height in open water, and wave periods are up to ≈ 3 s, which corresponds to about two times the peak period of the incident wave field. The wave height assumes maximum values for periods comparable with the peak period of the incident field. Wave heights tend to decrease for shorter and longer periods, with a greater decrease towards shorter periods. Wave heights and periods distribute along a small average steepness of ≈ 0.01, which is half the characteristic steepness of the mildest incident wave field tested (i.e. the joint distribution is flatter than its open waters counterpart), and are limited by an upper bound corresponding to a maximum individual wave steepness of ≈ 0.08, i.e. more than five times smaller the one of a breaking wave [cf. 125]. Less than 1% of waves have steepness between 0.05 and 0.08, and, thus, wave-induced loads on the ice cover are expected to be weak, preventing breakup. In contrast, when the ice transitions from unbroken to broken, individual wave heights reach much larger values, with the maximum ≈ 0.15 m, which is about two times the incident significant wave height for $\varepsilon = 0.04$. The shape of the distribution more closely resembles the joint distribution in open water. The average steepness is ≈ 0.03, which is three times as large as for the unbroken ice, and the maximum steepness is ≈ 0.2, which is greater than the maximum for the unbroken ice by a factor of 2.5 and about half the steepness of a breaking wave. More than 10% of waves exceed the maximum steepness for the unbroken ice, indicating a more substantial load on the ice cover and justifying the transition to broken ice.

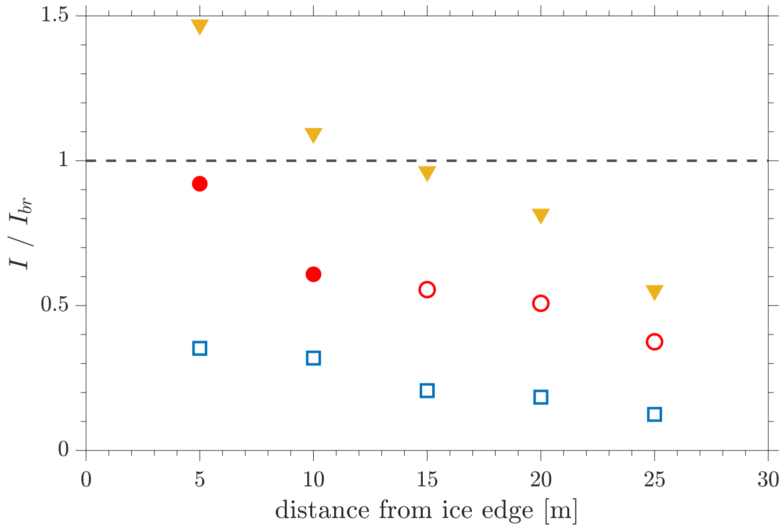

FIGURE 3.12: Breaking parameter, I, normalised by proposed breaking threshold $I_{br} = 0.014$ [2], versus distance from ice edge for $\varepsilon = 0.02$ (blue), $\varepsilon = 0.04$ (red) and $\varepsilon = 0.06$ (yellow), with locations where breakup occurs (bullets) and does not occur (circles) indicated.

Results in Figure 3.11 only consider the state of the ice cover, and do not incorporate information on its mechanical properties. A wave-induced breakup parameter that merges both wave and ice characteristics has been proposed as [2]

$$I = \frac{H_S\, h\, E}{2\, \sigma\, L_P^2}, \tag{3.5}$$

where the significant wave height H_S is calculated as four times the standard deviation of the surface elevation time series at measurement locations, and the wavelength, L_P, is calculated using the open water dispersion relation at the peak period [consistent with 2]. Note that I depends on the ratio of H_s to L_P, which is proportional to the wave steepness (by a factor $2\,\pi$). Figure 3.12 shows the values of I for each test and each measurement location, normalised by the universal breaking threshold $I_{br} = 0.014$ proposed by Voermans et al. [2], and indicating whether the ice is broken for the test and location. In each test, the values of I decrease with distance, as the significant wave height decreases and the wavelength (peak period) increases with distance. In the small steepness test, the ice is unbroken at all locations and $I < 0.55\, I_{br}$. The intermediate steepness wave field breaks the ice at the first two measurement locations, but the breaking parameter is less than the proposed threshold with $0.55\, I_{br} < I < 0.95\, I_{br}$ [low values of the breaking parameter are also reported in 139, for experiments with model ice of different characteristics]. The largest steepness breaks the ice cover at all locations and the breakup parameter spans the range $0.55\, I_{br} < I < 1.47\, I_{br}$, i.e. it takes values less than and greater than the proposed threshold. Note that some test and location combinations at which broken ice is indicated, the ice cover is unbroken for part of the test, and the measurements during the unbroken phases are included in the calculations of the significant wave heights and wavelengths, which adds some uncertainty to the relationship between the breakup parameter values. Therefore, although the value $I = 0.552\,I_{br}$ at the deepest measurement location for the largest steepness test where the waves break the ice, is slightly less than $I = 0.555\,I_{br}$ at the middle location and intermediate steepness test where the ice was unbroken, the results do not necessarily contradict the existence of a threshold for waves to break the ice in terms of the breakup parameter (for the particular experimental conditions).

In conclusion, the results and findings advance beyond previous physical models of coupled wave attenuation due to sea ice and wave-induced breakup [particularly 30] by using model ice, irregular unidirectional incident wave fields and the three-dimensional nature of the facility, allowing transverse breakup. The dataset generated new insights on (i) the spatial and temporal evolution of the ice breakup when waves are the only forcing, and (ii) the wave evolution and attenuation through a ice cover that transitions from a continuous to broken. This will empower assessments of combined attenuation and breakup theories.

Chapter 4

Field Observations in the Southern Ocean: Sea Ice Image Acquisition and Preprocessing

4.1 Introduction

In the following chapters, segmentation techniques are applied to sea ice imagery acquired in-situ. Understanding the differences between sea ice images taken in the field and those created in controlled experiments is crucial for implementing ice floe segmentation techniques that are suitable to assess in-situ data. In laboratory experiments, variables such as illumination and the ice's texture can be meticulously controlled. Furthermore, the model ice breaks into predominantly rectangular floes (albeit with some irregularity), leading to images with uniform clarity, as seen in Chapter 3. The ice tank's size also serves as a reference of known dimensions, used for geometric adjustments to ensure the images accurately reflect the true sizes of the ice floes. Conversely, in-situ sea ice imaging introduces unpredictability due to ever-changing field conditions. Variations in illumination, the presence of diverse ice types, and irregular floe sizes and shapes result in a heterogeneous dataset of images. Therefore, only a minority of images display ice under conditions that can be considered optimal, in stark contrast to the consistency found in laboratory settings.

In this chapter, sea ice imagery acquired from an icebreaker is detailed, showcasing sea ice images across a broad spectrum of field conditions. These vary from optimal to challenging scenarios, including low ice gradient, non-uniform illumination, nighttime darkness, and crowded scenes of irregular ice floes. The significant perspective distortion observed in in-situ images poses a particular challenge due to the lack of a size reference for correction. Consequently, sophisticated orthorectification, based on the camera's parameters and its position relative to the ice-covered ocean, becomes necessary. In addition, manual segmentation is performed on a subset of these images, serving as a benchmark for the evaluation of subsequent automated segmentation methods (Chapter 5, Chapter 6). A sensitivity analysis is also conducted to examine how ship motion, resulting from navigation in rough ocean waters, affects the accuracy of ice floe size estimation. This analysis seeks to quantify the impact of the ship's oscillations on the quality of the final images and, thus, the precision of size distribution calculations. Through all these processes, the complexities of managing and analyzing sea ice images under field conditions for accurate quantitative analysis are explored.

4.2 Image acquisition

Close-range optical sea ice imagery was acquired underway from a sensor installed on the icebreaker S.A. Agulhas II, during three winter expeditions to the Antarctic MIZ in the Eastern Weddel Sea and the Western part of the Indian Ocean sector. For the following chapters, we primarily focus the discussion on data acquired during an austral winter expedition in the Eastern Weddell Sea (Figure 4.1) in July-August 2022, which was part of the Southern oCean seAsonaL Experiment (SCALE [140]). The sea ice region was reached at approximately 58 degrees South and 1 degree West on 19 July 2022 (Figure 4.1b). The vessel then continued along a Southward route until it reached consolidated sea ice at latitude 58.8°S (≈85 km from the ice edge). Overall, the expedition spent six days in the MIZ before heading back North [see details on the expedition in 11].

The sensor consisted of a GigE monochrome industrial camera (Figure 4.1a) equipped with 2/3" Sony CMOS Pregius sensors and 5 mm F1.8 C-mount lenses (angle of view ≈120 degrees). It was mounted on the port side of the monkey bridge at 25 m above the water line and tilted by ≈70 degrees relative to the ground. The field of view covered a portion of the ocean surface of $\approx 200{\times}200$ m^2. Images were recorded continuously with a resolution of 1920×1080 pixels and at a sampling rate of 1 Hz. The camera was paired with an Inertial Measurement Unit (IMU) to monitor the vessel's motion at a sampling rate of 10 Hz. Flashlights were used to illuminate sea ice overnight.

During the expedition, around 90,000 images were collected, with approximately 70% capturing complex ice scenarios. This significant portion includes images taken in the darkness of night or featuring irregularly shaped and densely packed ice floes with varying gradients. To accurately reflect the diversity of conditions encountered, three images,

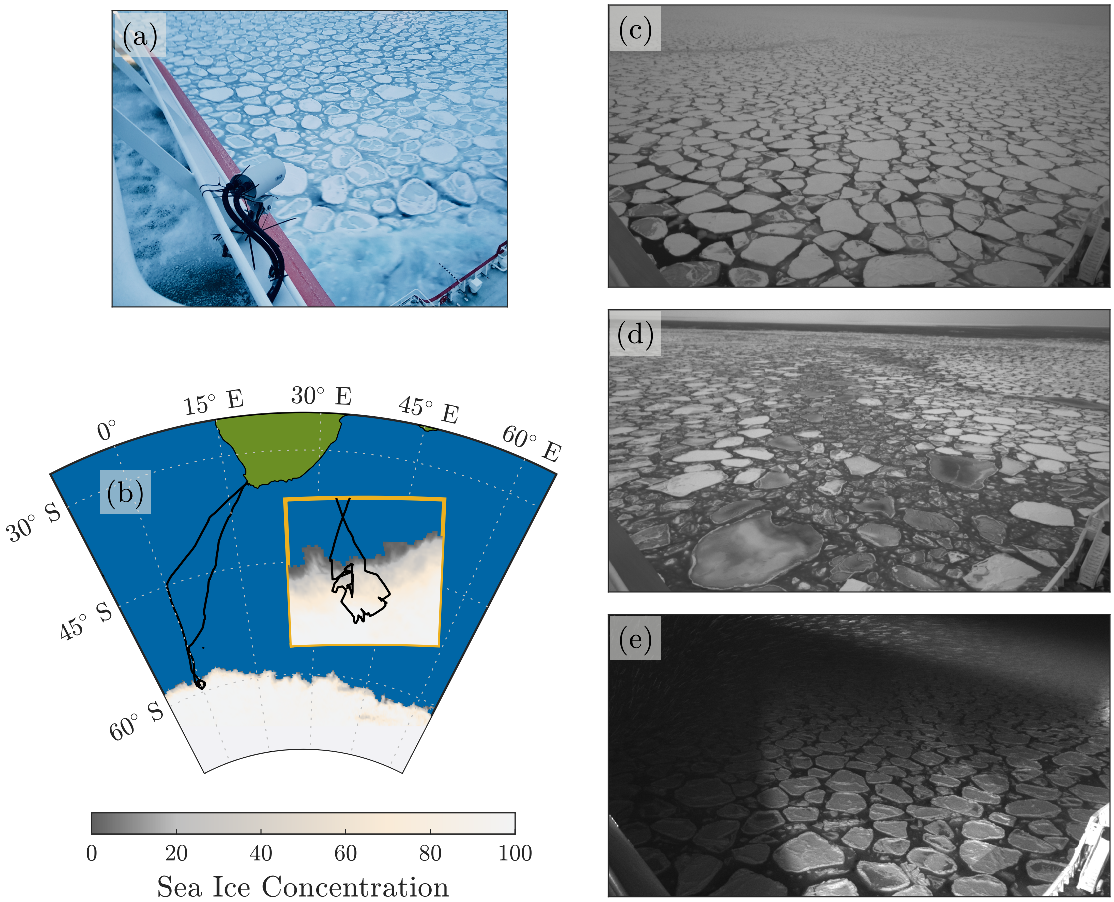

FIGURE 4.1: Antarctic SCALE expedition, winter 2022: (a) camera mounted on S.A. Agulhas II; (b) ship's track; (c) high-resolution image of the sea ice surface obtained under clear sky conditions; (d) exhibiting varying ice gradients; (e) taken at nighttime.

each exemplifying a distinct scenario, were selected; sample images are reported in Figure 4.1c-e. These images form the basis for evaluating image segmentation techniques for sea ice applications. While many image processing methods perform well under ideal conditions, field conditions seldom meet this criterion, presenting a non-uniform and unpredictable environment.

4.3 Camera calibration

Camera calibration is a pivotal step in image processing, especially critical in domains such as robotics and navigation where precision is fundamental to functionality and effectiveness. The aim of camera calibration is to correct lens and perspective distortions arising from the inherent characteristics of cameras and their environmental context. By addressing these distortions, it becomes possible to accurately measure objects within images using real-world units. This makes camera calibration an essential preparatory step for computer vision tasks that require a detailed understanding of object size, shape, and position.

The calibration process involves estimating parameters within the so-called camera matrix, a mathematical model that represents how a camera maps the 3D world space onto a 2D image plane. This matrix consists of intrinsic parameters – focal length, optical center, and pixel size in world units – affecting how the image is formed, and extrinsic parameters, describing the camera's spatial position and orientation. The intrinsic parameters are derived from a calibration process [a common method is presented in 45], which evaluates image distortion by analysing multiple images of a planar pattern with known geometry [a chessboard; see technical details in 141, 142]. Estimation of these parameters necessitates a known correlation between the 3D world coordinate system and the 2D image points. Zhang's methodology [45] employs the distinctive square corners of the chessboard, which are automatically detectable in the images, while the corresponding 3D world coordinates are determined using the known dimensions of the chessboard's squares. Due to their minimal size, these corner points are particularly beneficial for calibration as they are highly resistant to the effects of perspective and lens distortion, thus ensuring more accurate parameter estimation.

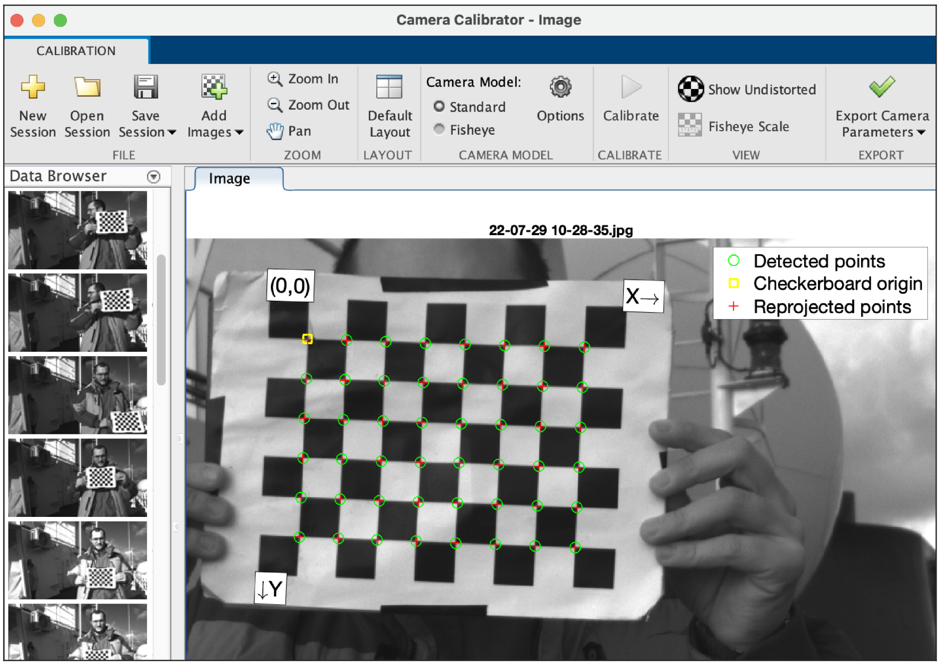

FIGURE 4.2: Computer Vision Toolbox for Camera Calibration in MATLAB.

The calibration was conducted using the Computer Vision Toolbox available in MATLAB [142] (see Figure 4.2). Forty chessboard images, spread across the camera's field of view (refer to Figure 4.3), were taken to reduce uncertainties and secure optimal calibration results. Notably, while theory advises the use of an asymmetric chessboard for enhanced orientation detection during calibration, the critical task of identifying the chessboard's corners and utilizing them for intrinsic parameter estimation can be accomplished with either type of chessboard. Calibration was executed both before and after the expedition to confirm the consistency of intrinsic features throughout the campaign.

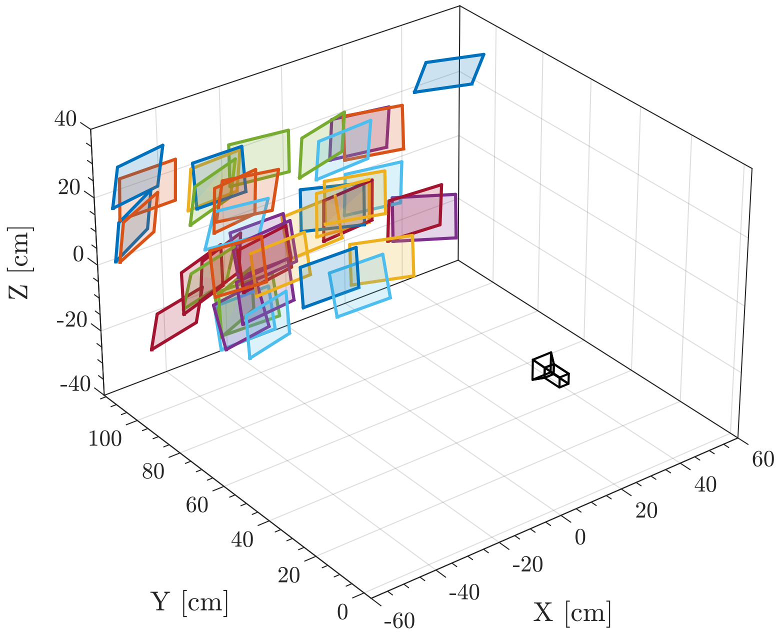

FIGURE 4.3: Chessboard images distributed across the camera's field of view.

After completing the calibration, its accuracy was verified through the analysis of reprojection errors. These errors are measured as the distances, in pixels, between the corner points identified in the calibration images and the positions of these same points when reprojected using the parameters of the estimated camera matrix. The average reprojection error was found to be less than one pixel, the smallest unit measurable in an image. This low level of error indicates that the calibration is sufficiently precise for correcting perspective distortions, demonstrating a high degree of accuracy in aligning digital image representation with the physical world.

4.4 Orthorectification

The tilt of the sensor produces a perspective distortion so that ice floes close to the camera appear bigger than those at a farther location. This creates inconsistencies in the scaling, which changes throughout the imagery scene and, hence, compromises the pixel-to-metre conversion. Therefore, a correction process that rectifies the sensor orientation, known as orthorectification, was applied to rearrange the displaced pixels as if the image were aligned with the focal plane (i.e. pixels are projected onto a plane perpendicular to the optical axis).

The process relies on the interpolation of the pixels in the original image as a function of the camera projection matrix, which maps the conversion from a three dimensional point cloud in the real world into a two dimensional plane (the image) through intrinsic and extrinsic parameters [143]. The former depends on how the sensor captures the images and includes, but they are not limited to, the focal length, aperture, resolution, and the optical center of the camera's sensor. The extrinsic parameters, on the other hand, describe the translations and rotations of the sensor relative to a reference Cartesian coordinate system. For simplicity, the camera was centered at the origin of the horizontal axis, so that translations in the x and y directions were nil and at a height of 25 m above the water line. The rotations encompass three components: the tilt around the transverse axis, which was applied during deployment; the roll around the optical axis, which was negligible assuming alignment with the horizon; and the heading around the vertical axis, which aligned with the sensor's direction. The latter is relevant only if the target is a specific object in the field of view, but it becomes negligible if the target is an extended portion of the image (the ocean surface in the present application). In the absence of any external forcing such as the ship motion, translations, and rotations are constant over time. A sensitivity analysis relative to ship motion is discussed in Section 4.6.

The orthorectification was undertaken with the CameraTransfor Python package [144]. The process was limited to a portion of the ocean surface confined into a rectangle of about 95 m × 165 m, which, based on a visual assessment over samples of images, includes clearly visible floes. The resolution (i.e. pixel-to-metre conversion) was forced to 0.05 m, to ensure both a good object accuracy and capacity of determining small-scale features in sea ice [in the order of tens of centimetres; 34]. A sample image and its orthorectified counterpart are shown in Figure 4.4.

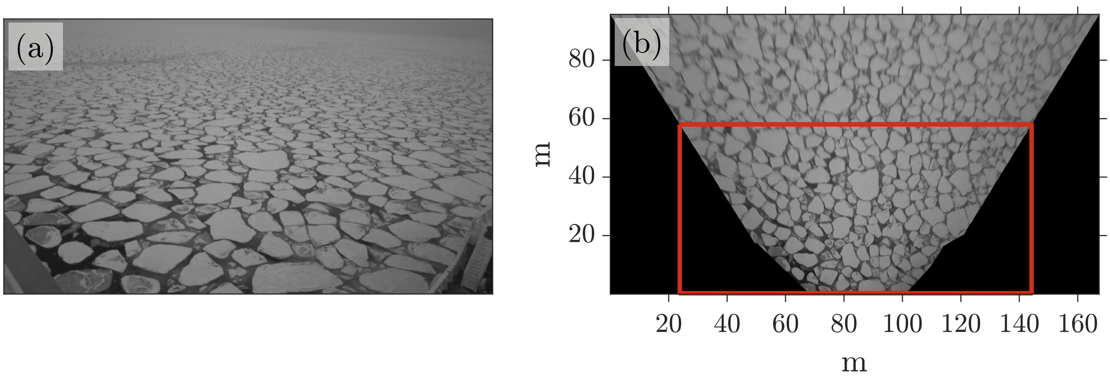

Figure 4.4: Sample image from winter 2022 after perspective correction, with the region of interest for analysis highlighted in red.

A quality check after the orthorectification revealed that floe edges loosed sharpness with distance from the sensor (see upper band of Figure 4.4b). To avoid ambiguity in the far field and, thus, reduce the risk of detecting unrealistic floes, the workable portion of the orthorectified images was restricted to an area of about 60 m × 120 m close to the sensors (see area within the red rectangle in Figure 4.4b).

4.5 Benchmark segmentation

In the field of image segmentation, establishing a ground truth is crucial. It acts as a reliable reference or true dataset, providing an objective standard to evaluate the accuracy of various detection algorithms. Manually segmenting images that depict the wide range of conditions in the Southern Ocean (refer to Figure 4.1c-e) serves to create this critical benchmark, indispensable for evaluating the automated segmentation methods discussed in subsequent chapters. The selected images display different levels of sea ice clarity, showcasing scenarios that deviate from the idealized conditions of clear ice boundaries and consistent contrast. Instead, they reflect the complex and varied realities of Antarctic sea ice, from well-illuminated scenes to those captured in nighttime darkness.

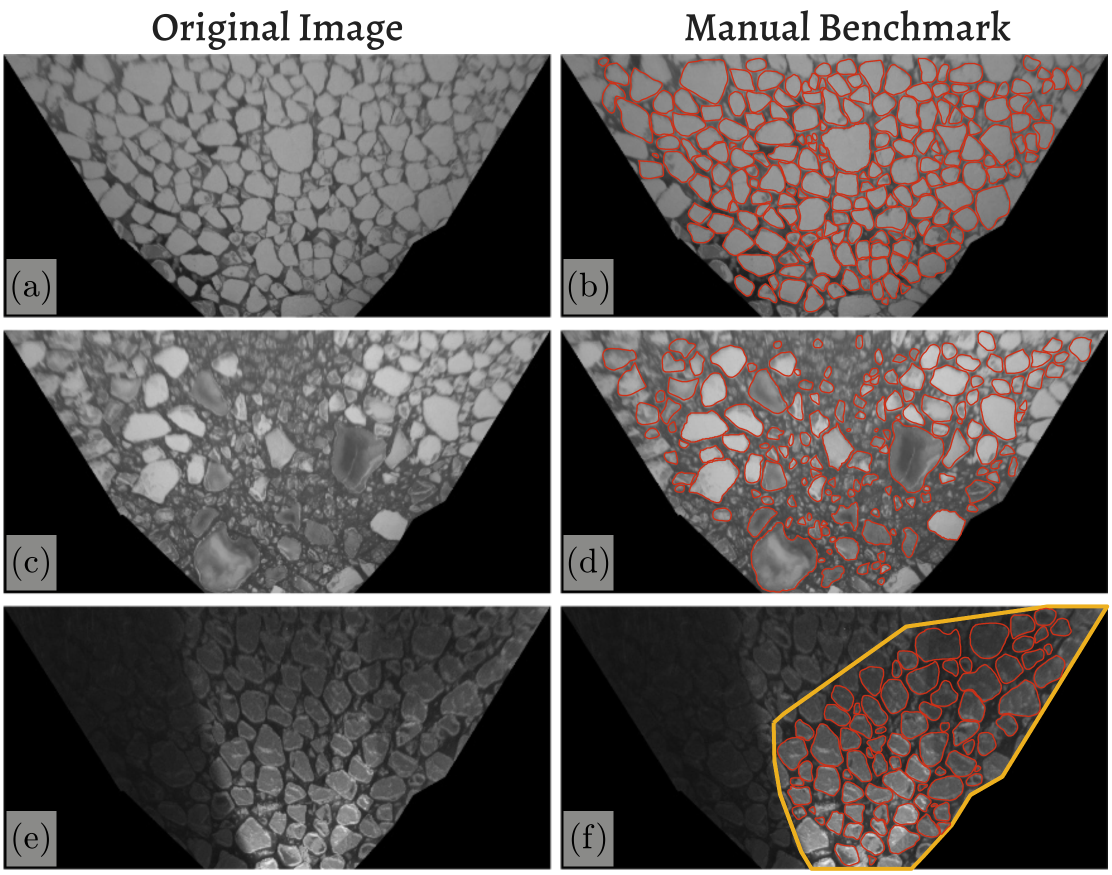

FIGURE 4.5: Sea ice images acquired under various conditions: clear (a), complex environment (c), and nighttime (e). Contours of the ice floes identified through benchmark manual segmentation are shown in corresponding images (b, d, f).

The manual segmentation was conducted using Pixelmator, a photo editing software designed for MacOS, but the process is compatible with any photo editing software. By meticulously outlining the contours of ice floes based on human observation and expertise, a set of high-fidelity reference data was created. These contours were then superimposed onto the original images to highlight the segmentation, as displayed in Figure 4.5. For nighttime images, the manual segmentation was confined to areas illuminated by the ship's lights, as the edges of ice floes become indistinct and undetectable in the darker regions of the image.

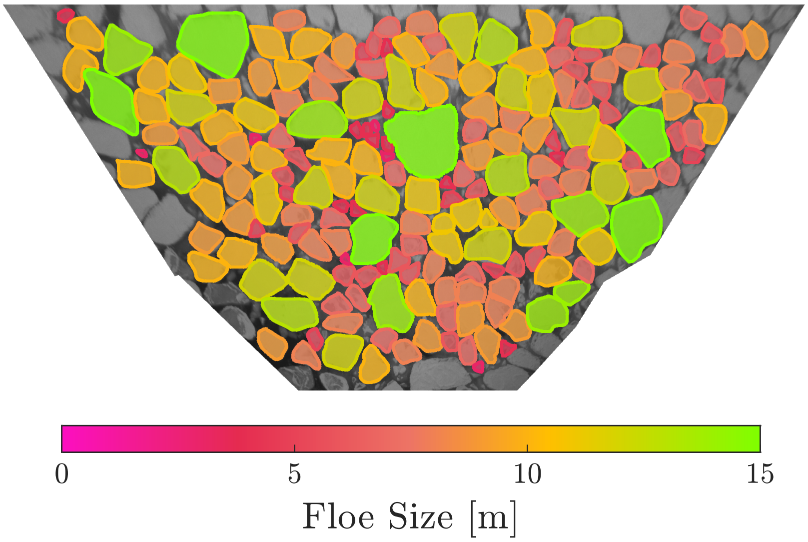

FIGURE 4.6: Sea ice floes categorized by diameter, from an image captured under optimal ice conditions.

From the manual segmentation, the parameters of each individual floe, such as size and concentration, can be extracted and analyzed. Figure 4.6 displays the resulting floe size distribution from an image with optimal ice conditions (see Figure 4.5b) as an example.

Creating this subset of manually segmented sea ice images ensures that the performance of automated detection techniques can be evaluated with precision, revealing their strengths and identifying areas for improvement.

4.6 Effect of ship motion

The orthorectification, upon which segmentation is based, relies on precise knowledge of the sensor's position and orientation (extrinsic parameters). Consistently with similar applications from mobile platforms like aircraft [16, 36] and ships [34, 42], the initial assumption was that the sensor remained fixed and, hence, the ship-induced motion was neglected. Although this hypothesis holds under relatively calm seas, the ship motion during the expedition was significant [cf. 24]. As the displacement of the supporting

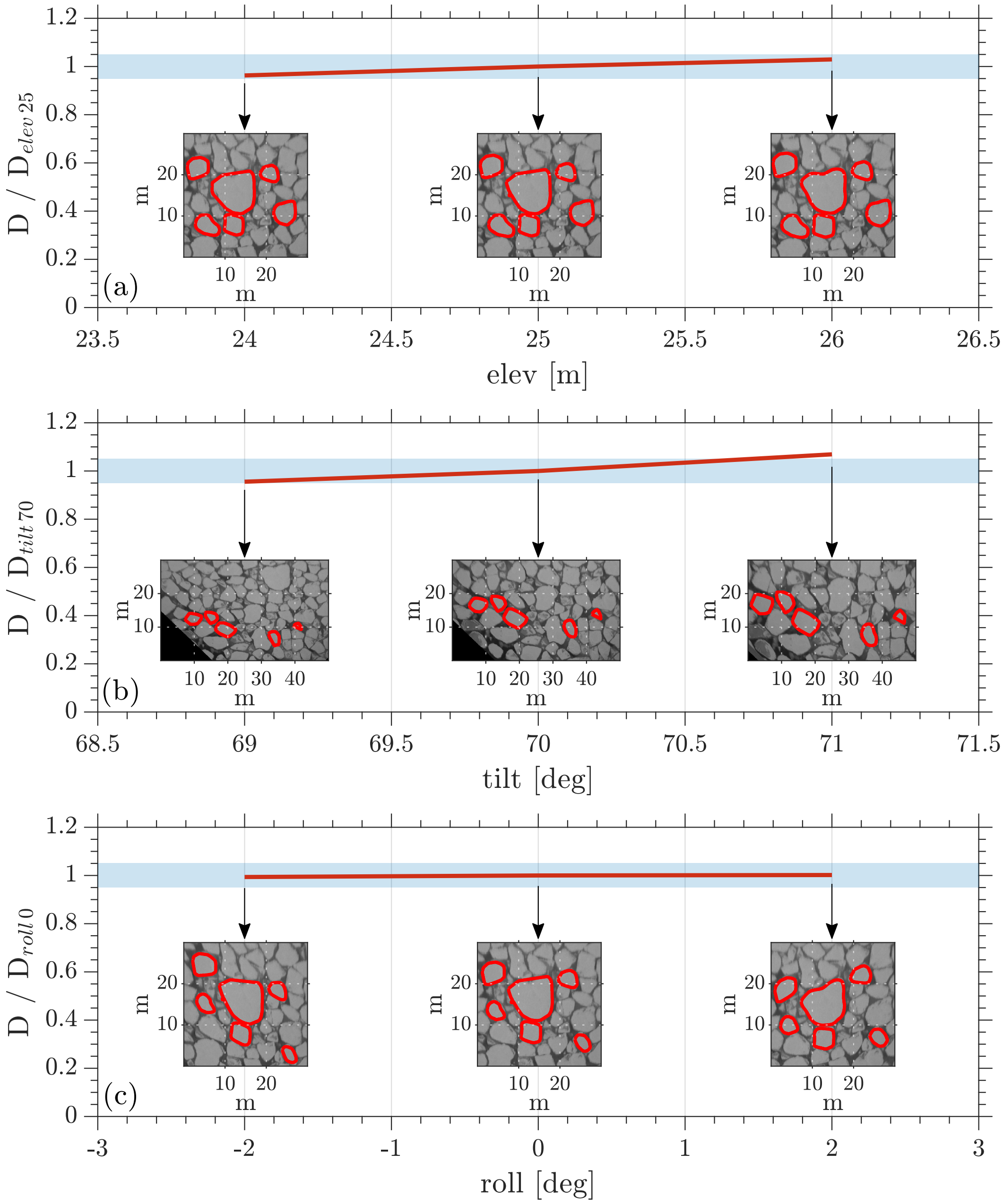

FIGURE 4.7: Uncertainty analysis of extrinsic camera parameters on the average diameter of selected ice floes, highlighted in red. The analysis includes variations of (a) elevation, (b) tilt, and (c) roll, considered independently. Variations are ± 1 m in elevation, ± 1 degree in tilt, and ± 2 degrees in roll. Diameters are normalized to those derived using reference extrinsics measured aboard the ship. The shaded blue area indicates a 5% uncertainty range.

platform can shift the camera's orientation relative to the ocean surface, it affects the orthorectification and, eventually, the estimated floe sizes.

To assess the impact of ship-induced motions, a sensitivity analysis was conducted by intentionally varying the elevation, tilt, and roll of the camera. An image captured under clear sky conditions was selected for this purpose. Orthorectification was performed with controlled misalignments from the original sensor position: $\pm$ 1 m in elevation, $\pm$ 1 degree in tilt, and $\pm$ 2 degrees in roll, consistent with extreme ship motion observations. A set of clearly distinguishable floes was then manually segmented to ensure precise comparisons of their dimensions under different motion conditions. Figure 4.7 presents the average variation in floe size, relative to the dimension extrapolated from the image with the sensor in its original position, as a function of the misalignment. Variations in elevation result in size differences within a 5% range (Figure 4.7a). Changes in tilt have a slightly larger effect, with size deviations marginally exceeding 5% (Figure 4.7b). Roll variations have the least impact, causing size changes of less than 2% (Figure 4.7c).

It should be noted that the impact of ship motion was evaluated by considering elevation, tilt, and roll independently, though in reality, they occur concurrently and could potentially interact, mitigating or amplifying overall distortion. During navigation, however, these motions tend to counteract each other due to the ship's dynamic equilibrium. Ships are designed for stability, and their natural balancing mechanisms limit these motions to maintain balance and prevent capsizing. Consequently, while tilt, roll, and elevation affect the process, their combined impact is often mitigated, minimizing the overall effect on orthorectification. The sensitivity analysis demonstrates that even with the maximum expected variations, the uncertainties remain within a manageable range, ensuring confidence in the accuracy of floe size estimations derived from orthorectified images assuming a fixed sensor position and orientation throughout the expedition.

Chapter 5

Active Contours Model

5.1 Introduction

The edge detection method presented in Chapter 3 excels in laboratory setups where variables like illumination, contrast, and the texture of model ice are known or controlled. This experimental approach mitigates common challenges associated with in-situ imaging, where unpredictable conditions, such as varying light intensity and contrast, can lead to the potential misinterpretation of floe edges. However, it also confines the efficacy of the segmentation method to the specific collection of laboratory-acquired images.

Sea ice images captured in natural environments are characterized by non-uniform illumination, shadows, impurities, and other dynamic variables that complicate the process of floe segmentation. Addressing these complexities requires adaptable image processing solutions that can identify ice floes across various conditions, which is beyond a standard edge detection method.

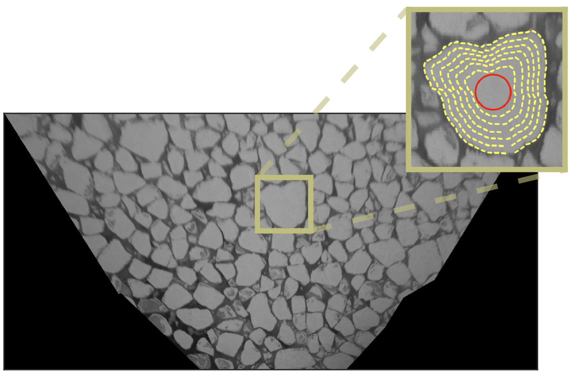

FIGURE 5.1: Illustration of the Gradient Vector Flow (GVF) method, featuring a dynamic curve that adjusts to precisely conform to the boundaries of the ice floes.

Active contour models, also known as snakes, prove to be a powerful tool for segmenting floes that are seemingly connected in the image [16], a common scenario in the Southern Ocean. They incorporate a dynamic curve that adjusts until conforming to the precise boundaries of the floes (for an example, see Figure 5.1). The Gradient Vector Flow (GVF) snake algorithm extends the capabilities of these models in detecting weak boundaries, especially when the floes exhibit a heterogeneous ice gradient. However, the efficiency of a snake-based method relies on the accuracy of the initial contour placement. If this contour does not approximate the actual floe shape closely, the curve risks converging toward incorrect results. Conversely, when the contour is positioned close to the true boundary, the GVF model accurately finds the boundary after a few iterations. An automated initial contour generator that adapts to the various ice floe shapes is then proposed in the following sections. This approach not only eliminates the need for manual contour initialization but also decreases the number of iterations required to match the edges, consequently reducing the computational time for the model's segmentation. Despite the initial contour placement, the algorithm's performance can still be influenced by the quality of the input image. Factors such as uneven grayscale distribution across floes can lead to inaccuracies in segmentation. Therefore, preprocessing that enhances the sharpness and smoothness of images is required to optimize their suitability for analysis with the GVF snake algorithm.

Herein the snake-based method is applied to the subset of images presented in Chapter 4. The results are discussed and compared with the manual benchmark segmentation.

5.2 Image enhancement

The illumination of images varied significantly within the database (see Figure 4.1c-e) due to differences in lighting and weather conditions. Consequently, the boundaries of ice floes in the raw images often remained uncertain, posing a challenge for the automation of segmentation processes [see, for example, 48].

Image enhancement techniques were applied to sharpen the edges. This was achieved through the homogenization of gray-scale levels [see, for example, 36], using a combination of an edge-preserving Gaussian bilateral filter [145] and an anisotropic diffusion filter [146]. These filters smoothed regions with low gradients while preserving the boundaries of the ice floes. Contrast enhancement was then applied using contrast-limited adaptive histogram equalization (CLAHE) [147] to accentuate the boundaries and reveal fine details (see transition from original to enhanced image in Figure 5.2a,b). It is worth mentioning that the adaptive nature of this method allows it to tailor its adjustments to the specific characteristics of each image, eliminating the need for predefined thresholds.

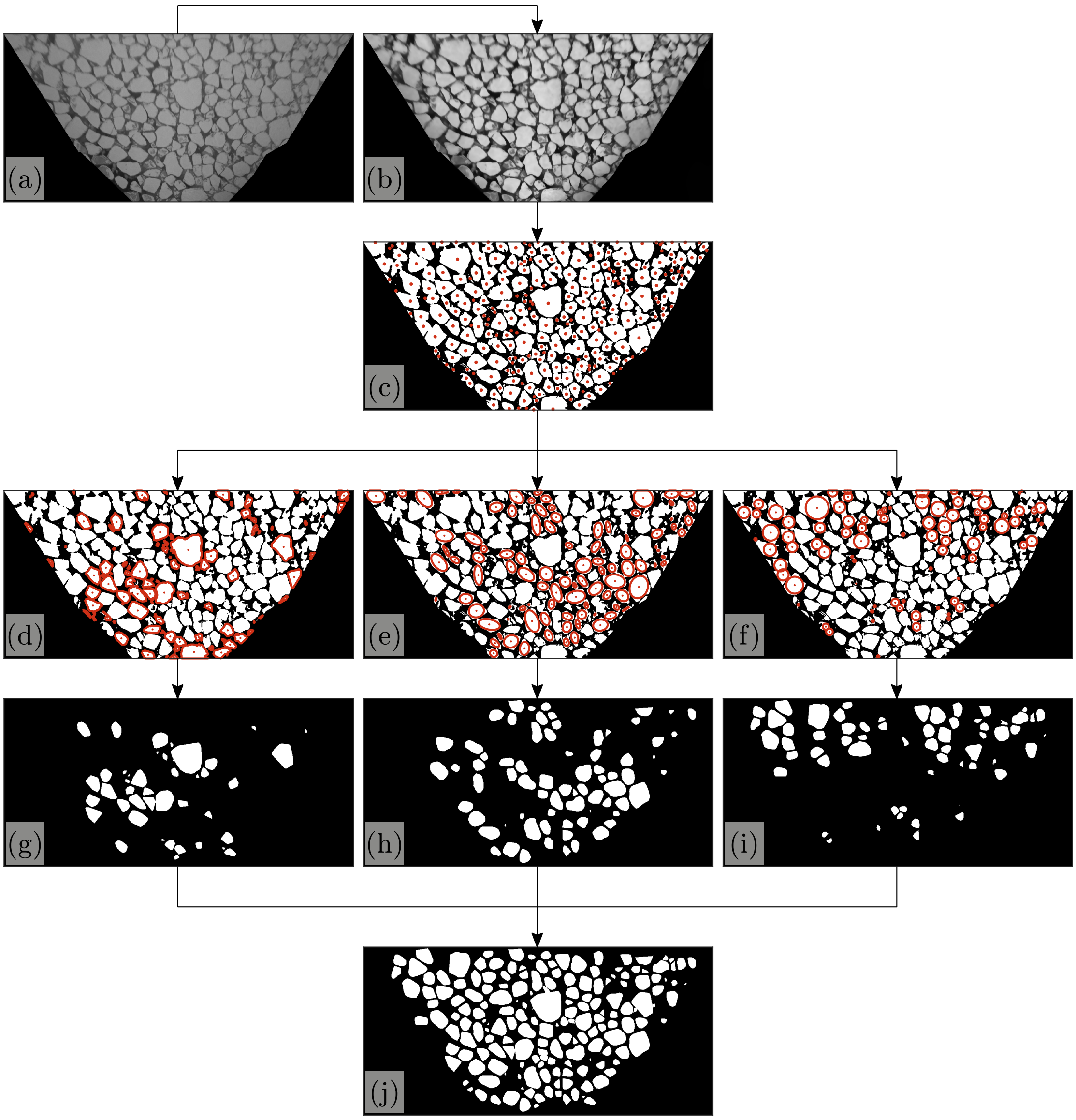

FIGURE 5.2: Ice floe detection algorithm: (a) region of interest of the image in Figure 4.4; (b) gray-level homogenization through Gaussian bilateral and anisotropic diffusion filter, and contrast enhancement using CLAHE; (c) seeds in red of the ice floes in the binary equivalent of the image; (d) perimeter in red of the floes containing a single seed; (e) elliptical initial contour in red of the floes containing a single seed after a morphological erosion; (f) circular initial contour in red for each remaining and unused seed; (g) ice floes already identified in Figure 5.2d; (h) ice floes detected by the GVF snake algorithm initialized with the elliptical contours; (i) ice floes detected by the GVF snake algorithm initialized with the circular contours; (j) final binary image with all the detected ice floes.

For night photographs, image enhancement was limited to the area illuminated by the vessel's spotlight, which was identified through haze removal techniques [148].

5.3 Gradient Vector Flow snake algorithm

The several steps for the image segmentation are illustrated in Figure 5.2. The process starts with the separation of the foreground (i.e. the objects) from the background through the transformation of the enhanced ice image into a binary counterpart (Figure 5.2c). This is achieved by selecting an appropriate threshold in the gray-scale histogram of the entire image. Pixels below the threshold are allocated a value of zero and labeled as non-feature pixels (background), while those above it are assigned a value of one and labeled as feature pixels (foreground; this corresponds to the white islands in Figure 5.2c). In the presence of many objects with low gray-scale contrast, the histograms do not show distinctive modes necessarily, leaving ambiguities in the selection of appropriate thresholds. To prevent uncertainties, the Otsu method [149] is used for automated thresholding. Otsu's method automatically determines the optimal threshold by maximizing the variance between the foreground and background pixel intensities. To further improve accuracy, the binarization is applied on small clusters of size 12 m $\times$ 12 m, each containing approximately 20 floes. The smaller size of the clusters produces more segregated modes in the grey-scale histogram, enhancing the effectiveness of automated thresholding [61].

A distance transformation [150] is then applied to the binary image to assign each feature pixel a value corresponding to its distance from the nearest non-feature pixel [151]. The local maxima within this matrix, defined as pixels with values greater than or equal to those of their neighbors, identify seeds that pinpoint individual objects [cf. 16]. Similarly to the clustering of binarisation, regional local maxima from sub-regions of the whole image were considered to enhance accuracy. If the portion of image within a sub-region is sharp, objects are well separated and possess only one seed. Therefore, their segmentation automatically follows from the binarisation. This initial phase of floe detection is reported in Figure 5.2d,g, which show seeds and the concurrent segmented objects respectively.

For the majority of sub-regions, however, adjacent objects were merged through the process and thus could not be segmented by binarisation alone. This resulted in large and irregular (white) islands pinpointed by more than one seed (see Figure 5.2c). For these cases, the segmentation is achieved through a second phase, which relies on a gradient vector flow (GVF) Snake algorithm [152]. This consists of an active contours (snakes) model [153], which evolves initial curves within an object towards its boundaries until it matches the perimeter. Compared to traditional active contour methods, the GVF Snake algorithm is less dependent on the initial contour and, thus, can process objects with complex shapes more efficiently, even in noisy and low contrast images. The accuracy depends on the initial contour being positioned as close to the true boundary as possible, noting the initial shape does not prevent the final contour from aligning with more irregular boundaries (an example of the evolution of an initial contour is presented in the inset of Figure 5.1). As most of the objects are connected to each other through only a few pixels, they can be isolated by smoothing the edges with a morphological erosion process [154]. These newly emerging objects are initialised by ellipses, which represent a natural shape for ice floes [cf. 1, 34]. The initial contour is selected so that the second moment of the covariance matrix matches the one of object [129]; see Figure 5.2e. The unprocessed objects remain within conglomerates of white regions as they share a significant portion of the edge with their neighbors, which cannot be consumed with morphological erosion. Segmentation is achieved by applying circles as initial contours to seeds, noting that the circular shape is an alternative to ellipses for approximating ice floes of small dimensions [34]. Relying on the distance transform, the radius is selected such that the contour is within the object, but not too far from the presumed edge (Figure 5.2f). Once initial contours are assigned to all seeds, the GVF snake algorithm is applied to expand the contours and, hence, identify the object's boundaries (Figure 5.2h-i). The algorithm requires approximately 30 seconds per floe to complete the segmentation.

The GVF approach is not free from anomalies and inaccuracies, which can result in features that are not present in the original image. Coefficients of circularity and eccentricity are used to quantify how closely the various shape resembles a perfect circle or how much elongated the feature is [see 155, 156]. Through the imposition of high-valued thresholds, spurious features in the form of nearly-perfect circular shapes or line segments are eliminated. Furthermore, objects without closed boundaries at the image's edges are also disregarded.

The final output of the analysis combines results from the various phases and is reported in Figure 5.2j. From this binary mask, geometric properties such as area, perimeter, and diameter are extracted by identifying connected pixel regions corresponding to each floe. Area is calculated from the number of pixels in each region, while perimeter and diameter are determined using boundary tracing techniques [157], which follow the edges of each floe to measure their outlines and maximum span.

5.4 GVF snake algorithm versus benchmark segmentation

The GVF snake algorithm is applied to the benchmark images presented in Chapter 4, and the outcomes are visually compared with those from manual segmentation (refer to Section 4.5). Figure 5.3 displays the segmentation of ice floes as contours superimposed on the original images, which represent different levels of sea ice clarity and lighting conditions.

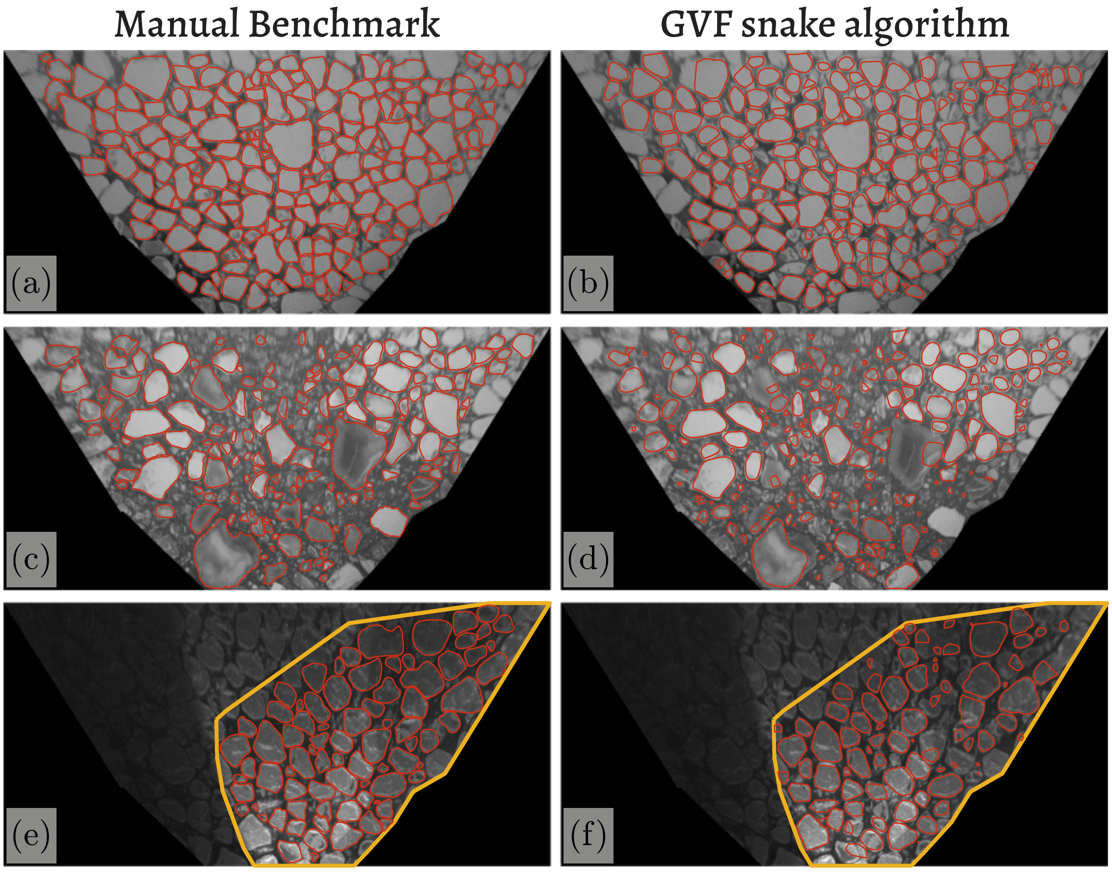

FIGURE 5.3: Contours of ice floes identified through benchmark manual segmentation under clear conditions (a), in a complex environment (c), and at nighttime with the ship's spotlight-lit area highlighted in yellow (e). Corresponding contours detected using the GVF snake algorithm are shown in images (b, d, f).

In comparing the snake-based method (Figure 5.3b,d,f) with manual segmentation (Figure 5.3a,c,e), notable variations in detection precision emerge, primarily due to the contrast and heterogeneity of the ice's appearance. Under optimal ice conditions (see Figure 5.3b), the snake model segments floes with high accuracy, though it misses some. When initial contours are set within irregular floes or those with heterogeneous gradients, curve evolutions can converge to incorrect segmentations. These are filtered out based on the coefficients discussed in Section 5.3, resulting in fewer identified floes.

Under less than optimal ice conditions (see Figure 5.3d), inaccuracies rise considerably. Contours often converge on smaller and less accurate segmentations, particularly with floes displaying varied gradient levels. This generally leads to boundaries that are smaller than the true floe edges, causing an over-representation of smaller floes compared to the manual segmentation, which then affects further quantitative ice floe analysis.

As outlined in Section 5.2, nighttime image analysis is limited to areas illuminated by the vessel's spotlight. This approach allows for the examination of images that would otherwise have been unusable due to the prevailing darkness across most of the image. The nighttime application of the GVF snake algorithm (see Figure 5.3f) presents both strengths and issues of the aforementioned conditions. Floes close to the ship's light source are accurately identified, benefiting from a consistent gradient. Conversely, floes farther away are segmented with lower reliability due to increased darkness and blurriness.

Section 7.4.1 provides a detailed understanding of the snake-based method's performance, featuring a more objective analysis that includes statistical evaluation of the results and comparison with manual benchmarks.

5.5 Conclusions

The effectiveness of a snake-based method in segmenting ice floes is evaluated using a subset of images detailed in Section 4.5. An automated initial contour generator is developed to closely mimic the shape of ice floes, thereby reducing the generally high computational time of the model. The outcomes from the application of the GVF snake algorithm are then compared with those obtained through the manual segmentation. Both pre-processing and post-processing are essential to improve image clarity and remove incorrect segmentations that do not match any ice floes in the original images.

The GVF snake algorithm has proven to be an effective technique for capturing the boundaries of ice floes, even in densely packed scenarios. Incorporating an automatic initial contour generator allows for the method's generalization, making it autonomously applicable to a multitude of ice images under various conditions. However, the model is computationally intense and its success heavily depends on the initial contour inputs. When these contours are not sufficiently close to the final floe boundaries, segmentation becomes less accurate. As a result, this method successfully identifies approximately 80% of the floes in the image, leaving the rest unsegmented. For these reasons, the snake-based method is not considered reliable for analyzing parameters such as ice concentration, and its use for this type of analysis is discouraged. Despite these limitations, where floes are detected, they are segmented with significant reliability. This precision makes it suitable for floe size analysis, particularly beneficial in large datasets where the effects of minor inaccuracies, such as contours slightly smaller than the true floe boundaries, are mitigated. An extensive statistical analysis of these findings is detailed in Section 7.4.1.

Chapter 6

Vision Foundation Model

6.1 Redefining Image Segmentation with AI

The main limitation of the snake-based method (Chapter 5) is its high sensitivity to initial contour placement, which directly depends on the image's clarity. When the ice floes feature a heterogeneous ice gradient or share a significant portion of their edges with neighboring floes, the automatic initial contour generation does not succeed in producing contours that are sufficiently close to the true floe boundary, causing a reduction of the segmentation efficiency.

Image segmentation techniques have experienced profound transformations due to recent advancements in AI. Contrary to the traditional snake-based models, modern techniques use AI systems to interpret images through general patterns learned from a training dataset, instead of relying on the specific features at a pixel level, such as smoothness, roughness, and contrast, unique to the individual image. Among AI-based technology, vision foundation models [158] represent an alternative approach to image segmentation that eliminates the need for manual feature engineering through the application of deep learning techniques. By processing the entire image without dependency on initial contours, these methods not only eliminate the necessity of a priori knowledge of the object's shape but also significantly reduce the computational time.

Vision foundation models are trained on a massive amount of varied data that can be adapted to a wide range of tasks and operations, and so serving as general-purpose systems. Although the training requires more time and computer resources than other deep learning models [such as convolutional neural networks; 159], the applicability of foundation models across diverse contexts reduces the need for multiple domain-specific models.

Segment Anything Model (SAM) by Meta AI Research [57] emerges as the first vision foundation model capable (in principle) of segmenting any object within an image. It is the product of training on an unprecedented segmentation dataset, comprising 1 billion masks across 11 million images. SAM introduces promptable segmentation to highlight specific objects in an image based on user commands, without labelling them, unlike traditional DL methods that assign a featured class to every pixel. Mimicking the human eye in delineating object borders without prior knowledge, SAM achieves zero-shot learning, which is the ability to process objects that are not observed during training without additional labeled data. However, its efficacy in real-world applications remains to be fully tested. Studies have highlighted its challenges in accurately identifying small densely packed or transparent objects [160]. While achieving comparable accuracy to specialized and highly trained models, SAM's performance drops when processing images with weak ice gradients or non-uniform ice distributions [58].

Advancing vision foundation models to adapt to various and complex segmentation tasks becomes crucial [161], especially in polar regions where new, relevant training data is scarce and challenging to obtain. In the following sections, SAM is introduced and applied to the same subset of images processed by the snake-based method. The methodology for using the model and obtaining segmentation masks is detailed. The outcomes are then compared with the manual benchmark segmentation and suitability for applications in polar regions is discussed.

6.2 Segment Anything Model

Segment Anything Model (SAM) is built upon the popular deep learning framework, PyTorch [162], and offers two distinct modalities to segment images: an automatic mask generator and a prompt-based mode. The first modality is designed to independently segment every recognizable element within an image without any need for instructions or input from the user. With this mode, SAM autonomously determines which parts of the image to segment, based on its built-in parameters. In contrast, the prompt-based mode allows users to guide the segmentation process by marking regions of interest with points or drawing bounding boxes around them. This can be as specific as a single object in a crowded scene or a particular portion of a landscape. This modality is particularly useful when precision and control over the segmented areas are crucial.

The performance of SAM for detecting sea ice floes is explored herein using both automatic and prompt modes. As for the snake-based algorithm, the sea ice images are enhanced as described in Section 5.2 before being processed by the SAM. This increases the overall quality of the output as the enhancement already addresses some common challenges like the differences in lighting and weather conditions in the image database. It is worth mentioning that the model is initialized on a consumer CPU. For faster deployment, application on an HPC computer is recommended.

6.2.1 Automatic mask generator

With the automatic mask generator mode SAM selects a fixed sample of points in a grid over the image (see Figure 6.1a). For each of these points, it can generate one or multiple masks assigning a value of one to the feature pixels corresponding to the identified objects and a value of zero to the non-feature pixels representing the background. Then, the model autonomously eliminates the redundant masks and filters them for quality. The output returned is a list of filtered masks corresponding to all the elements in the image (see Figure 6.1b). For sea ice images, this list includes masks containing ice floes, interstitial ice, and open water regions.

As with the snake-based models, SAM requires post-processing to eliminate anomalies, inaccuracies, and objects with open boundaries at the image's edge (cf. Section 5.3). However, this process alone does not discard all the masks with water regions (a feature that is not the target of the sea ice analysis), for which the coefficient of convexity [163] is exploited as a filtering criterion. In general, the less irregular an object's boundary, the higher its convexity will be. Ice floes, being approximated by ellipses and circles, exhibit convexity values tending to 1. Consequently, the more irregular, complementary water regions display lower convexity values. By setting a high threshold for this coefficient, these irrelevant regions are therefore filtered out (cf. [164]).

A closer examination of the output list reveals that certain masks redundantly represent the same ice floes, indicating that the deduplication of the masks applied by the model is not optimal. This issue primarily occurs with adjacent or overlapping floes that have poorly defined boundaries. In these scenarios, the model tends to generate identical masks for the floes multiple times, compromising the output list's suitability for direct quantitative ice floe analysis (see first two layers in Figure 6.1b). To address this challenge, all masks from the list are consolidated into a single comprehensive mask (cf. [58]). Consequently, masks corresponding to the same floe are merged. This final mask displays a feature pixel if any of the original masks also marked that pixel as positive (see Figure 6.1c).

Perimeters and properties of the ice floes segmented by SAM are finally extracted from the comprehensive mask using boundary tracing techniques. The runtime of this SAM mode is approximately 3 minutes per image.

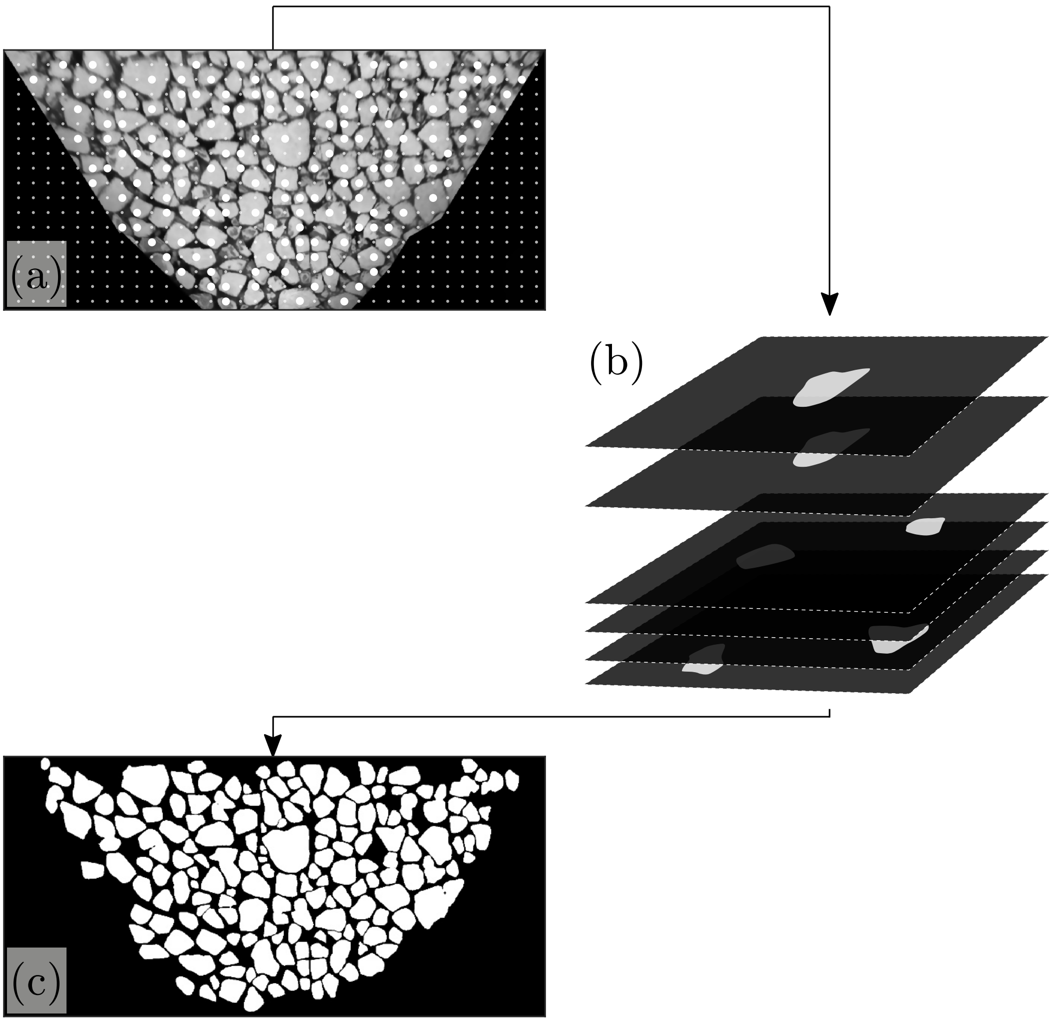

FIGURE 6.1: SAM's automatic mask generator algorithm: (a) fixed points selected by SAM over the grid in the enhanced sea ice image; (b) consolidation of the list of filtered masks returned by the model; (c) final unified mask with all the detected ice floes.

6.2.2 Prompt-based

In the prompt-based modality, the prompts necessary to initialize the model must be specified by the user. These prompts can take the form of points, bounding boxes, or a combination of them. Points may be single or multiple and are used to either directly indicate the desired object or to delineate both the object and areas to be excluded from identification. This modality does not incorporate any quality filtering, leaving the output's quality dependent on the chosen prompts.

For sea ice images, seeds derived from the distance transform matrix (see description in Section 5.3 and Figure 5.2c) are found to be effective at pinpointing individual ice floes (cf. Fig. 6.1a and Fig. 6.2a). Each seed is then utilized as a single prompt, which is fed into the model to generate the mask for the specific ice floe (Figure 6.2a). The resultant output is a list of masks of dimension n, where n corresponds to the number

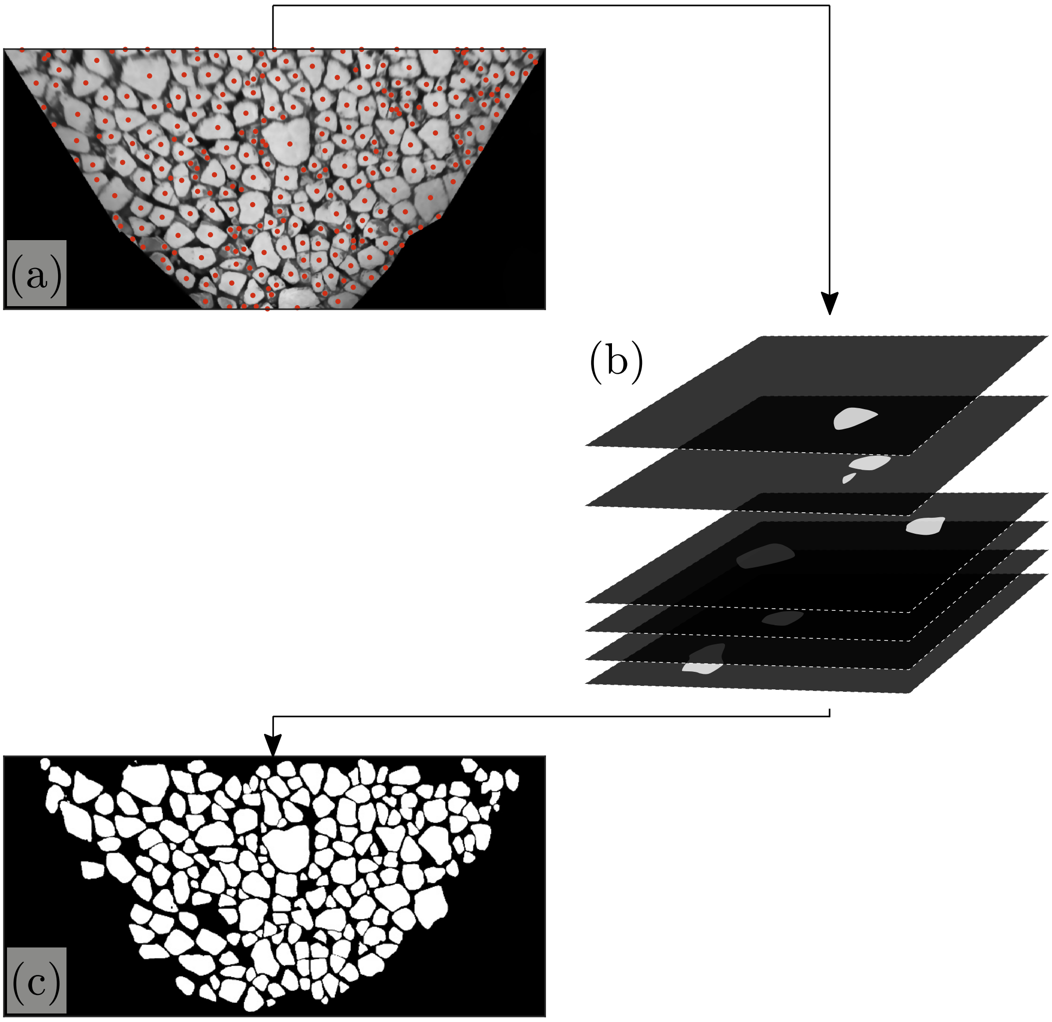

FIGURE 6.2: SAM's prompt-based algorithm: (a) seeds in red of the ice floes in the enhanced sea ice image; (b) consolidation of the list of filtered masks returned by the model; (c) final unified mask with all the detected ice floes.

of seeds in the image. However, introducing a seed to identify a floe in an area of the image characterized by uncertainty often results in an inaccurate mask. Instead of isolating the single floe, this mask may erroneously include discontinuous water regions or parts of adjacent floes (see first two layers in Figure 6.2b). The application of the shape-based filters – measuring circularity, eccentricity, and convexity – filters out the clusters of feature pixels in the mask that do not match the typical shape of ice floes. While clusters representing portions of the floes, rather than the floes in their entirety, are corrected with the appropriate masks for those same floes by consolidating all the output list into a single unified mask (Figure 6.2c). From this final binary mask, all properties of each individual ice floe can be easily extracted.

SAM is up to 5 times faster with seeds entered as prompts and produces more masks on average than the automatic mode. By bypassing the model's internal point selection process, the segmentation becomes more efficient. The higher number of masks produced is due to the limitations of the automatic mode, whose internally selected points are fixed and often insufficient to cover the multitude of ice floes present in the image.

6.3 SAM versus benchmark segmentation

The two SAM modalities are applied to the benchmark images introduced in Chapter 4 and the results are visually compared against those obtained through the manual segmentation (refer to Section 4.5). Figure 6.3 and Figure 6.4 show the ice floes segmentation as contours superimposed on the three original images, each representing a different ice or illumination condition.

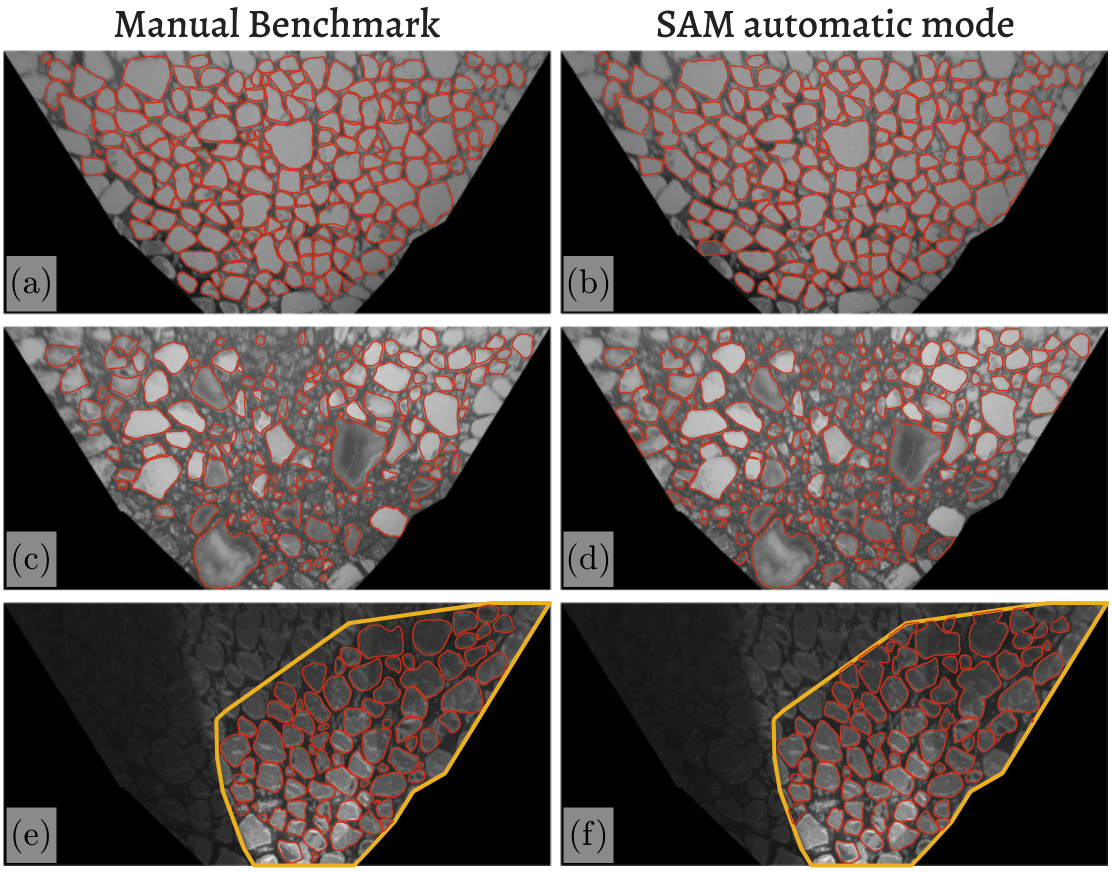

FIGURE 6.3: Contours of ice floes identified through benchmark manual segmentation under clear conditions (a), in a complex environment (c), and at nighttime with the ship's spotlight-lit area highlighted in yellow (e). Corresponding contours detected using SAM in automatic mask generator mode are shown in images (b, d, f).

The number of ice floes identified using the automatic SAM mode is lower than the corresponding benchmark value for all the sample images (see Figure 6.3). This discrepancy is mainly due to the mask unification process aimed at eliminating the output redundancy, described in Section 6.2.1.

Adjacent floes correctly segmented as separate entities may also be represented by a single, larger mask showing them as one connected, irregular floe. In the mask consolidation process, this larger, inaccurate mask overwrites the correct, smaller ones due to its size. This leads to an over-representation of larger floes that impacts the accuracy of floe size distribution analysis. Further, the segmentation of the floes becomes less reliable at the image's edge as the model tends to produce masks with closed-boundary objects even for the floes extending beyond the borders, which cannot be automatically filtered out. This occurs predominantly in the complex ice scenarios (Figure 6.3d) and nighttime images (Figure 6.3f).

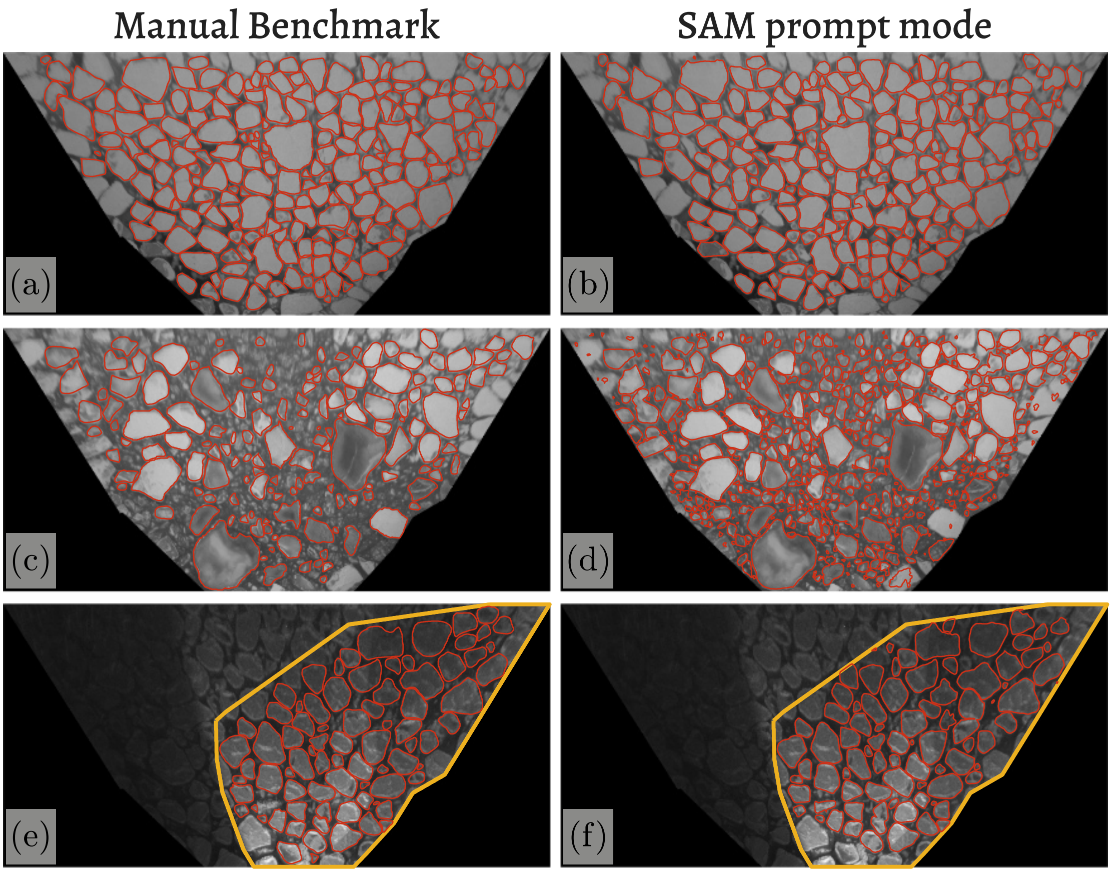

FIGURE 6.4: Contours of ice floes identified through benchmark manual segmentation under clear conditions (a), in a complex environment (c), and at nighttime with the ship's spotlight-lit area highlighted in yellow (e). Corresponding contours detected using SAM in prompt-based mode are shown in images (b, d, f).

The contours of the ice floes obtained with the prompt-based mode are shown in Figure 6.4. Imposing the seeds as prompt leads to the detection of almost the totality of the floes in all the conditions examined. Most of the adjacent floes that the automatic mode identified as a single unit are completely separated by this second approach, with the remaining part connected only through a few pixels. When the edge between two adjacent floes is particularly blurred, without a clear discontinuity, the model finds it difficult to assign that portion of the edge to just one of the two floes. If the portion is assigned to both the floe masks, these end up being merged by the mask unification process. While this leads to a lower overall count of detected floes under all conditions, there's a specific behavior in more complex ice scenarios that can artificially inflate their number. Specifically, in images where ice floes exhibit a heterogeneous ice gradient and have low contrast against water, the model is prone to hallucinate, i.e. to generate false contours that do not correspond to any actual object in the image. These anomalies, resembling ice floes in shape but lacking real counterparts, are neither corrected by merging with the actual floe masks nor eliminated by the shape-based filtering coefficients discussed in Section 6.2.2.

6.4 Conclusions

The performance of SAM in segmenting ice floes is evaluated across both its automatic mask generator and prompt-based modality. The two modalities are tested on the same subset of images also processed by the snake-based method and the results are compared against those obtained through the manual segmentation. The subset contains images obtained under optimal or complex ice scenarios (low ice gradient homogeneity), acquired at daytime or nighttime. As for the snake-based algorithm, post-processing is necessary to refine the segmentation as the output list of masks from both the SAM modalities includes redundant masks or masks that do not correspond to ice floes. Nonetheless, when compared to the snake-based method, this model succeeds in covering with its segmentation a broader ice surface in a considerably shorter time frame.

Besides a majority of correctly identified ice floes, the principal difficulties are encountered in segmenting adjacent floes as separate entities, especially in images characterized by an inhomogeneous ice gradient and weak edges between floes. In such scenarios, SAM's prompt-based mode outperforms the automatic mask generator modality by correctly separating a greater number of floes. Therefore, SAM's automatic mode is effective for calculating ice concentration, successfully identifying larger floes despite challenges in their boundary segmentation, while the prompt-based mode offers versatility for both ice concentration and floe size analysis. Caution is needed when the dataset primarily consists of images featuring complex ice scenarios, as these conditions can cause the prompt-based mode to produce misleading segmentations. A detailed statistical analysis in Section 7.4.1 explores the advantages and limitations of each mode, providing comprehensive insights into their application efficiency.

The main drawback of the prompt-based mode is the occurrence of hallucinations, which are incorrect segmentation masks that become more frequent in images with low ice-water contrast. These hallucinations represent a trade-off when aiming to generalize the method across various sea ice images. Ideally, such inaccuracies could be avoided by focusing the model's attention on parts of the images with higher contrast. However, this approach would necessitate manual intervention, thereby undermining the objective of automating the sea ice segmentation process. On the other hand, as the SAM's prompt-based mode segments are based solely on seeds without insight into the ideal shapes of the floes, the segmentation of adjacent floes can be automatically improved by incorporating knowledge of the optimal ice floe shapes into the model. This can be achieved by adding a layer into SAM where floes that are not correctly separated are further processed by the snake-based algorithm whose initial contours summarize the shape information. By integrating specific shape characteristics into the model, this approach combines the strengths of both methods, refining segmentation results without sacrificing process automation.

Chapter 7

A Combination of SAM and GVF algorithms

7.1 Introduction

Snake-based models excel in delineating detected floes with reliability and accuracy. Despite this, their sole reliance on visual characteristics and lack of data learning capabilities cause them to struggle in complex scenarios, such as ice floes with varied gradients. In contrast, foundation models are adept at pattern recognition, benefiting from training on extensive and diverse datasets. However, they cannot include efficiently specific shape details of floes in their segmentation processes, resulting in inaccuracies particularly when distinguishing adjacent floes with weak edges. To overcome the inherent limitations of each approach, when applied independently, an integration of SAM and GVF snake models is proposed.

The combination of SAM and active contours offers a comprehensive solution for ice floe segmentation. By incorporating the GVF model as a refinement step, the process is enriched with floe shape information, compensating SAM's shape awareness limitations. This approach not only leverages SAM's global learning and recognition strengths to manage diverse and complex image data but also improves detection accuracy through the GVF algorithm's shape-informed segmentation. A similar strategy of merging geometrical information with the concept of region similarity originating from shape-agnostic deep learning models has been efficiently utilized in fields beyond sea ice analysis [165, 166], achieving remarkable success in medical imaging where precision in object delineation is critical. This application emphasizes the nature of foundation models, designed to be versatile tools adaptable to meet the exacting needs of tasks requiring a higher level of accuracy.

Section 7.2 detail the integration of the GVF algorithm into the SAM's prompt-based mode, culminating in the SAM-GVF hybrid algorithm. This combined approach is applied to the same subset of images also processed by the other segmentation techniques for direct comparison with the manual benchmark.

Subsequently, Section 7.4 discusses an application of image segmentation with a focus on the estimate of floe size statistics. A small subset of images is used to assess the performance of the various segmentation methods within a more robust statistical framework (Section 7.4.1). Variations in floe size statistics arising from GVF, SAM, and combined SAM-GVF are discussed. The best performing method is then applied to the entire databases (Section 7.4.2) – comprising winter expeditions to the Antarctic MIZ in 2017, 2019, and 2022 (e.g. [11, 24]). Parameters such as floe area, diameter, and ice concentration are determined for each sea ice image through the segmentation and statistical properties are analysed.

7.2 SAM and GVF combined algorithm

The combination of SAM and GVF involves an initial broad identification of ice floes across the entire image using SAM, followed by precise, shape-specific refinements using GVF. The steps for the segmentation with this hybrid approach are displayed in Figure 7.1. The process starts with the application of SAM's prompt-based mode to the enhanced sea ice images, as discussed in Section 6.2.2. Seeds derived from the distance transform matrix (see description in Section 5.3 and Figure 5.2c) are used to initialise the model. Each seed effectively pinpoints an ice floe, enabling SAM to generate a mask for that specific floe, resulting in a collection of masks equal to the number of seeds in the image. While this modality efficiently isolates floes under various conditions, it sometimes produces inaccurate masks due to uncertainty in certain image areas. To address these uncertainties, the individual masks are consolidated into a unified mask, which results in a binary image (Figure 7.1b). This consolidation corrects segmentation by eliminating uncertain masks and retaining those unequivocally associated to floes. Nevertheless, although most ice floes are successfully detected and separated, challenges arise with blurred edges between floes that lack clear discontinuity. The model struggles to assign these ambiguous edge portions exclusively to one floe. During the mask unification process, this ambiguity causes such floes to be welded together at their most unclear edges, underscoring the need for further refinement in distinguishing closely adjacent floes.

The refinement of SAM segmentation is achieved through a subsequent phase that utilizes the GVF model (Figure 7.1c-e). As previously discussed, snake algorithms are

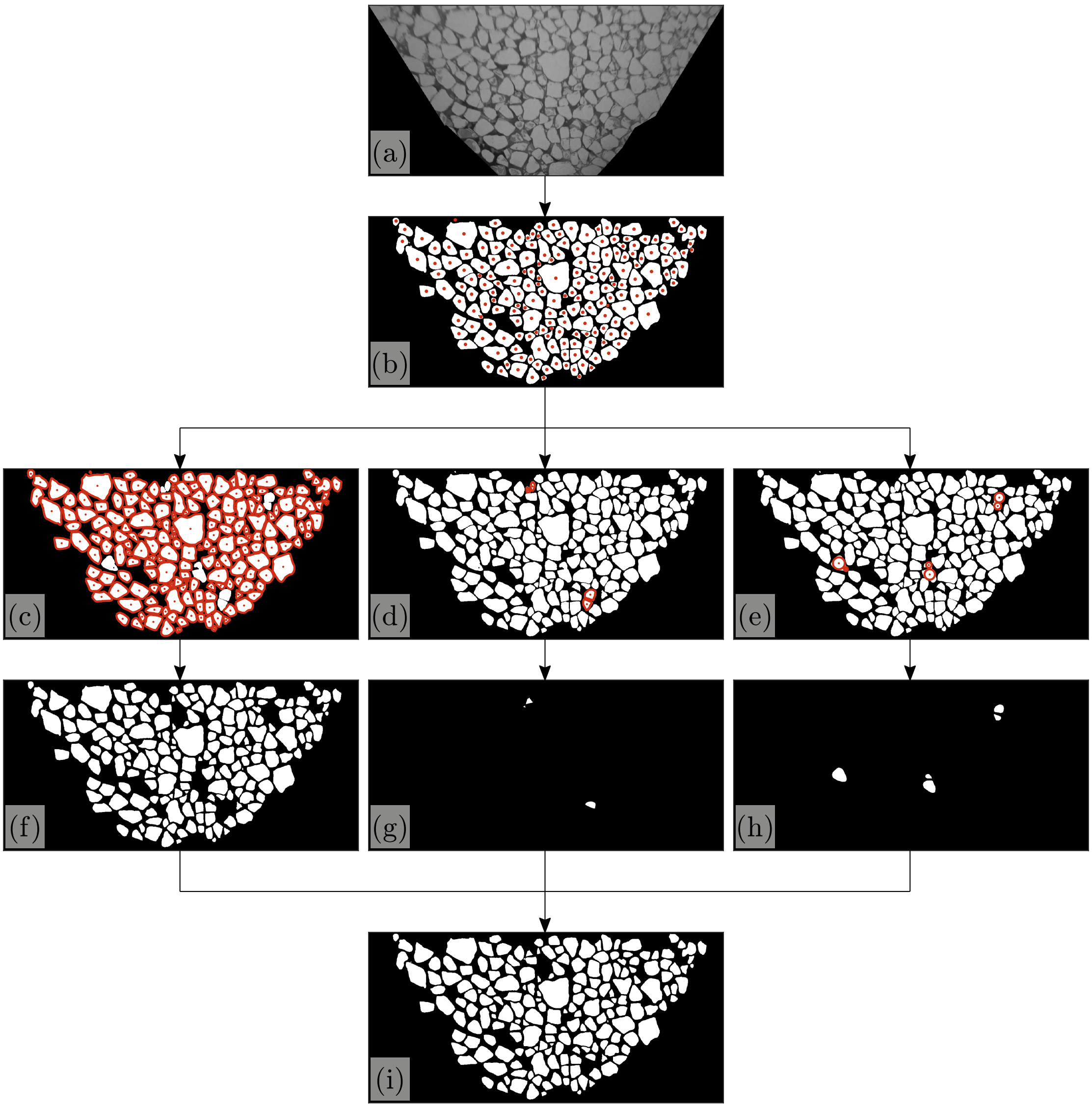

Figure 7.1: SAM-GVF hybrid algorithm: (a) original image (b) unified binary mask produced by SAM's prompt mode with seeds in red of the ice floes; (c) contour in red of the floes containing a single seed because already correctly segmented by SAM; (d) initial contour in red of the floes containing a single seed after a morphological erosion; (e) circular initial contour in red for each remaining and unused seed; (f) ice floes already identified in Figure 7.1c; (g) ice floes detected by the GVF snake algorithm initialized with the initial contours in Figure 7.1d; (h) ice floes detected by the GVF snake algorithm initialized with the circular contours; (i) final binary image with all the detected ice floes.

particularly adept at separating ice floes in dense scenarios by leveraging the shape information provided by initial contours. In this process, seeds are employed to generate these initial contours. A distance transformation is then applied to the binary comprehensive mask shown in Figure 7.1b. This transformation calculates the distances from each feature pixel, which corresponds to ice, to the nearest non-feature pixel, which represents the background. Similarly to the snake-based method, the local maxima of this distance matrix serve to identify the seeds that pinpoint individual ice floes. However, in this hybrid approach, the binary image used for finding seeds comes from a unified mask derived from the image segmentation through SAM, whereas in the standalone snake-based method, it is generated through automated thresholding (detailed in Section 5.3). As a result, the majority of floes are already detected accurately and require no further processing. These pre-detected floes are represented by the objects possessing only one seed in Figure 7.1c. Excluding these floes (Figure 7.1f) from the GVF processing reduces computational time and focuses the initial contour placement only on those floes that SAM did not segment correctly. These result in objects pinpointed by more than one seed in Figure 7.1d,e.

Part of the interconnected objects are merged with each other by only a few pixels and, hence, they can be isolated through morphological erosion, which smooths the edges. The contours of the newly emerged objects serve as the initial contours for the snake model (see Figure 7.1d). These objects represent the ice floes that SAM partially segments, capturing their shapes successfully but not completely separating them. Therefore, utilizing their contours retains the shape characteristics of the floes, enabling the snake model to accurately expand the contours to the true boundaries of each floe.

The remaining unprocessed objects, which share a significant portion of their edges with neighboring objects, cannot be effectively isolated through morphological erosion. For these cases, the binary image lacks detailed information about the floe shapes. Therefore, segmentation is facilitated by applying circles as initial contours around the seeds, a shape commonly used to approximate ice floes in the marginal ice zone. The radius for each circle is chosen based on the distance transform to ensure the initial contour lies within the object but remains close to the presumed edge (Figure 7.1e). Once initial contours are established for all seeds, the GVF snake algorithm is applied to expand these contours, thereby delineating the object's boundaries (Figure 7.1g-h).

The advantage of applying the GVF snake algorithm is its ability to capture the shape of ice floes in densely packed environments where SAM struggles to define boundaries. However, even the combined SAM and GVF approach may introduce anomalies and inaccuracies not present in the original image. As with the standalone GVF application, spurious features such as nearly-perfect circles or elongated line segments are removed using circularity and eccentricity coefficients (refer to Section 5.3 for details). The final output, combining results from all phases, is presented in Figure 7.1i, from which floe properties are extracted using boundary tracing algorithms.

7.3 Validation against benchmark

The combined SAM-GVF algorithm is applied to the benchmark images detailed in Chapter 4, with the results visually compared against those obtained through manual segmentation (refer to Section 4.5). Figure 7.2 illustrates the segmentation of ice floes, showing contours superimposed on the original images that depict various levels of sea ice clarity.

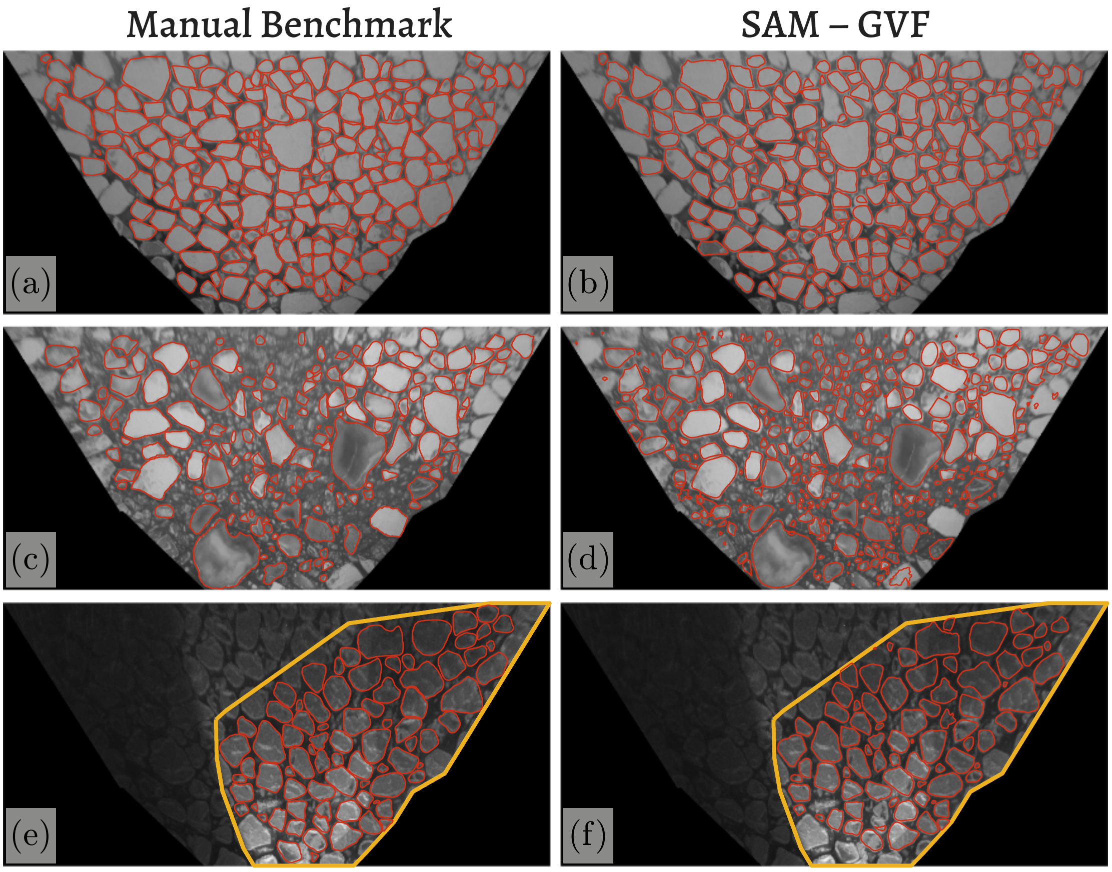

Figure 7.2: Contours of ice floes identified through benchmark manual segmentation under clear conditions (a), in a complex environment (c), and at nighttime with the ship's spotlight-lit area highlighted in yellow (e). Corresponding contours detected using SAM combined with the GVF snake algorithm are shown in images (b, d, f).

In this hybrid approach, the large number of floes correctly identified by SAM is augmented by those separated by the snake algorithm, achieving nearly complete identification of floes regardless of the ice image's clarity. The GVF algorithm enhances SAM's segmentation by separating adjacent floes with unclear boundaries, thereby increasing the amount of accurately identified floes. However, some uncertainties still persist. Specifically, these are hallucinations – false contours that do not correspond to actual floes, primarily occurring in complex scenarios with varying ice gradients and low contrast against water – arising from the SAM-based segmentation counterpart. Moreover, when the adjacent floes with blurred edges have particularly irregular shapes, initial contours for the GVF step may not accurately conform to the floes' actual shapes, leading to incorrect results. However, this issue affects a minority of floes only, and the errors are typically filtered out using the coefficients of circularity and eccentricity described in Section 7.2. The advantage of the snake phase is that it either produces correct contours or incorrect ones that can be effectively identified and removed by these coefficients. Since only a small number of floes are affected and subsequently removed from the final segmentation, floe size analysis remains unaffected, though ice concentration might be slightly underestimated compared to the benchmark. An extensive statistical analysis of these results will be detailed in Section 7.4.1.

7.4 A practical application: Floe size statistics

In this section, the performance of various segmentation methods is evaluated by analyzing floe size statistics. These statistics are derived by applying the methods to a small subset of 10 random images, which includes a broad range of image quality. Discrepancies in floe size statistics resulting from the GVF, SAM, and combined SAM-GVF methods are examined and discussed against benchmark statistics derived from a manual segmentation approach. The most effective method is then applied to the whole database, which comprises imagery from the three winter expeditions to the Antarctic Marginal Ice Zone (MIZ) in 2017, 2019, and 2022. This further application aims to identify any statistical deviations that may correlate with the different sea ice conditions encountered during these expeditions (which took place over the same season – winter).

7.4.1 Comparison of floe size distributions from GVF, SAM and SAM-GVF combined algorithms

A carefully selected subset of 10 images, which deviate from the ideal scenario of clear ice boundaries and consistent contrast (see examples in Figure 7.3), is used to reflect the complexity of Antarctic sea ice. These images undergo floe detection through the segmentation methods discussed in this dissertation, namely GVF, SAM, and the combined SAM-GVF approach. The results of the segmentation are then used to estimate floe size statistics, including the number of detected floes, floe concentration, and size distribution for each method. These parameters are shown in Figure 7.4 where they are compared to those obtained from manually segmenting the same image subset to provide an objective benchmark. In the upper panels (Figure 7.4a-b), the number of detected floes and the ice concentration are shown in a normalised form so that values are relative to the corresponding parameters obtained from manual segmentation. Each black line segment extending from the circles to the horizontal line shows how far each method's results deviate from the benchmark. The bottom panel (Figure 7.4c) presents a size distribution based on the diameter of the floes, with the left side representing manual segmentation and serving as the benchmark against which the reliability of the segmentation methods is evaluated.

Figure 7.4a shows that the number of accurately detected floes is underestimated by both the GVF and SAM automatic mode, with values of 0.85 and 0.76, respectively, while it is overestimated by the SAM prompt mode, with a value of 1.20. Generally, the error for this statistic does not exceed 25% of the actual number of floes in the image. The underestimation in both the GVF and SAM automatic mode reflects the challenge these methods face in detecting floes in complex scenarios (Figure 7.3). Conversely, the overestimation in the SAM prompt mode is due to the model's tendency to generate hallucinations. The combined GVF-SAM algorithm mitigates both underestimation and overestimation issues, resulting in a more accurate floe count, with only a slight overestimation (1.06) of the actual number of floes.

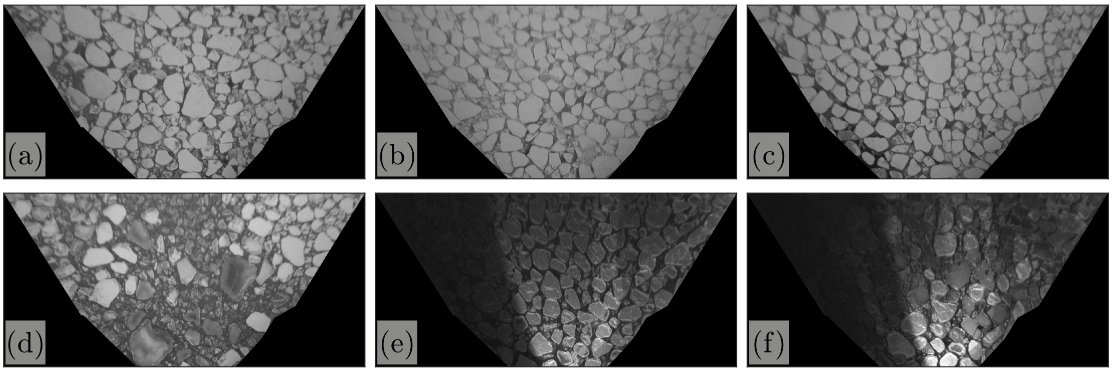

FIGURE 7.3: Sample from the subset of 10 images illustrating the complexity of Antarctic sea ice, used for method comparison.

Sea ice concentration in Figure 7.4b shows that the method based on SAM, regardless of the mode, closely approximates the benchmark from manual segmentation, with values of 0.96 for the automatic mode and 1.01 for the prompt-based mode. Interestingly, despite not excelling at segmenting individual floes – affecting the floe count – SAM effectively distinguishes between ice and water, resulting in the reported high accuracy in separating the sea ice fraction. The combined SAM-GVF method (0.88) introduces slightly more uncertainty, with an error range of about 10%, than SAM alone. However, it still outperforms the GVF method (0.68), which tends to under-detect floes or generate contours smaller than the true boundaries, especially when ice floes display heterogeneous gradients. This limitation causes GVF to underestimate ice concentration, highlighting the benefit of combining it with SAM.

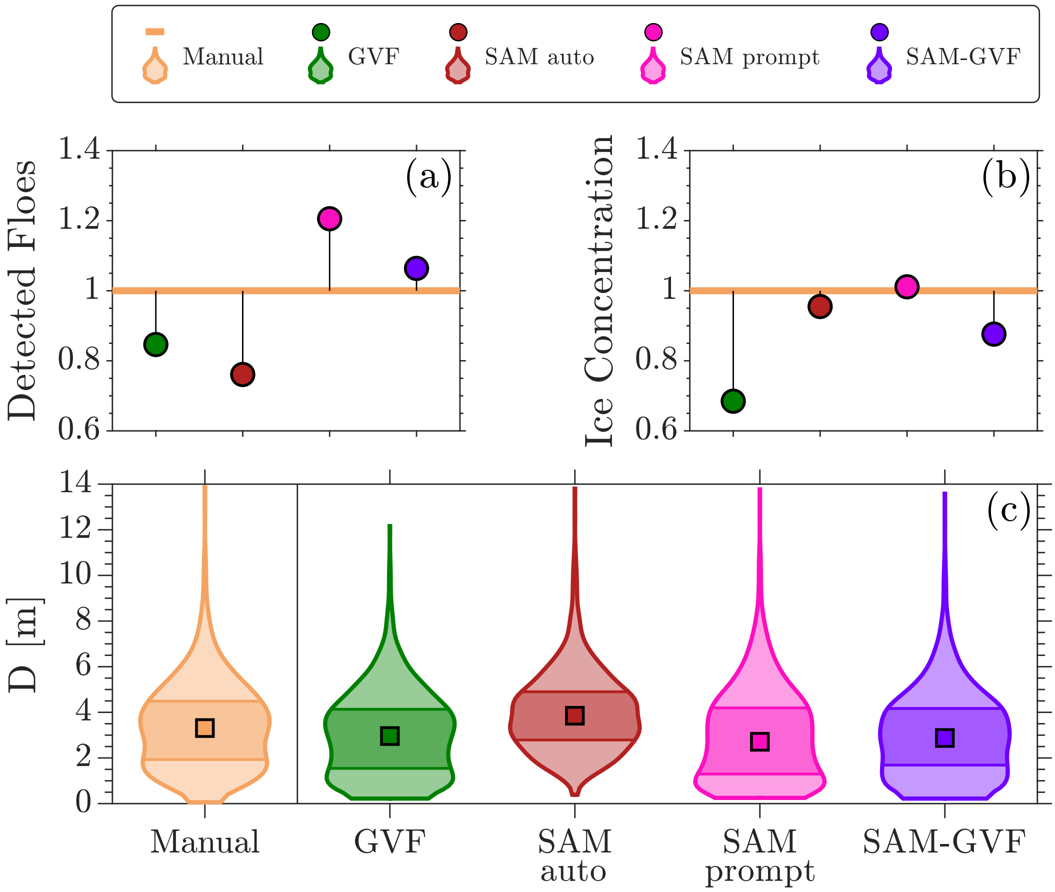

FIGURE 7.4: Comparison of floe size statistics obtained through segmentation with GVF (green), SAM automatic (red) and prompt-based (pink) mode, and the combined SAM-GVF (purple) against the manual benchmark (orange) segmentation: (a) number of detected floes for each method, normalized by the corresponding parameter from manual segmentation (horizontal line); (b) ice concentration for each method, normalized by the corresponding parameter from manual segmentation (horizontal line); (c) floe size distribution illustrated as violin plots for all methods, with the manual size distribution shown on the left. Medians and quartiles are represented respectively by squares inside the violins and darker shaded areas.

The floe size distribution is illustrated as violin plots in Figure 7.4c. These plots combine features of a box plot and a probability density function, showing the median (squares inside the violins), the first (Q1) and third (Q3) quartiles (darker shaded areas), and highlighting potential multimodality in the distribution. In this regard, the benchmark size distribution exhibits an evident bimodality at small (approximately 2 meters in diameter) and larger (around 4 meters) floes, noting that this feature may arise due to the limited size of the sample and, hence, it may both be a characteristic signature of the floe size distribution. Fifty percent of the floe sizes fall between Q1 at 2 meters and Q3 at 4.5 meters, with a median of 3.2 meters. Although there are some minor discrepancies due to biases towards smaller floes, both GVF and SAM-GVF capture the main features of the distribution, such as the median (2.9 meters for both methods) and the bimodality around the distribution's peak, due to their ability to delineate the true edges more accurately than SAM-based approaches. To be noted, though, that the quartiles are underestimated by GVF (1.5 meters for Q1 and 4 meters for Q3), while SAM-GVF provides a more accurate representation (1.7 meters for Q1 and 4.2 meters for Q3) relative to the benchmark. Applications based on SAM alone (in both modes) return a more uncertain distribution. Relative to the benchmark, the prompt-based approach reasonably captures the median (2.7 meters) and quartiles (1.3 meters for Q1 and 4.2 meters for Q3). The bimodality of the distribution is hinted, but there is an evident skewness towards small floe size (around 1 meter) that distorts the shape of the distribution. The standard SAM approach provides the least accurate distribution, with clear uncertainties in the median (3.8 meters), which is overestimated relative to the benchmarks and other approaches, and shape of distribution, which returns a unimodal feature, missing the evident bimodality of the benchmark distribution. Quartiles are also poorly represented (2.8 meters for Q1 and 4.9 meters for Q3), highlighting the limitations of SAM automatic mode in accurately detecting individual floes without seed-based prompts.

Declaring one method as superior to another in absolute terms is not possible, as the choice depends on the specific use case. Prompt-based and automated SAM, with their faster computational speed and strong performance in estimating ice concentration, are better suited for real-time applications where immediacy is critical. In contrast, the hybrid SAM-GVF approach, along with GVF alone, proved more effective at capturing the floe size distribution. In particular, SAM-GVF improves concentration estimates compared to GVF alone, without compromising accuracy in size distribution. However, their longer computational time makes them more suitable for post-processing and further data refinement. It is also important to acknowledge that the manual segmentation of the benchmark dataset inherently involves some subjectivity, arising not only from individual interpretation but also from the ambiguous definition of what constitutes an ice floe. Consequently, how manual segmentation is conducted can affect the entire comparison process. To mitigate this subjectivity and enhance the robustness of the benchmark, increasing the number of images in the dataset is a practical approach.

7.4.2 Floe size distribution based on SAM-GVF combined algorithm

7.4.2.1 General

Herein, the SAM-GVF combined algorithm is applied to the entire imagery database. The camera set up, details of which can be found in Chapter 4, was the same for all the voyages. An overview of the three expeditions and details on the sea ice concentration and floe size are reported in Figure 7.5. All expeditions went through the MIZ and reached regions of sea ice concentration of 100% (a few hundred km into the MIZ). The sea ice was not compact at the southernmost location during the 2017 voyage, though, but it was a mixture of pancakes and solidified frazil ice [34, 69]. Conversely, compact sea ice was reached during the 2019 and 2022 voyages (e.g. [11]). It is also worth noting that cyclones develop primarily in the Atlantic and Pacific sectors and typically follow a south-eastward trajectory, undergoing net cyclogenesis (the development of cyclonic circulation) in the midlatitudes and net cyclolysis (the process by which a cyclone weakens and eventually deteriorates) closer to the Antarctic continent. The South Atlantic, and especially the ice-covered eastern Weddell Sea, is an area of net cyclolysis for systems originating from open ocean (cf. [69]). Waves conditions here are characterised by fully developed seas, i.e. long and gently sloping waves. This is the region where observations were acquired in 2019 and 2022. The voyage in 2017, on the contrary, focused on the Western Indian Ocean sector, which is again a region of cyclogenesis [69]. The sea state observed during this expedition was characterised by relatively young waves with short wavelengths, significant heights, and thus steep forms even in the sea ice region [24, 167].

The purpose of the analysis presented herein is the evaluation of floe size within a robust stochastic framework. Due to the different wave conditions in the two explored sectors, sea ice characteristics differ from each other, despite acquisition occurring during the same season (winter). Hence, the relation of floe size distribution to the specific sea ice conditions is discussed.

7.4.2.2 The expeditions and the imagery database

The routes of the three winter voyages are displayed in Figure 7.5a. The first voyage (hereafter referred to as v1) occurred in July 2017, entering the MIZ in the Western Indian Ocean sector at approximately 61.3°S, 30°E on 04 July 2017 and continuing south to 62.7°S, spending only one day in ice. The second voyage (v2) took place in July-August 2019. The vessel entered the MIZ in the Eastern Weddel Sea at 56.3°S and followed a southward route. It reached consolidate sea ice at 57.1°S and continued until approximately 58°S, staying in ice for three days from 26 July to 29 July. The third voyage (v3) in July-August 2022, followed a similar path. The icebreaker reached the ice at around 58°S, 1°W on 19 July 2002 and traveled southward until it reached consolidated sea ice at latitude 58.8°S, spending six days in the MIZ before heading back North. In total, the three winter expeditions together spent 10 days in sea ice.

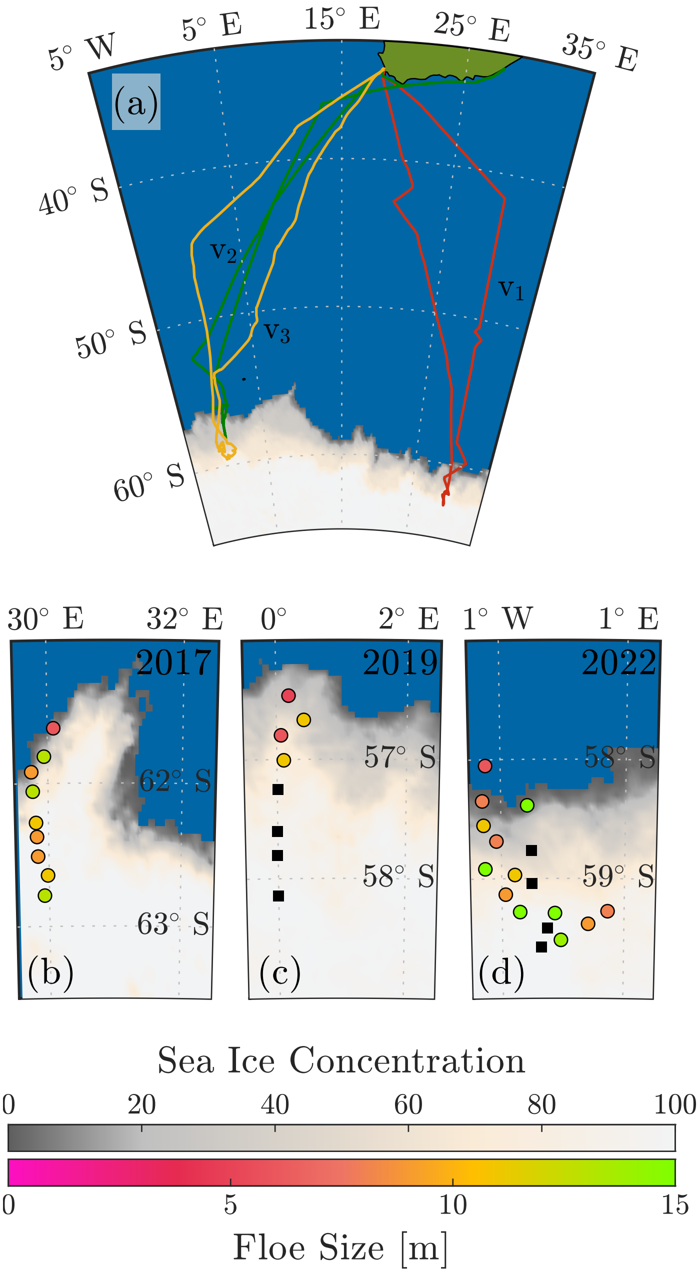

FIGURE 7.5: Antarctic winter expeditions: (a) ship tracks for 2017 (red; v1), 2019 (green; v2), and 2022 (yellow; v3); (b, c, d) maps of the floe size distribution for 2017, 2019, and 2022 ('o': pancake/brash; 'square filled': consolidated ice).

Overall, the combined database includes more than 130,000 images, taken at the sampling frequency of 1 Hz. To ensure independence of data, only one image every 15 seconds is selected for segmentation. Additionally, images taken during stationary periods are excluded. Therefore, approximately 9,000 images are available for analysis: 1,000 in 2017, 2,000 in 2019, and 6,000 in 2022.

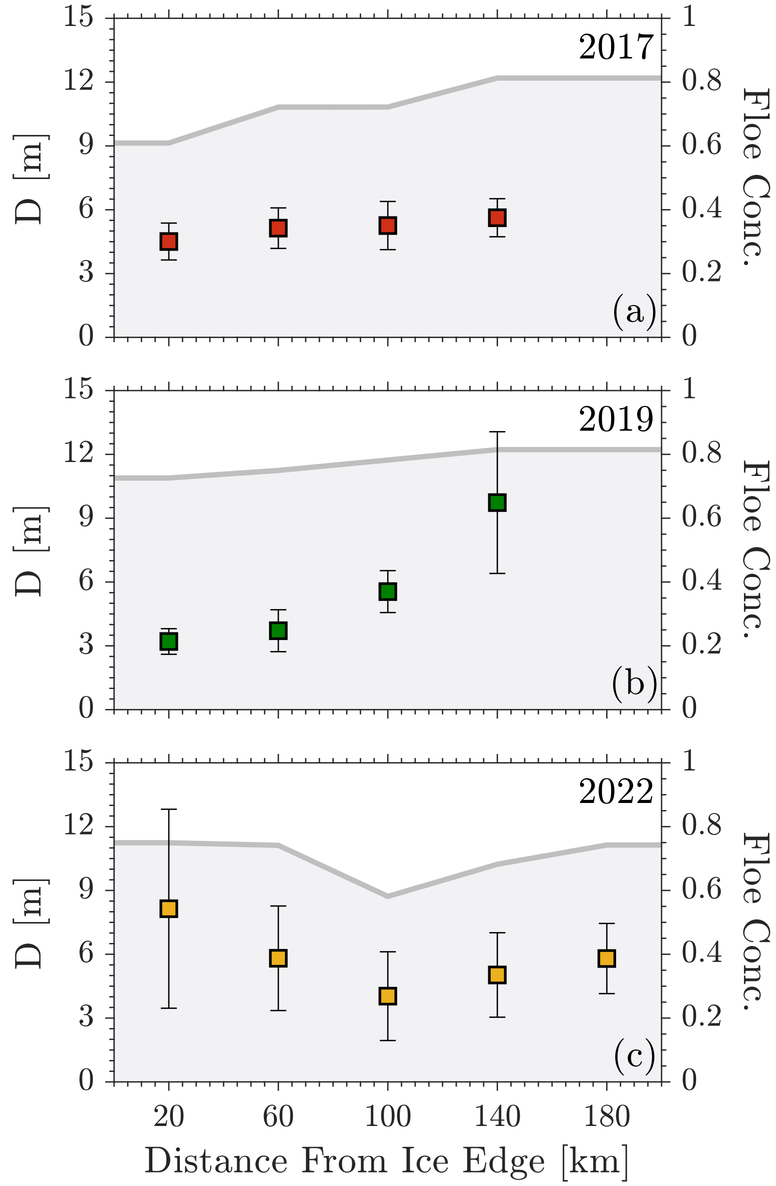

FIGURE 7.6: Average floe size and concentration as a function of the distance from the ice edge (error bar: 1 std).

7.4.2.3 Sea ice concentration and average floe size

A general view of the ice condition along the ship's route, based on the floes size derived from the application of the SAM-GVF algorithm and the concentration resulting from the AMSR2 satellite remote sensing [168], is shown in Figure 7.5b-d. These satellite data, acquired daily at a 6.25 km grid spacing and averaged for the days spent in ice, have limited spatial and temporal resolutions. These limitations, along with susceptibility to atmospheric conditions like cloud cover, introduce significant uncertainties. Consequently, the MIZ edge depicted by satellites differs from that observed directly from sea ice imagery (cf. [34]). In particular, during the second voyage, the ice was encountered further south than indicated by remote sensing, and further north during the third expedition, as detailed in Figure 7.5c-d. The size of the ice floes in Figure 7.5b-c is somewhat proportional to the distance from the ice edge, with dimensions increasing with distance. When floes are no longer distinguishable, the ice is classified as predominantly compact and indicated as black squares in the figure. It is worth noting that there is a significant variability of the sea ice in 2022 (Figure 7.5c). This is partially due to the vessel sailing both southward and eastward, thus exploring a larger sea ice region. Variation of sea ice floe size with distance is less evident with floe size alternating regions of large and small floes along the route.

The variation of floe size with increasing distance from the ice edge is further analyzed in Figure 7.6. Average floe diameters are calculated at 40 km intervals, extending up to the maximum distance of 200 km from the ice edge reached in 2022. Each data point includes also a vertical error bar representing one standard deviation (i.e. 64% confidence interval) associated to the floe size estimate. The average ice concentration, as determined from the images as the ratio of the total area of detected floes to the total area of the image, is also reported. In 2017, the size trend shows a slight increase but remains between 4-5 meters in diameter. The confidence level is relatively stable over distance. The floe concentration is also rather stable as it only slightly increases from 60% to 80%. Interestingly, satellites detect 100% ice concentration over the entire area considered herein (see Figure 7.5a and [34]). The discrepancy is due to the presence of interstitial frazil ice that fills entirely the gaps between floes, enhancing the total sea ice concentration to the maximum. Samples of frazil ice taken during the expedition reveal that the interstitial ice was solidifying. While the weak variability of floe size with distance can be attributed to the limited time spent in the MIZ (one day), it cannot be excluded that the solid frazil ice acted as a constraint on further increase of the floe size, somewhat limiting their dimension. Although the sea ice cover was set to turn into a more compact condition, it remained quite flexible due to intense wave activity with maximum individual wave height reported up to 9 m [24].

In 2019, floe concentration remained steady at 80%, while floe diameters increased from an average of 3 meters within the 0-40 km range to 9 meters between 120-160 km from the ice edge. The variability in size mirrors the increasing trend in diameter, with standard deviations reaching about 3 meters at greater distances. Wave conditions at the time were mild and wave energy penetrated into the MIZ only marginally. Therefore, the pattern suggests a developing growth phase for the sea ice, where floes gradually weld with each other forming larger floes as the distance from the MIZ's edge increases and so does wave action decreases.

In 2022, the six days spent on the ice led to a greater variability in floe sizes. The floe diameters initially decrease from 9 to 4 meters before slightly increasing beyond the 120 km mark. Floe concentration fluctuates similarly, dropping from 75% to 65% and then rising back to 75%. As the vessel moved southward and eastward during this period, it encountered varying ice types, from fully formed floes to conglomerates of floes merged together to broken floes, contributing to the high variability observed (cf. [11]). The standard deviation is consistently greater than 2 meters, reflecting the diverse sizes of floes found across different days in the same sea ice region. This variability excludes a gradual growth as observed in 2019. On the contrary, it suggests that sea ice went through a break up process following intense wave activities, which occurred a few days earlier than the reported measurements.

7.4.2.4 Floe size distribution

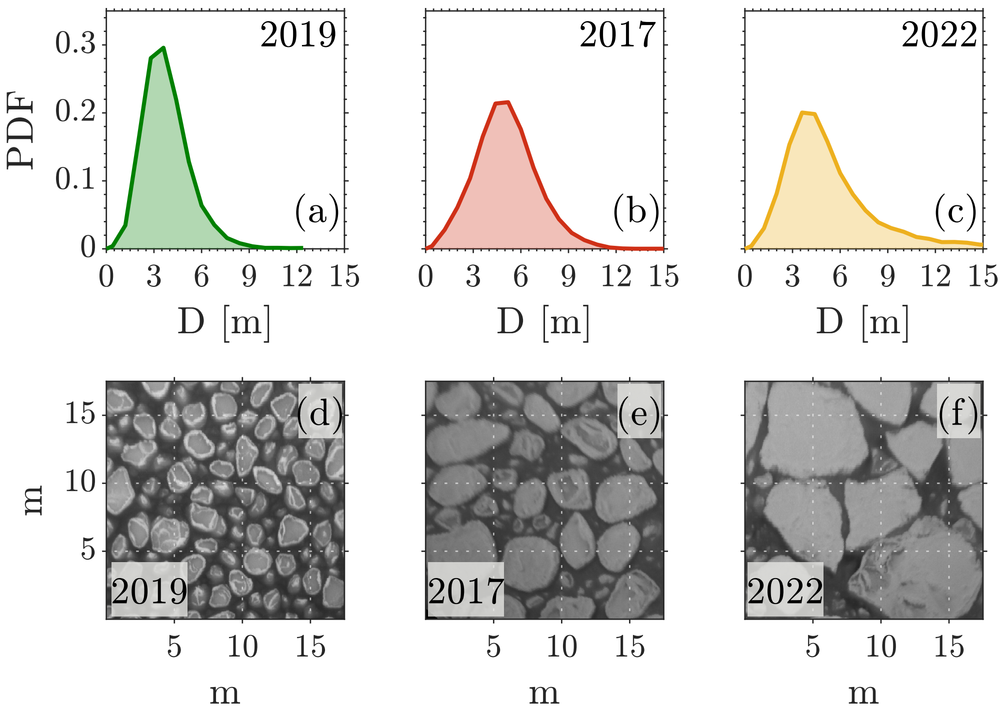

Figure 7.7: Probability density function of floe diameter (continuous line) for 2017 (a), 2019 (b), and 2022 (d). Examples of floes during the expeditions are reported in panels (d, e, f) respectively.

The empirical probability density functions for floe diameter during each expedition are shown in Figure 7.7. The distributions are not presented in chronological order but are displayed to follow the different states of sea ice (see sample images in Figure 7.7d-f). In 2019, the icebreaker encountered the ice during the initial stages of floe formation. This is further substantiated by the round, pancake-like, shape of the ice floes in Figure 7.7d.

This resulted in a narrow, bell-shaped probability density function with a modal diameter of 3.5 meters. In contrast, the probability density functions from 2017 and 2022 exhibit a broader shape, each with a modal diameter of 4.5 meters, indicating a greater diversity in floe sizes.

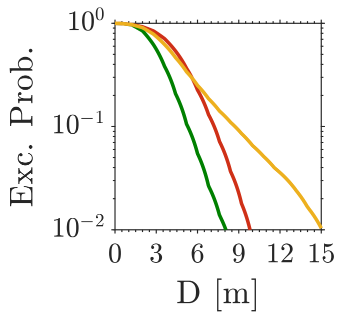

FIGURE 7.8: Exceedance probability in log scale of floe diameter in 2017 (red), 2019 (green) and 2022 (yellow).

The 2017 expedition reported floes that were fully formed, also due to interstitial solid frazil ice that constrained further increase in dimension. There is evidence of welded floes, which also gives rise to larger conglomerated floes. The shape of the floe is still of elliptical or circular type (even those of conglomerated floes), which is typical of pancakes (a form of sea ice in formation). This produced a rightward skew in the probability density function relative to the distribution observed in 2019, indicating a higher probability of encountering larger floes with some exceeding 9 meters. The increased probability for larger floes is highlighted in Figure 7.8, where the exceedance probability of the floe size represented in a semi-logarithmic scale is reported. Interestingly, relative to the 2019 data set, the tail of the distribution shows a clear shift towards higher values, while the tail of the distribution retains the same form. This substantiates, to some extent, an advanced phase of sea ice growth with consistent ice form but with greater dimensions.

In 2022, the trend towards larger floes is even more pronounced than in 2017, with many records of multiple pancake-like forms welded together. As shown in Figure 7.7f, however, the edges of the floe are more irregular and sharp than those observed in 2017 and 2019 (Figure 7.7d,e). This is not the characteristic boundary typical of pancakes, but it rather represents conditions of broken or brash ice, supporting the earlier conjecture that the sea ice floes observed in 2022 are the result of breakup events. Despite having the same mode as in 2017, the right tail of the probability density function extends further, suggesting an increased likelihood of encountering substantially larger floes. The abundance of large floe is reported more clearly by the exceedance probability in Figure 7.8, which shows a very distinctive deviation from the distribution observed in 2017. This departure starts at a floe size of about 6 m.

7.5 Conclusions

The integration of SAM and GVF algorithms enhances ice floe segmentation by compensating for the individual limitations of each method when used independently. The hybrid SAM-GVF approach combines SAM's global learning and pattern recognition capabilities with GVF's precise, shape-informed segmentation. This combination effectively addresses complex scenarios such as adjacent floes with unclear boundaries, significantly improving detection accuracy.

A detailed evaluation of floe statistics from a controlled subset of 10 images demonstrates that the combined method substantially outperforms individual algorithms, especially in accurately separating floes in densely packed ice. These methods, including GVF, SAM, and combined SAM-GVF, are evaluated against manual segmentation. The comparison reveals that while SAM excels at distinguishing between ice and water, GVF tends to underestimate floe numbers but provides accurate outlines when correctly identifying floes. The combined SAM-GVF method effectively balances these strengths and weaknesses, offering more precise floe identification and size estimation, suggesting potential for (almost) real-time sea ice monitoring.

The analysis is further extended to floe size distribution across the entire imagery database arising from three Antarctic expeditions. The best-performing SAM-GVF algorithm was applied to this end. The results indicate a correlation with distance from the ice edge that depends on the stage of growth of the sea ice. A clear increasing trend was observed in 2019, where the ice cover was composed of pancake-like floes, a typical form of growing ice. The small dimensions near the edge were attributed to intense wave activity, while the reduction of it into the marginal ice zone facilitated welding and thus an increase of dimensions. In the 2017 voyage, ice was developing into a consolidated cover. Floes have pancake-like form, but interstitial frazil ice was solidifying, constraining further increase of floe size. Although an increasing trend was still evident, this was weak. In 2022, observations revealed a more dynamic scenario in which sea ice was subjected to breakup events as substantiated by more irregular and sharp floe edges. This resulted in an erratic trend with floes first increasing, then decreasing, and eventually increasing again with distance from the edge.

Overall, these findings highlight the effectiveness of the SAM-GVF algorithm in adapting to varied and complex sea ice conditions, offering detailed insights into floe size distributions crucial for understanding and predicting changes in polar marine environments.

Chapter 8

Conclusions

8.1 Recapitulation

Computer vision is a well recognised tool for measuring the properties of sea ice. This dissertation showcases the development and refinement of advanced segmentation algorithms specifically designed for the complex and varied conditions of Antarctic sea ice. Imagery from a controlled laboratory set up as well as field observation of the Antarctic marginal ice zone is used to this end. By enhancing the segmentation of sea ice images, this research tackles the challenge of data scarcity in polar regions, enabling retrieval of sea ice data from images acquired by ship-borne sensors of varying image quality. The outcomes of this study are crucial for deepening our understanding of and improving our predictive capabilities regarding changes at high latitudes, thereby making a significant contribution to climate science.

In the first instance, the dissertation focuses on the analysis of imagery of model ice in laboratory facilities. This revealed that traditional segmentation techniques, such as image binarization and edge detection filters, operate well in controlled settings. However, their extension to field data shows inadequacy for the diverse conditions encountered in a natural sea ice field. In the laboratory, constant conditions—where lighting and ice texture remain consistent—allow for the capture of clear and distinct features, facilitating detection. This differs markedly from field conditions, which are unpredictable, with ice shapes varying seasonally and resulting in low image quality. Furthermore, ice floes in the laboratory exhibit a fairly consistent elliptical shape, making the application of segmentation algorithms more effective compared to field imagery, where the shape of the floe is arbitrary. The controlled variables in the laboratory also negate the need for pixel-to-meter conversion, as dimensions and geometric properties can be inferred using reference measurements or by directly measuring the ice dimensions in the tank.

Although laboratory data provides a good alternative to realistic conditions, they remain an approximation of realistic conditions. Therefore, the focus of the thesis was then shifted towards the analysis of real field conditions with the particular aim of adapting segmentation algorithms to cope with a broad range of image quality. Imagery data was acquired from an icebreaker vessel during three Antarctic expeditions. The constant motion of the ship was a challenge for data capture and a robust methodology was essential for reliable results. In this respect, the thesis discussed the installation and operation of a camera system aboard the icebreaker S.A. Agulhas II. The system operated during three winter expeditions in 2017, 2019, and 2022 and acquired more than 130,000 images. Of those, 9,000 images were selected for further processes, to ensure Independence in the data set. Essential pre-processing such as detailed camera calibration and orthorectification were discussed to mitigate geometric distortions. These steps were accomplished without the need to reference known objects within the camera's field of view. By effectively adjusting these distortions, the system enabled precise meter-to-pixel conversions, crucial for the accurate measurement and analysis of ice floe sizes.

To evaluate segmentation techniques, manual segmentation of a set of images was used as a high-quality benchmark. To this end, only a few selected images representing a variety of conditions found in Antarctica, including optimal scenarios with well-defined floes and uniform lighting, and challenging images taken at night or under variable lighting conditions where the ice gradient differs across and within floes, were selected. This benchmark also served to verify the accuracy of the orthorectification process. In this regard, the position of the camera changes according to the movement of the ship induced by the ocean waves. Sensitivity analysis performed on a sample of floes for extreme values recorded during rough waves shows that the final influence on the size of the floes is less than 5% compared to a steady ocean, thus negligible.

After pre-processing, the dissertation continues with the evaluation of advanced segmentation algorithms for identifying and analyzing sea ice floes, integrating several methodologies to enhance accuracy and efficiency. One of the algorithms is the Gradient Vector Flow (GVF) snake algorithm, which uses an automated initial contour generator to mimic ice floe shapes. Its advantage is the relatively low computational time and its capacity to adapt to varied conditions. GVF proved to be effective in capturing floe boundaries, even for adjacent floes. However, it relies on initial (guessed) contours. Due to the irregularity of Antarctic sea ice, approximately 20% of the floes in a frame remain unsegmented. While this is not a critical issue for the accuracy of the detected floes – particularly effective for estimating floe size in large datasets where minor inaccuracies are less critical – it limits the suitability for analyzing ice concentration.

A second algorithm that was assessed was the Segment Anything Model (SAM), which operates in two modes: an automatic mask generator and a prompt-based approach. Both modalities cover more ice surface more quickly than the GVF algorithm. However, they struggle with segmenting adjacent floes in complex conditions with non-homogeneous ice gradients and weak edges. The prompt-based modality, which relies on a pre-selection of floes to be processed, excels in separating floes more effectively, although it is susceptible to producing segmentation errors in low-contrast scenarios, necessitating careful application.

Various methods have pros and cons. Therefore, a hybrid algorithm was proposed by integrating SAM and GVF to take advantage of SAM's pattern recognition capabilities and GVF's precise, shape-informed, segmentation. This synergistic method significantly enhances segmentation accuracy, particularly in scenarios with adjacent floes and unclear boundaries, suggesting its potential for near real-time sea ice monitoring. This hybrid method outperforms the individual algorithms, especially in densely packed ice conditions, demonstrating superior capabilities in floe identification and size estimation.

The method was further applied to analyze floe size distribution across an entire imagery database (9,000 images) from three Antarctic expeditions. The analysis indicated that floe size correlates with distance from the ice edge, varying with the stage of ice growth. In 2019, smaller pancake-like floes near the edge grew in size further into the ice zone due to reduced wave activity allowing for floe consolidation. In 2017, though floes also showed pancake-like forms with solidifying frazil ice, the size increase was more constrained. In 2022, the ice experienced more dynamic breakup events, resulting in irregular floe edges and erratic size trends with varying distances from the edge.

Overall, these findings demonstrate the effectiveness of the SAM-GVF algorithm in navigating the complexities of sea ice conditions, providing detailed insights into floe size distributions that are crucial for understanding and forecasting changes in polar marine environments.

8.2 Outlook

Looking ahead, the study highlights several areas for potential improvement and further research. The integration of these image processing techniques into real-time monitoring systems could significantly enhance our understanding of sea ice dynamics. Additionally, future work could focus on refining these models to better handle the variability and complexities of sea ice patterns observed in different conditions and locations.

A pivotal element in advancing this field is the continuous analysis of sea ice cover, enabled by upcoming Antarctic expeditions. These expeditions will provide high-resolution data that are essential for developing and validating sea ice models. The results derived from the hybrid SAM-GVF method can serve as a reliable source for verifying satellite measurements, such as ice concentration. The ability to correlate high-resolution, in-situ data with broader-scale satellite observations will bridge the gap between local observations and global monitoring systems.

Moreover, these detailed observations can lead to enhanced predictive capabilities of sea ice models, which are crucial for anticipating changes in ice dynamics and their subsequent effects on global climate systems. The ongoing development and validation of these models, supported by empirical data from field expeditions, are critical for informing climate policy and enhancing our global response strategies to climate-induced changes in polar regions.

The segmentation masks generated through the hybrid SAM-GVF method can also serve as training data for specialized deep learning models. These models could be developed to distinguish between different types of sea ice, such as ice covered by snow versus bare ice floes, or to calculate the concentration of various ice types accurately.

Currently, the analysis of these characteristics is often qualitative and conducted by visual observers aboard ships. This manual method, while valuable, introduces subjectivity and potential inconsistencies in data collection. By automating this process, we can achieve a more standardized and scalable approach to monitoring sea ice properties. Deep learning models trained on accurately segmented images could automate the detection and classification of ice types, potentially transforming how sea ice is monitored.

This automated approach would not only increase the efficiency and accuracy of sea ice measurements but also enhance the capability to perform these analyses in real-time, even in remote or harsh conditions. As these models evolve, they could integrate seamlessly with satellite imaging and other remote sensing technologies, providing comprehensive and timely insights into sea ice dynamics. Such advancements would significantly contribute to our understanding of polar ecosystems and their responses to environmental changes.

Bibliography

[1] Giulio Passerotti, Luke G. Bennetts, Franz von Bock und Polach, Alberto Alberello, Otto Puolakka, Azam Dolatshah, Jaak Monbaliu, and Alessandro Toffoli. Interactions between irregular wave fields and sea ice: A physical model for wave attenuation and ice breakup in an ice tank. *Journal of Physical Oceanography*, 52 (7):1431–1446, July 2022. ISSN 1520-0485. doi: 10.1175/jpo-d-21-0238.1.

[2] J. J. Voermans, J. Rabault, K. Filchuk, I. Ryzhov, P. Heil, A. Marchenko, C. O. Collins III, M. Dabboor, G. Sutherland, and A. V. Babanin. Experimental evidence for a universal threshold characterizing wave-induced sea ice breakup. *The Cryosphere*, 14(11):4265–4278, November 2020. ISSN 1994-0424. doi: 10.5194/tc-14-4265-2020.

[3] Marzieh H. Derkani, Alberto Alberello, Filippo Nelli, Luke G. Bennetts, Katrin G. Hessner, Keith MacHutchon, Konny Reichert, Lotfi Aouf, Salman Khan, and Alessandro Toffoli. Wind, waves, and surface currents in the southern ocean: observations from the antarctic circumnavigation expedition. *Earth System Science Data*, 13(3):1189–1209, March 2021. ISSN 1866-3516. doi: 10.5194/essd-13-1189-2021.

[4] Alireza Moallemi, Alberto Alberello, Iris Thurnherr, Guangyu Li, Zamin A. Kanji, Filippo Bergamasco, Roman Pohorsky, Filippo Nelli, Alessandro Toffoli, and Julia Schmale. Links between atmospheric aerosols and sea state in the arctic ocean. *Atmospheric Environment*, 338:120844, December 2024. ISSN 1352-2310. doi: 10.1016/j.atmosenv.2024.120844.

[5] Julia Schmale, Andrea Baccarini, Iris Thurnherr, Silvia Henning, Avichay Efraim, Leighton Regayre, Conor Bolas, Markus Hartmann, André Welti, Katrianne Lehtipalo, Franziska Aemisegger, Christian Tatzelt, Sebastian Landwehr, Robin L. Modini, Fiona Tummon, Jill S. Johnson, Neil Harris, Martin Schnaiter, Alessandro Toffoli, Marzieh Derkani, Nicolas Bukowiecki, Frank Stratmann, Josef Dommen, Urs Baltensperger, Heini Wernli, Daniel Rosenfeld, Martin Gysel-Beer, and Ken S. Carslaw. Overview of the antarctic circumnavigation expedition: Study

of preindustrial-like aerosols and their climate effects (ace-space). *Bulletin of the American Meteorological Society*, 100(11):2260–2283, November 2019. ISSN 1520-0477. doi: 10.1175/bams-d-18-0187.1.

[6] Marcello Vichi. An indicator of sea ice variability for the antarctic marginal ice zone. *The Cryosphere*, 16(10):4087–4106, October 2022. ISSN 1994-0424. doi: 10.5194/tc-16-4087-2022.

[7] Ashleigh Womack, Marcello Vichi, Alberto Alberello, and Alessandro Toffoli. Atmospheric drivers of a winter-to-spring lagrangian sea-ice drift in the eastern antarctic marginal ice zone. *Journal of Glaciology*, pages 1–15, March 2022. ISSN 1727-5652. doi: 10.1017/jog.2022.14.

[8] Mark A. Bourassa, Sarah T. Gille, Cecilia Bitz, David Carlson, Ivana Cerovecki, Carol Anne Clayson, Meghan F. Cronin, Will M. Drennan, Chris W. Fairall, Ross N. Hoffman, Gudrun Magnusdottir, Rachel T. Pinker, Ian A. Renfrew, Mark Serreze, Kevin Speer, Lynne D. Talley, and Gary A. Wick. High-latitude ocean and sea ice surface fluxes: Challenges for climate research. *Bulletin of the American Meteorological Society*, 94(3):403–423, March 2013. ISSN 1520-0477. doi: 10.1175/bams-d-11-00244.1.

[9] A WORBY. Studies of the antarctic sea ice edge and ice extent from satellite and ship observations. *Remote Sensing of Environment*, 92(1):98–111, July 2004. ISSN 0034-4257. doi: 10.1016/j.rse.2004.05.007.

[10] Ehlke Hepworth, Marcello Vichi, Armand van Zuydam, Nicole Catherine Taylor, Jesslyn Bossau, Martinique Engelbrecht, and Tor Aarskog. Sea ice observations in the antarctic marginal ice zone during winter 2019, 2020.

[11] Ippolita Tersigni, Alberto Alberello, Gabriele Messori, Marcello Vichi, Miguel Onorato, and Alessandro Toffoli. High-resolution thermal imaging in the antarctic marginal ice zone: Skin temperature heterogeneity and effects on heat fluxes. *Earth and Space Science*, 10(9), September 2023. ISSN 2333-5084. doi: 10.1029/2023ea003078.

[12] Sebastian Landwehr, Michele Volpi, F. Alexander Haumann, Charlotte M. Robinson, Iris Thurnherr, Valerio Ferracci, Andrea Baccarini, Jenny Thomas, Irina Gorodetskaya, Christian Tatzelt, Silvia Henning, Rob L. Modini, Heather J. Forrer, Yajuan Lin, Nicolas Cassar, Rafel Simó, Christel Hassler, Alireza Moallemi, Sarah E. Fawcett, Neil Harris, Ruth Airs, Marzieh H. Derkani, Alberto Alberello, Alessandro Toffoli, Gang Chen, Pablo Rodríguez-Ros, Marina Zamanillo, Pau

Cortés-Greus, Lei Xue, Conor G. Bolas, Katherine C. Leonard, Fernando Perez-Cruz, David Walton, and Julia Schmale. Exploring the coupled ocean and atmosphere system with a data science approach applied to observations from the antarctic circumnavigation expedition. *Earth System Dynamics*, 12(4):1295–1369, November 2021. ISSN 2190-4987. doi: 10.5194/esd-12-1295-2021.

[13] Nabil Panchi and Ekaterina Kim. Deep learning strategies for analysis of weather-degraded optical sea ice images. *IEEE Sensors Journal*, 24(9):15252–15272, May 2024. ISSN 2379-9153. doi: 10.1109/jsen.2024.3376518.

[14] Andrei Sandru, Heikki Hyyti, Arto Visala, and Pentti Kujala. A complete process for shipborne sea-ice field analysis using machine vision. *IFAC-PapersOnLine*, 53 (2):14539–14545, 2020. ISSN 2405-8963. doi: 10.1016/j.ifacol.2020.12.1458.

[15] Qin Zhang and Nick Hughes. Ice floe segmentation and floe size distribution in airborne and high-resolution optical satellite images: towards an automated labelling deep learning approach. *The Cryosphere*, 17(12):5519–5537, December 2023. ISSN 1994-0424. doi: 10.5194/tc-17-5519-2023.

[16] Qin Zhang and Roger Skjetne. Image processing for identification of sea-ice floes and the floe size distributions. *IEEE Transactions on Geoscience and Remote Sensing*, 53(5):2913–2924, May 2015. ISSN 1558-0644. doi: 10.1109/tgrs.2014.2366640.

[17] Sebastian Skatulla, Riesna R. Audh, Andrea Cook, Ehlke Hepworth, Siobhan Johnson, Doru C. Lupascu, Keith MacHutchon, Rutger Marquart, Tommy Mielke, Emmanuel Omatuku, Felix Paul, Tokoloho Rampai, Jörg Schröder, Carina Schwarz, and Marcello Vichi. Physical and mechanical properties of winter first-year ice in the antarctic marginal ice zone along the good hope line. *The Cryosphere*, 16(7):2899–2925, July 2022. ISSN 1994-0424. doi: 10.5194/tc-16-2899-2022.

[18] Shengxi Gui, Shuang Song, Rongjun Qin, and Yang Tang. Remote sensing object detection in the deep learning era—a review. *Remote Sensing*, 16(2):327, January 2024. ISSN 2072-4292. doi: 10.3390/rs16020327.

[19] Lefei Zhang and Liangpei Zhang. Artificial intelligence for remote sensing data analysis: A review of challenges and opportunities. *IEEE Geoscience and Remote Sensing Magazine*, 10(2):270–294, June 2022. ISSN 2373-7468. doi: 10.1109/mgrs.2022.3145854.

[20] Judith A. Curry, Julie L. Schramm, and Elizabeth E. Ebert. Sea ice-albedo climate feedback mechanism. *Journal of Climate*, 8(2):240–247, February 1995. ISSN 1520-0442. doi: 10.1175/1520-0442(1995)008⟨0240:siacfm⟩2.0.co;2.

[21] Andrea Riedel, Christine Michel, Michel Gosselin, and Bernard LeBlanc. Winter–spring dynamics in sea-ice carbon cycling in the coastal arctic ocean. *Journal of Marine Systems*, 74(3–4):918–932, December 2008. ISSN 0924-7963. doi: 10.1016/j.jmarsys.2008.01.003.

[22] D. A. Rothrock and A. S. Thorndike. Measuring the sea ice floe size distribution. *Journal of Geophysical Research: Oceans*, 89(C4):6477–6486, July 1984. ISSN 0148-0227. doi: 10.1029/jc089ic04p06477.

[23] Christopher Horvat. Floes, the marginal ice zone and coupled wave-sea-ice feedbacks. *Philosophical Transactions of the Royal Society A: Mathematical, Physical and Engineering Sciences*, 380(2235), September 2022. ISSN 1471-2962. doi: 10.1098/rsta.2021.0252.

[24] Alberto Alberello, Luke G. Bennetts, Miguel Onorato, Marcello Vichi, Keith MacHutchon, Clare Eayrs, Butteur Ntamba Ntamba, Alvise Benetazzo, Filippo Bergamasco, Filippo Nelli, Rohinee Pattani, Hans Clarke, Ippolita Tersigni, and Alessandro Toffoli. Three-dimensional imaging of waves and floes in the marginal ice zone during a cyclone. *Nature Communications*, 13(1), August 2022. ISSN 2041-1723. doi: 10.1038/s41467-022-32036-2.

[25] Christopher Horvat, Eli Tziperman, and Jean-Michel Campin. Interaction of sea ice floe size, ocean eddies, and sea ice melting. *Geophysical Research Letters*, 43 (15):8083–8090, August 2016. ISSN 1944-8007. doi: 10.1002/2016gl069742.

[26] Michel Tsamados, Daniel L. Feltham, David Schroeder, Daniela Flocco, Sinead L. Farrell, Nathan Kurtz, Seymour W. Laxon, and Sheldon Bacon. Impact of variable atmospheric and oceanic form drag on simulations of arctic sea ice*. *Journal of Physical Oceanography*, 44(5):1329–1353, April 2014. ISSN 1520-0485. doi: 10.1175/jpo-d-13-0215.1.

[27] Christof Lüpkes, Vladimir M. Gryanik, Jörg Hartmann, and Edgar L. Andreas. A parametrization, based on sea ice morphology, of the neutral atmospheric drag coefficients for weather prediction and climate models. *Journal of Geophysical Research: Atmospheres*, 117(D13), July 2012. ISSN 0148-0227. doi: 10.1029/2012jd017630.

[28] Daniel L Feltham. Granular flow in the marginal ice zone. *Philosophical Transactions of the Royal Society A: Mathematical, Physical and Engineering Sciences*, 363(1832):1677–1700, July 2005. ISSN 1471-2962. doi: 10.1098/rsta.2005.1601.

[29] Agnieszka Herman, Marta Wenta, and Sukun Cheng. Sizes and shapes of sea ice floes broken by waves–a case study from the east antarctic coast. *Frontiers in Earth Science*, 9, May 2021. ISSN 2296-6463. doi: 10.3389/feart.2021.655977.

[30] A. Dolatshah, F. Nelli, L. G. Bennetts, A. Alberello, M. H. Meylan, J. P. Monty, and A. Toffoli. Letter: Hydroelastic interactions between water waves and floating freshwater ice. *Physics of Fluids*, 30(9), September 2018. ISSN 1089-7666. doi: 10.1063/1.5050262.

[31] Fabien Montiel, V. A. Squire, and L. G. Bennetts. Attenuation and directional spreading of ocean wave spectra in the marginal ice zone. *Journal of Fluid Mechanics*, 790:492–522, February 2016. ISSN 1469-7645. doi: 10.1017/jfm.2016.21.

[32] Michael H. Meylan, Christopher Horvat, Cecilia M. Bitz, and Luke G. Bennetts. A floe size dependent scattering model in two- and three-dimensions for wave attenuation by ice floes. *Ocean Modelling*, 161:101779, May 2021. ISSN 1463-5003. doi: 10.1016/j.ocemod.2021.101779.

[33] Yanan Wang, Byongjun Hwang, Adam William Bateson, Yevgeny Aksenov, and Christopher Horvat. Summer sea ice floe perimeter density in the arctic: high-resolution optical satellite imagery and model evaluation. *The Cryosphere*, 17(8): 3575–3591, August 2023. ISSN 1994-0424. doi: 10.5194/tc-17-3575-2023.

[34] Alberto Alberello, Miguel Onorato, Luke Bennetts, Marcello Vichi, Clare Eayrs, Keith MacHutchon, and Alessandro Toffoli. Brief communication: Pancake ice floe size distribution during the winter expansion of the antarctic marginal ice zone. *The Cryosphere*, 13(1):41–48, January 2019. ISSN 1994-0424. doi: 10.5194/tc-13-41-2019.

[35] Alberto Alberello, Azam Dolatshah, Luke G Bennetts, Miguel Onorato, Filippo Nelli, and Alessandro Toffoli. A physical model of wave attenuation in pancake ice. *International Journal of Offshore and Polar Engineering*, 31(3):263–269, September 2021. ISSN 1053-5381. doi: 10.17736/ijope.2021.ik08.

[36] F. Parmiggiani, M. Moctezuma-Flores, P. Wadhams, and G. Aulicino. Image processing for pancake ice detection and size distribution computation. *International Journal of Remote Sensing*, 40(9):3368–3383, November 2018. ISSN 1366-5901. doi: 10.1080/01431161.2018.1541367.

[37] B. Weissling, S. Ackley, P. Wagner, and H. Xie. Eiscam — digital image acquisition and processing for sea ice parameters from ships. *Cold Regions Science and Technology*, 57(1):49–60, June 2009. ISSN 0165-232X. doi: 10.1016/j.coldregions.2009.01.001.

[38] Nahed M. Alsharay, Yuanzhu Chen, Octavia A. Dobre, and Oscar De Silva. Improved sea-ice identification using semantic segmentation with raindrop removal. *IEEE Access*, 10:21599–21607, 2022. ISSN 2169-3536. doi: 10.1109/access.2022.3150969.

[39] Wenjun Lu, Qin Zhang, Raed Lubbad, Sveinung Løset, and Roger Skjetne. A shipborne measurement system to acquire sea ice thickness and concentration at engineering scale. In *All Days*, 16OARC. OTC, October 2016. doi: 10.4043/27361-ms.

[40] Chengqian Zhang, Xiaodong Chen, and Shunying Ji. Semantic image segmentation for sea ice parameters recognition using deep convolutional neural networks. *International Journal of Applied Earth Observation and Geoinformation*, 112:102885, August 2022. ISSN 1569-8432. doi: 10.1016/j.jag.2022.102885.

[41] Nabil Panchi, Ekaterina Kim, and Anirban Bhattacharyya. Supplementing remote sensing of ice: Deep learning-based image segmentation system for automatic detection and localization of sea-ice formations from close-range optical images. *IEEE Sensors Journal*, 21(16):18004–18019, August 2021. ISSN 2379-9153. doi: 10.1109/jsen.2021.3084556.

[42] Hans-Martin Heyn, Martin Knoche, Qin Zhang, and Roger Skjetne. A system for automated vision-based sea-ice concentration detection and floe-size distribution indication from an icebreaker. In *Volume 8: Polar and Arctic Sciences and Technology; Petroleum Technology*, OMAE2017. American Society of Mechanical Engineers, June 2017. doi: 10.1115/omae2017-61822.

[43] P. Lu, Z. J. Li, Z. H. Zhang, and X. L. Dong. Aerial observations of floe size distribution in the marginal ice zone of summer prydz bay. *Journal of Geophysical Research: Oceans*, 113(C2), February 2008. ISSN 0148-0227. doi: 10.1029/2006jc003965.

[44] Elie Dumas-Lefebvre and Dany Dumont. Aerial observations of sea ice breakup by ship waves. *The Cryosphere*, 17(2):827–842, February 2023. ISSN 1994-0424. doi: 10.5194/tc-17-827-2023.

[45] Z. Zhang. A flexible new technique for camera calibration. *IEEE Transactions on Pattern Analysis and Machine Intelligence*, 22(11):1330–1334, 2000. ISSN 0162-8828. doi: 10.1109/34.888718.

[46] David Arthur and Sergei Vassilvitskii. K-means++ the advantages of careful seeding. In *Proceedings of the eighteenth annual ACM-SIAM symposium on Discrete algorithms*, pages 1027–1035, 2007.

[47] Benjamin Dowden, Oscar De Silva, Weimin Huang, and Dan Oldford. Sea ice classification via deep neural network semantic segmentation. *IEEE Sensors Journal*, 21(10):11879–11888, May 2021. ISSN 2379-9153. doi: 10.1109/jsen.2020.3031475.

[48] Martin Maška, Vladimír Ulman, Pablo Delgado-Rodriguez, Estibaliz Gómez-de Mariscal, Tereza Nečasová, Fidel A. Guerrero Peña, Tsang Ing Ren, Elliot M. Meyerowitz, Tim Scherr, Katharina Löffler, Ralf Mikut, Tianqi Guo, Yin Wang, Jan P. Allebach, Rina Bao, Noor M. Al-Shakarji, Gani Rahmon, Imad Eddine Toubal, Kannappan Palaniappan, Filip Lux, Petr Matula, Ko Sugawara, Klas E. G. Magnusson, Layton Aho, Andrew R. Cohen, Assaf Arbelle, Tal Ben-Haim, Tammy Riklin Raviv, Fabian Isensee, Paul F. Jäger, Klaus H. Maier-Hein, Yanming Zhu, Cristina Ederra, Ainhoa Urbiola, Erik Meijering, Alexandre Cunha, Arrate Muñoz-Barrutia, Michal Kozubek, and Carlos Ortiz-de Solórzano. The cell tracking challenge: 10 years of objective benchmarking. *Nature Methods*, 20(7): 1010–1020, May 2023. ISSN 1548-7105. doi: 10.1038/s41592-023-01879-y.

[49] Wenjun Huang, Anzhu Yu, Qing Xu, Qun Sun, Wenyue Guo, Song Ji, Bowei Wen, and Chunping Qiu. Sea ice extraction via remote sensing imagery: Algorithms, datasets, applications and challenges. *Remote Sensing*, 16(5):842, February 2024. ISSN 2072-4292. doi: 10.3390/rs16050842.

[50] Zhaohui Wang, Alexander D. Fraser, Phillip Reid, Siobhan O'Farrell, and Richard Coleman. Antarctic sea ice surface temperature bias in atmospheric reanalyses induced by the combined effects of sea ice and clouds. *Communications Earth & Environment*, 5(1), October 2024. ISSN 2662-4435. doi: 10.1038/s43247-024-01692-1.

[51] P. Wadhams, G. Aulicino, F. Parmiggiani, P. O. G. Persson, and B. Holt. Pancake ice thickness mapping in the beaufort sea from wave dispersion observed in sar imagery. *Journal of Geophysical Research: Oceans*, 123(3):2213–2237, March 2018. ISSN 2169-9291. doi: 10.1002/2017jc013003.

[52] Natalia Zakhvatkina, Vladimir Smirnov, and Irina Bychkova. Satellite sar data-based sea ice classification: An overview. *Geosciences*, 9(4):152, March 2019. ISSN 2076-3263. doi: 10.3390/geosciences9040152.

[53] J. Karvonen, M. Simila, and M. Makynen. Open water detection from baltic sea ice radarsat-1 sar imagery. *IEEE Geoscience and Remote Sensing Letters*, 2(3): 275–279, July 2005. ISSN 1545-598X. doi: 10.1109/lgrs.2005.847930.

[54] D. Haverkamp, Leen Kiat Soh, and C. Tsatsoulis. A comprehensive, automated approach to determining sea ice thickness from sar data. *IEEE Transactions on Geoscience and Remote Sensing*, 33(1):46–57, 1995. ISSN 0196-2892. doi: 10.1109/36.368223.

[55] Yanmei Chai, Jinchang Ren, Byongjun Hwang, Jian Wang, Dan Fan, Yijun Yan, and Shiwei Zhu. Texture-sensitive superpixeling and adaptive thresholding for effective segmentation of sea ice floes in high-resolution optical images. *IEEE Journal of Selected Topics in Applied Earth Observations and Remote Sensing*, 14:577–586, 2021. ISSN 2151-1535. doi: 10.1109/jstars.2020.3040614.

[56] Xiao-Ming Li, Yan Sun, and Qiang Zhang. Extraction of sea ice cover by sentinel-1 sar based on support vector machine with unsupervised generation of training data. *IEEE Transactions on Geoscience and Remote Sensing*, 59(4):3040–3053, April 2021. ISSN 1558-0644. doi: 10.1109/tgrs.2020.3007789.

[57] Alexander Kirillov, Eric Mintun, Nikhila Ravi, Hanzi Mao, Chloe Rolland, Laura Gustafson, Tete Xiao, Spencer Whitehead, Alexander C. Berg, Wan-Yen Lo, Piotr Dollár, and Ross Girshick. Segment anything, 2023.

[58] Siddharth Shankar, Leigh A. Stearns, and C. J. van der Veen. Semantic segmentation of glaciological features across multiple remote sensing platforms with the segment anything model (sam). *Journal of Glaciology*, pages 1–10, November 2023. ISSN 1727-5652. doi: 10.1017/jog.2023.95.

[59] Agnieszka Herman, Karl-Ulrich Evers, and Nils Reimer. Floe-size distributions in laboratory ice broken by waves. *The Cryosphere*, 12(2):685–699, February 2018. ISSN 1994-0424. doi: 10.5194/tc-12-685-2018.

[60] Q. Zhang, R. Skjetne, I. Metrikin, and S. Løset. Image processing for ice floe analyses in broken-ice model testing. *Cold Regions Science and Technology*, 111: 27–38, March 2015. ISSN 0165-232X. doi: 10.1016/j.coldregions.2014.12.004.

[61] Seok-Ho Byun and Jong-Ho Nam. Estimation of pack ice concentration using histogram peak analysis and image subdivision. *Cold Regions Science and Technology*, 181:103185, January 2021. ISSN 0165-232X. doi: 10.1016/j.coldregions.2020.103185.

[62] Li Zhou, Jinyan Cai, and Shifeng Ding. The identification of ice floes and calculation of sea ice concentration based on a deep learning method. *Remote Sensing*, 15(10):2663, May 2023. ISSN 2072-4292. doi: 10.3390/rs15102663.

[63] Vernon A. Squire. Past, present and impendent hydroelastic challenges in the polar and subpolar seas. *Philosophical Transactions of the Royal Society A: Mathematical, Physical and Engineering Sciences*, 369(1947):2813–2831, July 2011. ISSN 1471-2962. doi: 10.1098/rsta.2011.0093.

[64] Vernon A. Squire. Ocean wave interactions with sea ice: A reappraisal. *Annual Review of Fluid Mechanics*, 52(1):37–60, January 2020. ISSN 1545-4479. doi: 10.1146/annurev-fluid-010719-060301.

[65] Kenneth M. Golden, Luke G. Bennetts, Elena Cherkaev, Ian Eisenman, Daniel Feltham, Christopher Horvat, Elizabeth Hunke, Christopher Jones, Donald K. Perovich, Pedro Ponte-Castaneda, Courtenay Strong, Deborah Sulsky, and Andrew J. Wells. Modeling sea ice. *Notices of the American Mathematical Society*, 67(10):1, November 2020. ISSN 1088-9477. doi: 10.1090/noti2171.

[66] A. L. Kohout, M. J. M. Williams, S. M. Dean, and M. H. Meylan. Storm-induced sea-ice breakup and the implications for ice extent. *Nature*, 509(7502):604–607, May 2014. ISSN 1476-4687. doi: 10.1038/nature13262.

[67] Alison L. Kohout, Madison Smith, Lettie A. Roach, Guy Williams, Fabien Montiel, and Michael J. M. Williams. Observations of exponential wave attenuation in antarctic sea ice during the pipers campaign. *Annals of Glaciology*, 61(82):196–209, June 2020. ISSN 1727-5644. doi: 10.1017/aog.2020.36.

[68] J. Thomson, S. Ackley, F. Girard-Ardhuin, F. Ardhuin, A. Babanin, G. Boutin, J. Brozena, S. Cheng, C. Collins, M. Doble, C. Fairall, P. Guest, C. Gebhardt, J. Gemmrich, H. C. Graber, B. Holt, S. Lehner, B. Lund, M. H. Meylan, T. Maksym, F. Montiel, W. Perrie, O. Persson, L. Rainville, W. E. Rogers, H. Shen, H. Shen, V. A. Squire, S. Stammerjohn, J. Stopa, M. M. Smith, P. Sutherland, and P. Wadhams. Overview of the arctic sea state and boundary layer physics program. *Journal of Geophysical Research: Oceans*, 123(12):8674–8687, December 2018. ISSN 2169-9291. doi: 10.1002/2018jc013766.

[69] M. Vichi, C. Eayrs, A. Alberello, A. Bekker, L. Bennetts, D. Holland, E. de Jong, W. Joubert, K. MacHutchon, G. Messori, J. F. Mojica, M. Onorato, C. Saunders, S. Skatulla, and A. Toffoli. Effects of an explosive polar cyclone crossing the antarctic marginal ice zone. *Geophysical Research Letters*, 46(11):5948–5958, June 2019. ISSN 1944-8007. doi: 10.1029/2019gl082457.

[70] Martin J. Doble and Jean-Raymond Bidlot. Wave buoy measurements at the antarctic sea ice edge compared with an enhanced ecmwf wam: Progress towards global waves-in-ice modelling. *Ocean Modelling*, 70:166–173, October 2013. ISSN 1463-5003. doi: 10.1016/j.ocemod.2013.05.012.

[71] Fabrice Ardhuin, Guillaume Boutin, Justin Stopa, Fanny Girard-Ardhuin, Christian Melsheimer, Jim Thomson, Alison Kohout, Martin Doble, and Peter Wadhams. Wave attenuation through an arctic marginal ice zone on 12 october 2015: 2. numerical modeling of waves and associated ice breakup. *Journal of Geophysical Research: Oceans*, 123(8):5652–5668, August 2018. ISSN 2169-9291. doi: 10.1002/2018jc013784.

[72] Michael H. Meylan, Will Perrie, Bechara Toulany, Yongcun Hu, and Michael P. Casey. On the three-dimensional scattering of waves by flexible marginal ice floes. *Journal of Geophysical Research: Oceans*, 125(12), December 2020. ISSN 2169-9291. doi: 10.1029/2019jc015868.

[73] W. Erick Rogers, Michael H. Meylan, and Alison L. Kohout. Estimates of spectral wave attenuation in antarctic sea ice, using model/data inversion. *Cold Regions Science and Technology*, 182:103198, February 2021. ISSN 0165-232X. doi: 10.1016/j.coldregions.2020.103198.

[74] Luke G. Bennetts, Siobhan O'Farrell, and Petteri Uotila. Brief communication: Impacts of ocean-wave-induced breakup of antarctic sea ice via thermodynamics in a stand-alone version of the cice sea-ice model. *The Cryosphere*, 11(3):1035–1040, May 2017. ISSN 1994-0424. doi: 10.5194/tc-11-1035-2017.

[75] Lettie A. Roach, Cecilia M. Bitz, Christopher Horvat, and Samuel M. Dean. Advances in modeling interactions between sea ice and ocean surface waves. *Journal of Advances in Modeling Earth Systems*, 11(12):4167–4181, December 2019. ISSN 1942-2466. doi: 10.1029/2019ms001836.

[76] Adam W. Bateson, Daniel L. Feltham, David Schröder, Lucia Hosekova, Jeff K. Ridley, and Yevgeny Aksenov. Impact of sea ice floe size distribution on seasonal fragmentation and melt of arctic sea ice. *The Cryosphere*, 14(2):403–428, February 2020. ISSN 1994-0424. doi: 10.5194/tc-14-403-2020.

[77] Guillaume Boutin, Timothy Williams, Pierre Rampal, Einar Olason, and Camille Lique. Wave–sea-ice interactions in a brittle rheological framework. *The Cryosphere*, 15(1):431–457, January 2021. ISSN 1994-0424. doi: 10.5194/tc-15-431-2021.

[78] D. Dumont, A. Kohout, and L. Bertino. A wave-based model for the marginal ice zone including a floe breaking parameterization. *Journal of Geophysical Research*, 116(C4), April 2011. ISSN 0148-0227. doi: 10.1029/2010jc006682.

[79] Timothy D. Williams, Luke G. Bennetts, Vernon A. Squire, Dany Dumont, and Laurent Bertino. Wave–ice interactions in the marginal ice zone. part 1: Theoretical foundations. *Ocean Modelling*, 71:81–91, November 2013. ISSN 1463-5003. doi: 10.1016/j.ocemod.2013.05.010.

[80] Timothy D. Williams, Luke G. Bennetts, Vernon A. Squire, Dany Dumont, and Laurent Bertino. Wave–ice interactions in the marginal ice zone. part 2: Numerical implementation and sensitivity studies along 1d transects of the ocean surface. *Ocean Modelling*, 71:92–101, November 2013. ISSN 1463-5003. doi: 10.1016/j.ocemod.2013.05.011.

[81] Rike Grotmaack and Michael H. Meylan. Wave forcing of small floating bodies. *Journal of Waterway, Port, Coastal, and Ocean Engineering*, 132(3):192–198, May 2006. ISSN 1943-5460. doi: 10.1061/(asce)0733-950x(2006)132:3(192).

[82] Timothy D. Williams, Pierre Rampal, and Sylvain Bouillon. Wave–ice interactions in the nextsim sea-ice model. *The Cryosphere*, 11(5):2117–2135, September 2017. ISSN 1994-0424. doi: 10.5194/tc-11-2117-2017.

[83] L. J. Yiew, L. G. Bennetts, M. H. Meylan, G. A. Thomas, and B. J. French. Wave-induced collisions of thin floating disks. *Physics of Fluids*, 29(12), December 2017. ISSN 1089-7666. doi: 10.1063/1.5003310.

[84] A. Herman. Wave-induced surge motion and collisions of sea ice floes: Finite-floe-size effects. *Journal of Geophysical Research: Oceans*, 123(10):7472–7494, October 2018. ISSN 2169-9291. doi: 10.1029/2018jc014500.

[85] Robert A. Massom and Sharon E. Stammerjohn. Antarctic sea ice change and variability – physical and ecological implications. *Polar Science*, 4(2):149–186, August 2010. ISSN 1873-9652. doi: 10.1016/j.polar.2010.05.001.

[86] D. M. Skene, L. G. Bennetts, M. H. Meylan, and A. Toffoli. Modelling water wave overwash of a thin floating plate. *Journal of Fluid Mechanics*, 777, July 2015. ISSN 1469-7645. doi: 10.1017/jfm.2015.378.

[87] F. Montiel, V. A. Squire, M. Doble, J. Thomson, and P. Wadhams. Attenuation and directional spreading of ocean waves during a storm event in the autumn beaufort sea marginal ice zone. *Journal of Geophysical Research: Oceans*, 123(8): 5912–5932, August 2018. ISSN 2169-9291. doi: 10.1029/2018jc013763.

[88] Fabrice Ardhuin, Fabrice Collard, Bertrand Chapron, Fanny Girard-Ardhuin, Gilles Guitton, Alexis Mouche, and Justin E. Stopa. Estimates of ocean wave heights and attenuation in sea ice using the sar wave mode on sentinel-1a. *Geophysical Research Letters*, 42(7):2317–2325, April 2015. ISSN 1944-8007. doi: 10.1002/2014gl062940.

[89] Peter Sutherland, John Brozena, W. Erick Rogers, Martin Doble, and Peter Wadhams. Airborne remote sensing of wave propagation in the marginal ice zone. *Journal of Geophysical Research: Oceans*, 123(6):4132–4152, June 2018. ISSN 2169-9291. doi: 10.1029/2018jc013785.

[90] Alexander J. Campbell, Adam J. Bechle, and Chin H. Wu. Observations of surface waves interacting with ice using stereo imaging. *Journal of Geophysical Research: Oceans*, 119(6):3266–3284, June 2014. ISSN 2169-9291. doi: 10.1002/2014jc009894.

[91] Michael H. Meylan, Luke G. Bennetts, and Alison L. Kohout. In situ measurements and analysis of ocean waves in the antarctic marginal ice zone. *Geophysical Research Letters*, 41(14):5046–5051, July 2014. ISSN 1944-8007. doi: 10.1002/2014gl060809.

[92] A. L. Kohout and M. H. Meylan. An elastic plate model for wave attenuation and ice floe breaking in the marginal ice zone. *Journal of Geophysical Research: Oceans*, 113(C9), September 2008. ISSN 0148-0227. doi: 10.1029/2007jc004434.

[93] L. G. Bennetts, M. A. Peter, V. A. Squire, and M. H. Meylan. A three-dimensional model of wave attenuation in the marginal ice zone. *Journal of Geophysical Research: Oceans*, 115(C12), December 2010. ISSN 0148-0227. doi: 10.1029/2009jc005982.

[94] L.G. Bennetts and V.A. Squire. Model sensitivity analysis of scattering-induced attenuation of ice-coupled waves. *Ocean Modelling*, 45–46:1–13, January 2012. ISSN 1463-5003. doi: 10.1016/j.ocemod.2012.01.002.

[95] Johannes E. M. Mosig, Fabien Montiel, and Vernon A. Squire. Comparison of viscoelastic-type models for ocean wave attenuation in ice-covered seas. *Journal of Geophysical Research: Oceans*, 120(9):6072–6090, September 2015. ISSN 2169-9291. doi: 10.1002/2015jc010881.

[96] Sukun Cheng, W. Erick Rogers, Jim Thomson, Madison Smith, Martin J. Doble, Peter Wadhams, Alison L. Kohout, Björn Lund, Ola P.G. Persson, Clarence O. Collins, Stephen F. Ackley, Fabien Montiel, and Hayley H. Shen. Calibrating a viscoelastic sea ice model for wave propagation in the arctic fall marginal ice

zone. *Journal of Geophysical Research: Oceans*, 122(11):8770–8793, November 2017. ISSN 2169-9291. doi: 10.1002/2017jc013275.

[97] Clarence O. Collins, W. Erick Rogers, Aleksey Marchenko, and Alexander V. Babanin. In situ measurements of an energetic wave event in the arctic marginal ice zone. *Geophysical Research Letters*, 42(6):1863–1870, March 2015. ISSN 1944-8007. doi: 10.1002/2015gl063063.

[98] Fabrice Ardhuin, Mark Otero, Sophia Merrifield, Antoine Grouazel, and Eric Terrill. Ice breakup controls dissipation of wind waves across southern ocean sea ice. *Geophysical Research Letters*, 47(13), July 2020. ISSN 1944-8007. doi: 10.1029/2020gl087699.

[99] Simon J. Prinsenberg and Ingrid K. Peterson. Observing regional-scale pack-ice decay processes with helicopter-borne sensors and moored upward-looking sonars. *Annals of Glaciology*, 52(57):35–42, 2011. ISSN 1727-5644. doi: 10.3189/172756411795931688.

[100] Matthew G. Asplin, Ryan Galley, David G. Barber, and Simon Prinsenberg. Fracture of summer perennial sea ice by ocean swell as a result of arctic storms. *Journal of Geophysical Research: Oceans*, 117(C6), June 2012. ISSN 0148-0227. doi: 10.1029/2011jc007221.

[101] A.L. Kohout, M.J.M. Williams, T. Toyota, J. Lieser, and J. Hutchings. In situ observations of wave-induced sea ice breakup. *Deep Sea Research Part II: Topical Studies in Oceanography*, 131:22–27, September 2016. ISSN 0967-0645. doi: 10.1016/j.dsr2.2015.06.010.

[102] Luke G. Bennetts, Siobhan O'Farrell, Petteri Uotila, and Vernon A. Squire. An idealized wave–ice interaction model without subgrid spatial or temporal discretizations. *Annals of Glaciology*, 56(69):258–262, 2015. ISSN 1727-5644. doi: 10.3189/2015aog69a599.

[103] G.B. Crocker and P. Wadhams. Breakup of antarctic fast ice. *Cold Regions Science and Technology*, 17(1):61–76, September 1989. ISSN 0165-232X. doi: 10.1016/s0165-232x(89)80016-3.

[104] G.L. Vaughan and V.A. Squire. Wave induced fracture probabilities for arctic sea-ice. *Cold Regions Science and Technology*, 67(1–2):31–36, June 2011. ISSN 0165-232X. doi: 10.1016/j.coldregions.2011.02.003.

[105] Patricia J. Langhorne, Vernon A. Squire, Colin Fox, and Timothy G. Haskell. Break-up of sea ice by ocean waves. *Annals of Glaciology*, 27:438–442, 1998. ISSN 1727-5644. doi: 10.3189/s0260305500017869.

[106] C. Horvat and E. Tziperman. A prognostic model of the sea-ice floe size and thickness distribution. *The Cryosphere*, 9(6):2119–2134, November 2015. ISSN 1994-0424. doi: 10.5194/tc-9-2119-2015.

[107] F. Montiel and V. A. Squire. Modelling wave-induced sea ice break-up in the marginal ice zone. *Proceedings of the Royal Society A: Mathematical, Physical and Engineering Sciences*, 473(2206):20170258, October 2017. ISSN 1471-2946. doi: 10.1098/rspa.2017.0258.

[108] Changpeng Zhang and Xin Zhao. Theoretical model for predicting the break-up of ice covers due to wave-ice interaction. *Applied Ocean Research*, 112:102614, July 2021. ISSN 0141-1187. doi: 10.1016/j.apor.2021.102614.

[109] L.G. Bennetts, A. Alberello, M.H. Meylan, C. Cavaliere, A.V. Babanin, and A. Toffoli. An idealised experimental model of ocean surface wave transmission by an ice floe. *Ocean Modelling*, 96:85–92, December 2015. ISSN 1463-5003. doi: 10.1016/j.ocemod.2015.03.001.

[110] L. G. Bennetts and T. D. Williams. Water wave transmission by an array of floating discs. *Proceedings of the Royal Society A: Mathematical, Physical and Engineering Sciences*, 471(2173):20140698, January 2015. ISSN 1471-2946. doi: 10.1098/rspa.2014.0698.

[111] A. Toffoli, L. G. Bennetts, M. H. Meylan, C. Cavaliere, A. Alberello, J. Elsnab, and J. P. Monty. Sea ice floes dissipate the energy of steep ocean waves. *Geophysical Research Letters*, 42(20):8547–8554, October 2015. ISSN 0094-8276. doi: 10.1002/2015gl065937.

[112] F. Nelli, L.G. Bennetts, D.M. Skene, J.P. Monty, J.H. Lee, M.H. Meylan, and A. Toffoli. Reflection and transmission of regular water waves by a thin, floating plate. *Wave Motion*, 70:209–221, April 2017. ISSN 0165-2125. doi: 10.1016/j.wavemoti.2016.09.003.

[113] Sabrina M. Parra, Dharma K.K. Sree, David Wang, Erick Rogers, Jung H. Lee, Clarence O. Collins, Adrian Wing-Keung Law, and Alexander V. Babanin. Experimental study on surface wave modifications by different ice covers. *Cold Regions Science and Technology*, 174:103042, June 2020. ISSN 0165-232X. doi: 10.1016/j.coldregions.2020.103042.

[114] Marco Klein, Moritz Hartmann, and Franz von Bock und Polach. Note on the application of transient wave packets for wave–ice interaction experiments. *Water*, 13(12):1699, June 2021. ISSN 2073-4441. doi: 10.3390/w13121699.

[115] Sukun Cheng, Andrei Tsarau, Karl-Ulrich Evers, and Hayley Shen. Floe size effect on gravity wave propagation through ice covers. *Journal of Geophysical Research: Oceans*, 124(1):320–334, January 2019. ISSN 2169-9291. doi: 10.1029/2018jc014094.

[116] Z. Li and K. Riska. *Preliminary study of physical and mechanical properties of model ice*. Helsinki University of Technology, Otaniemi, 1996. ISBN 978-951-22-3296-3. OCLC: 58208918.

[117] Rüdiger von Bock und Polach, Sören Ehlers, and Pentti Kujala. Model-scale ice — part a: Experiments. *Cold Regions Science and Technology*, 94:74–81, October 2013. ISSN 0165-232X. doi: 10.1016/j.coldregions.2013.07.001.

[118] Rüdiger U. Franz von Bock und Polach, Robert Ettema, Silke Gralher, Leon Kellner, and Merten Stender. The non-linear behavior of aqueous model ice in downward flexure. *Cold Regions Science and Technology*, 165:102775, September 2019. ISSN 0165-232X. doi: 10.1016/j.coldregions.2019.05.001.

[119] J. Schwarz. New developments in modeling ice problems. *Proc. of 4th POAC*, 1: 45–61, 1977.

[120] Rüdiger U. Franz von Bock und Polach. Numerical analysis of the bending strength of model-scale ice. *Cold Regions Science and Technology*, 118:91–104, October 2015. ISSN 0165-232X. doi: 10.1016/j.coldregions.2015.06.003.

[121] G.W. Timco and W.F. Weeks. A review of the engineering properties of sea ice. *Cold Regions Science and Technology*, 60(2):107–129, February 2010. ISSN 0165-232X. doi: 10.1016/j.coldregions.2009.10.003.

[122] G. J. Komen, L. Cavaleri, M. Donelan, K. Hasselmann, S. Hasselmann, and P. A. E. M. Janssen. *Dynamics and Modelling of Ocean Waves*. Cambridge University Press, September 1994. ISBN 9780511628955. doi: 10.1017/cbo9780511628955.

[123] Leo H. Holthuijsen. *Waves in Oceanic and Coastal Waters*. Cambridge University Press, January 2007. ISBN 9780521129954. doi: 10.1017/cbo9780511618536.

[124] M. Onorato, L. Cavaleri, S. Fouques, O. Gramstad, P. A. E. M. Janssen, J. Monbaliu, A. R. Osborne, C. Pakozdi, M. Serio, C.T. Stansberg, A. Toffoli, and K. Trulsen. Statistical properties of mechanically generated surface gravity waves: a laboratory experiment in a three-dimensional wave basin. *Journal of Fluid Mechanics*, 627:235–257, May 2009. ISSN 1469-7645. doi: 10.1017/s002211200900603x.

[125] A. Toffoli, A. Babanin, M. Onorato, and T. Waseda. Maximum steepness of oceanic waves: Field and laboratory experiments. *Geophysical Research Letters*, 37(5), March 2010. ISSN 1944-8007. doi: 10.1029/2009gl041771.

[126] A. Toffoli, T. Waseda, H. Houtani, L. Cavaleri, D. Greaves, and M. Onorato. Rogue waves in opposing currents: an experimental study on deterministic and stochastic wave trains. *Journal of Fluid Mechanics*, 769:277–297, March 2015. ISSN 1469-7645. doi: 10.1017/jfm.2015.132.

[127] E.P.D. Mansard and E.R. Funke. The measurement of incident and reflected spectra using a least squares method. In *Coastal Engineering 1980*. American Society of Civil Engineers, March 1980. doi: 10.1061/9780872622647.008.

[128] R. Jain, R. Kasturi, and B. G. Schunck. *Machine vision*. McGraw-Hill series in computer science. McGraw-Hill, 1995. ISBN 0070320187.

[129] Kieran F. Mulchrone and Kingshuk Roy Choudhury. Fitting an ellipse to an arbitrary shape: implications for strain analysis. *Journal of Structural Geology*, 26 (1):143–153, January 2004. ISSN 0191-8141. doi: 10.1016/s0191-8141(03)00093-2.

[130] I. de Souza Cabral. *Climate change in the Arctic Ocean: Long-term variability of metocean conditions*. PhD thesis, The University of Melbourne, 2020.

[131] Filippo Nelli, Luke G. Bennetts, David M. Skene, and Alessandro Toffoli. Water wave transmission and energy dissipation by a floating plate in the presence of overwash. *Journal of Fluid Mechanics*, 889, February 2020. ISSN 1469-7645. doi: 10.1017/jfm.2020.75.

[132] P. Joseph and J. Hennessey. A comparison of the weibull and rayleigh distributions for estimating wind power potential. *Wind Engineering*, pages 156–164, 1978.

[133] Michel K. Ochi. *Ocean Waves: The Stochastic Approach*. Cambridge University Press, March 1998. ISBN 9780511529559. doi: 10.1017/cbo9780511529559.

[134] D. Reeve, A. Chadwick, and C. Fleming. *Coastal engineering: processes, theory and design practice*. CRC Press, 3rd edition edition, 2018. ISBN 9781351165525.

[135] David M. Skene and Luke G. Bennetts. A transition-loss theory for waves reflected and transmitted by an overwashed body. *SIAM Journal on Applied Mathematics*, 81(3):834–852, January 2021. ISSN 1095-712X. doi: 10.1137/20m1386979.

[136] C. Fox and V. A. Squire. On the oblique reflexion and transmission of ocean waves at shore fast sea ice. *Philosophical Transactions: Physical Sciences and Engineering*, 347(1682):185–218, April 1994. ISSN 2054-0299. doi: 10.1098/rsta.1994.0044.

[137] M. H. Meylan, L. G. Bennetts, J. E. M. Mosig, W. E. Rogers, M. J. Doble, and M. A. Peter. Dispersion relations, power laws, and energy loss for waves in the marginal ice zone. *Journal of Geophysical Research: Oceans*, 123(5):3322–3335, May 2018. ISSN 2169-9291. doi: 10.1002/2018jc013776.

[138] Luke G. Bennetts and Vernon A. Squire. On the calculation of an attenuation coefficient for transects of ice-covered ocean. *Proceedings of the Royal Society A: Mathematical, Physical and Engineering Sciences*, 468(2137):136–162, August 2011. ISSN 1471-2946. doi: 10.1098/rspa.2011.0155.

[139] Franz von Bock und Polach, Marco Klein, and Moritz Hartmann. A new model ice for wave-ice interaction. *Water*, 13(23):3397, December 2021. ISSN 2073-4441. doi: 10.3390/w13233397.

[140] Thomas Ryan-Keogh and Marcello Vichi. Scale-win19 & scale-spr19 cruise report, 2022.

[141] P.F. Sturm and S.J. Maybank. On plane-based camera calibration: A general algorithm, singularities, applications. In *Proceedings. 1999 IEEE Computer Society Conference on Computer Vision and Pattern Recognition (Cat. No PR00149)*, CVPR-99. IEEE Comput. Soc, 1999. doi: 10.1109/cvpr.1999.786974.

[142] Jean-Yves Bouguet. Camera calibration toolbox for matlab. *http://www. vision. caltech. edu/bouguetj/calib_doc/*, 2004.

[143] Richard Hartley and Andrew Zisserman. *Multiple View Geometry in Computer Vision.* Cambridge University Press, March 2004. ISBN 9780511811685. doi: 10.1017/cbo9780511811685.

[144] Richard C. Gerum, Sebastian Richter, Alexander Winterl, Christoph Mark, Ben Fabry, Céline Le Bohec, and Daniel P. Zitterbart. Cameratransform: A python package for perspective corrections and image mapping. *SoftwareX*, 10:100333, July 2019. ISSN 2352-7110. doi: 10.1016/j.softx.2019.100333.

[145] C. Tomasi and R. Manduchi. Bilateral filtering for gray and color images. In *Sixth International Conference on Computer Vision (IEEE Cat. No.98CH36271)*, ICCV-98. Narosa Publishing House, 1998. doi: 10.1109/iccv.1998.710815.

[146] P. Perona and J. Malik. Scale-space and edge detection using anisotropic diffusion. *IEEE Transactions on Pattern Analysis and Machine Intelligence*, 12(7):629–639, July 1990. ISSN 0162-8828. doi: 10.1109/34.56205.

[147] Karel Zuiderveld. *Contrast Limited Adaptive Histogram Equalization*, pages 474–485. Elsevier, 1994. doi: 10.1016/b978-0-12-336156-1.50061-6.

[148] Kaiming He, Jian Sun, and Xiaoou Tang. Single image haze removal using dark channel prior. *IEEE Transactions on Pattern Analysis and Machine Intelligence*, 33(12):2341–2353, December 2011. ISSN 2160-9292. doi: 10.1109/tpami.2010.168.

[149] Nobuyuki Otsu. A threshold selection method from gray-level histograms. *IEEE Transactions on Systems, Man, and Cybernetics*, 9(1):62–66, January 1979. ISSN 2168-2909. doi: 10.1109/tsmc.1979.4310076.

[150] David W Paglieroni. Distance transforms: Properties and machine vision applications. *CVGIP: Graphical Models and Image Processing*, 54(1):56–74, January 1992. ISSN 1049-9652. doi: 10.1016/1049-9652(92)90034-u.

[151] C.R. Maurer, Rensheng Qi, and V. Raghavan. A linear time algorithm for computing exact euclidean distance transforms of binary images in arbitrary dimensions. *IEEE Transactions on Pattern Analysis and Machine Intelligence*, 25(2):265–270, February 2003. ISSN 0162-8828. doi: 10.1109/tpami.2003.1177156.

[152] Chenyang Xu and J.L. Prince. Snakes, shapes, and gradient vector flow. *IEEE Transactions on Image Processing*, 7(3):359–369, March 1998. ISSN 1057-7149. doi: 10.1109/83.661186.

[153] Michael Kass, Andrew Witkin, and Demetri Terzopoulos. Snakes: Active contour models. *International Journal of Computer Vision*, 1(4):321–331, January 1988. ISSN 1573-1405. doi: 10.1007/bf00133570.

[154] R. Adams. Radial decomposition of disks and spheres. *CVGIP: Graphical Models and Image Processing*, 55(5):325–332, September 1993. ISSN 1049-9652. doi: 10.1006/cgip.1993.1024.

[155] Ayoub B. Ayoub. The eccentricity of a conic section. *The College Mathematics Journal*, 34(2):116–121, March 2003. ISSN 1931-1346. doi: 10.1080/07468342.2003.11921994.

[156] M.J. Bottema. Circularity of objects in images. In *2000 IEEE International Conference on Acoustics, Speech, and Signal Processing. Proceedings (Cat. No.00CH37100)*, ICASSP-00. IEEE, 2000. doi: 10.1109/icassp.2000.859286.

[157] Soumen Biswas and Ranjay Hazra. Robust edge detection based on modified moore-neighbor. *Optik*, 168:931–943, September 2018. ISSN 0030-4026. doi: 10.1016/j.ijleo.2018.05.011.

[158] Alexey Dosovitskiy, Lucas Beyer, Alexander Kolesnikov, Dirk Weissenborn, Xiaohua Zhai, Thomas Unterthiner, Mostafa Dehghani, Matthias Minderer, Georg

Heigold, Sylvain Gelly, Jakob Uszkoreit, and Neil Houlsby. An image is worth 16x16 words: Transformers for image recognition at scale, 2020.

[159] Maithra Raghu, Thomas Unterthiner, Simon Kornblith, Chiyuan Zhang, and Alexey Dosovitskiy. Do vision transformers see like convolutional neural networks?, 2021.

[160] Chaoning Zhang, Fachrina Dewi Puspitasari, Sheng Zheng, Chenghao Li, Yu Qiao, Taegoo Kang, Xinru Shan, Chenshuang Zhang, Caiyan Qin, Francois Rameau, Lik-Hang Lee, Sung-Ho Bae, and Choong Seon Hong. A survey on segment anything model (sam): Vision foundation model meets prompt engineering, 2023.

[161] Jun Ma and Bo Wang. Towards foundation models of biological image segmentation. *Nature Methods*, 20(7):953–955, July 2023. ISSN 1548-7105. doi: 10.1038/s41592-023-01885-0.

[162] Nikhil Ketkar and Jojo Moolayil. *Introduction to PyTorch*, pages 27–91. Apress, 2021. ISBN 9781484253649. doi: 10.1007/978-1-4842-5364-9_2.

[163] J. Sklansky. Recognition of convex blobs. *Pattern Recognition*, 2(1):3–10, January 1970. ISSN 0031-3203. doi: 10.1016/0031-3203(70)90037-3.

[164] A. Wang, B. Wei, J. Sui, J. Wang, N. Xu, and G. Hao. Integrating a data-driven classifier and shape-modulated segmentation for sea-ice floe extraction. *International Journal of Applied Earth Observation and Geoinformation*, 128:103726, April 2024. ISSN 1569-8432. doi: 10.1016/j.jag.2024.103726.

[165] T. Hoang Ngan Le, Khoa Luu, Chi Nhan Duong, Kha Gia Quach, Thanh Dat Truong, Kyle Sadler, and Marios Savvides. *Active Contour Model in Deep Learning Era: A Revise and Review*, pages 231–260. Springer International Publishing, 2020. ISBN 9783030409777. doi: 10.1007/978-3-030-40977-7_11.

[166] Xu Chen, Bryan M. Williams, Srinivasa R. Vallabhaneni, Gabriela Czanner, Rachel Williams, and Yalin Zheng. Learning active contour models for medical image segmentation. In *2019 IEEE/CVF Conference on Computer Vision and Pattern Recognition (CVPR)*. IEEE, June 2019. doi: 10.1109/cvpr.2019.01190.

[167] A. Toffoli, A. Alberello, H. Clarke, F. Nelli, A. Benetazzo, F. Bergamasco, B. Ntamba Ntamba, M. Vichi, and M. Onorato. Observations of rogue seas in the southern ocean. *Physical Review Letters*, 132(15):154101, April 2024. ISSN 1079-7114. doi: 10.1103/physrevlett.132.154101.

[168] G. Spreen, L. Kaleschke, and G. Heygster. Sea ice remote sensing using amsr-e 89-ghz channels. *Journal of Geophysical Research: Oceans*, 113(C2), January 2008. ISSN 0148-0227. doi: 10.1029/2005jc003384.